



Jimmy Mangalam

Lead halide perovskite solar cells: Fabrication challenges  
and interface modification using phosphonic acid self  
assembled monolayers

Doctoral Thesis

To achieve the University degree of  
Doktor der technischen Wissenschaften

Submitted to

Graz University of Technology

Supervisor

Assoc. Prof. Dipl.-Ing. Dr. Techn. Gregor Trimmel  
Institute for Chemistry and Technology of Materials

Graz, May 2019

---

## AFFIDAVIT

---

I declare that I have authored this thesis independently, that I have not used other than the declared sources/resources, and that I have explicitly indicated all material which has been quoted either literally or by content from the sources used. The text document uploaded to TUGRAZonline is identical to the present doctoral thesis.

---

Date

---

Signature

*To my family and the sunshine that awaits...*

---

## ACKNOWLEDGEMENT

---

*Knowledge is in the end based on acknowledgement...*

- *Ludwig Wittgenstein*

I would humbly express my gratitude towards Assoc. Prof. Dipl.-Ing. Dr. Techn. Gregor Trimmel for his supervision and guidance. I am indebted to him for providing the opportunity and mentoring me towards the completion of this journey. His guidance facilitated my understanding of the problems and consequent solution findings. In this endeavour I received many helping hands and ears. I would like to credit Dipl.-Ing. Dr. Techn. Thomas Rath. He walked with me throughout this journey listening to the ideas and issues. We had intense discussions and closely formulated the steps towards understanding and problem solving. I am grateful for his help and friendship.

I thank my co-authors Dr. Theodoros Dimopoulos, Birgit Kunert, and Dipl.-Ing. Alexander Fian for their help in characterizing the materials using scanning electron microscopy, X-ray diffraction, and X-ray photon spectroscopy. These results played an important role in my understanding and the completion of this work.

This work was carried out within the project “flex!PV\_2.0” (FFG No. 853603) funded by the Austrian Climate and Energy Fund within the program Energy Emission Austria.

The Trimmel AG is an excellent place to work as a group, share ideas and discuss problems. Everyone here has been indispensable towards my sanity as I lost and found my ways. To have friends in the form of office mates like Manuel, Franz, and Efthymia was a blessing. Working closely with Stefan on the project was full of meaningful discussions and exchange of anime knowledge. It was pleasing to share break times with Sebastian, Bianca, Reinhold, Corinna, Birgit and Rene. Sharing of meals, coffee and cake was decompressing. I am delighted to affirm the importance of their friendship and support during this process and in my personal and professional growth. These people are wonderful human beings.

Furthermore, I would like to mention Karin and Egbert for providing me the means to come to Graz, Austria and Shashank for informing me about the amazing opportunity to work

closely with them prior to joining Gregor. Their generous thoughtfulness led to my joining in the Trimmel AG.

During my stay in Graz, Austria, I made friends who turned into family. Special thanks to Jörg, Florian (L), Patrick, and Mathias for all the video game lessons, hiking through the nature, cooking together, and specially enduring my irrationalities and teaching me important life lessons. They accepted me as one of theirs. I would also like to mention Georgii, Florian (D), and Pritam for being a part of this journey through evenings of sharing life lessons, intriguing discussions, watching movies, and eating food all the same. They are my international Austrian family. This journey without them would not be worthy.

I would like to mention and acknowledge all my mentors and teachers since the onset of my learning.

I am grateful to my family in India and Neha. I admire them for their patience and perpetual support and understanding.



---

## ABSTRACT

---

Lead halide perovskite solar cells have reached power conversion efficiencies (PCEs) greater than 23%. These materials have shown potential to reach higher efficiencies due to their favourable photovoltaic properties. However, the fabrication of highly efficient lead perovskite solar cells is a challenging task. This thesis explores the influence of different layers involved in the fabrication of conventional (n-type electron transport layer / perovskite absorber layer / p-type hole transport layer) and inverted architectures (p-type hole transport layer / perovskite absorber layer / n-type electron transport layer) for lead perovskite solar cells.

Firstly, in the case of a conventional architecture comparison of different transparent conducting oxides (TCOs) and different hole transport layers (HTLs) have been presented. Indium doped tin oxide (ITO) and fluorine doped tin oxide (FTO) were the choice of TCOs and 2,2',7,7'-tetrakis[*N*, *N*-di(4-methoxyphenyl)amino]-9,9'-spirobifluorene (spiro-OMeTAD) and poly[bis(4-phenyl)(2,4,6-trimethylphenyl)amine] (PTAA) were the choice of HTLs. A cesium, formamidinium, methylammonium, lead, iodide, and bromide based  $\text{Cs}_x(\text{FA}_{0.83}\text{MA}_{0.17})_{1-x}\text{Pb}(\text{I}_{0.83}\text{Br}_{0.17})_3$  perovskite absorber layer was chosen for these solar cells. The PCEs obtained were in the range up to 13% across the variations. The multitude of critical parameters influencing the fabrication process requires meticulous attention. However, not all parameters could be controlled in these experiments.

In addition, for inverted solar cell architecture nickel oxide ( $\text{NiO}_x$ ) based HTL was chosen alongside  $\text{Cs}_x(\text{FA}_{0.83}\text{MA}_{0.17})_{1-x}\text{Pb}(\text{I}_{0.83}\text{Br}_{0.17})_3$  perovskite absorber layer. The interface of the HTL and the perovskite absorber layer was modified using differently functionalized benzylphosphonic acid molecules. These molecules form self-assembled monolayers (SAMs). The modifications were done using benzylphosphonic acid (BPA), 4-bromobenzyl phosphonic acid (Br-BPA), 4-fluorobenzyl phosphonic acid (F-BPA), 4-aminobenzyl phosphonic acid ( $\text{NH}_2$ -BPA), 4-nitrobenzyl phosphonic acid ( $\text{NO}_2$ -BPA), and 4-methoxy benzylphosphonic acid molecules ( $\text{OCH}_3$ -BPA). The successful deposition was carried out using various deposition methods and conditions. The modifications were confirmed through contact angle measurements and X-ray photoelectron spectroscopy. The influences of these molecules on the perovskite were studied using absorption spectroscopy, X-ray diffraction, and scanning electron microscopy. The solar cell devices were characterized using current density – voltage measurements, maximum

power point tracking, and external quantum efficiency. The Br-BPA molecules based solar cells showed an improvement in the open circuit voltage ( $V_{oc}$ ) compared to the non-modified samples in dip coated (from 0.978 V to 1.099 V) and spin coated (from 0.977 V to 1.057 V) samples alike leading stable PCEs of above 12%.



---

## ZUSAMMENFASSUNG

---

In den letzten Jahren haben Bleiperowskitsolarzellen einen stetig steigenden Aufwärtstrend gezeigt, welche mittlerweile die 23% Marke überschritten haben und damit großes Potential im Bereich der Photovoltaik darstellen. Nichtsdestotrotz ist die Herstellung solch effizienter Energieträger eine große Herausforderung. Diese Arbeit beschäftigt sich mit dem Einfluss unterschiedlicher Transportschichten in der konventionellen (*n-i-p*) sowie der inversen (*p-i-n*) Aufbaustruktur in Bleiperowskitsolarzellen.

Zunächst wurde der Einfluss von transparent leitfähigen Schichten (*TCO*) und der Lochleiterschicht im *n-i-p* Aufbau dargestellt. Dabei wurden die zwei transparenten Schichten Indium dotiertes Zinnoxid (*ITO*) und Fluor dotiertes Zinnoxid (*FTO*) sowie die Lochleiter *spiro-OMeTAD* und *PTAA* untereinander verglichen. Der dazugehörige Bleiperowskitabsorber besteht aus einer Kombination aus Cäsium, Formamidinium, Methylammonium, Blei, Iodid und Bromid mit der Zusammensetzung  $\text{Cs}_x(\text{FA}_{0.83}\text{MA}_{0.17})_{1-x}\text{Pb}(\text{I}_{0.83}\text{Br}_{0.17})_3$ . Die damit untersuchten Solarzellen zeigten Effizienzen um die 13%. Jedoch muss man bei der Herstellung effizienter Solarzellen eine Vielzahl von kritischen Prozessierungsparametern berücksichtigen um reproduzierbare Ergebnisse zu erhalten. Die Kontrolle all dieser Parameter konnte aber nicht bewerkstelligt werden.

In weiterer Folge wird der Einfluss von  $\text{NiO}_x$  als Lochleiter im inversen Aufbau mit demselben Bleiperowskitabsorber  $\text{Cs}_x(\text{FA}_{0.83}\text{MA}_{0.17})_{1-x}\text{Pb}(\text{I}_{0.83}\text{Br}_{0.17})_3$  dargelegt. Eine Modifizierung der  $\text{NiO}_x$ /Perowskit Zwischenschicht durch selbst assemblierende Monolagen (*SAMs*) konnte durch funktionalisierte Benzylphosphonsäure-Moleküle bewerkstelligt werden. Dabei wurden die SAM Moleküle Benzylphosphonsäure (*BPA*), 4-Brombenzylphosphonsäure (*Br-BPA*), 4-Fluorbenzylphosphonsäure (*F-BPA*), 4-Aminbenzylphosphonsäure (*NH<sub>2</sub>-BPA*), 4-Nitrobenzylphosphonsäure (*NO<sub>2</sub>-BPA*) und 4-Methoxybenzylphosphonsäure (*OCH<sub>3</sub>-BPA*) untersucht. Die Monoschicht konnte über verschiedene Beschichtungsmethoden aufgebracht werden und wurde durch Kontaktwinkelmessungen und Röntgenphotoelektronenspektroskopie nachgewiesen. In weiterer Folge wurde der Einfluss dieser Schicht auf die Perowskit Schicht durch Absorptionsspektroskopie, Röntgendiffraktometrie und Rasterelektronenmikroskopie untersucht. Fertiggestellte Solarzellen wurden mittels Strom-Spannung Messungen, *maximum power point tracking* und Externer Quanteneffizienz Messungen charakterisiert. Bleiperowskit Solarzellen mit *Br-BPA* zeigen eine Verbesserung der Leerlaufspannung im Vergleich zu nicht-modifizierten Solarzellen. Dabei ist die Erhöhung der Leerlaufspannung unabhängig von der

Beschichtungsmethode - Tauchmethode (von 0.978 V zu 1.099 V) sowie Rotationsbeschichtung (von 0.977 V zu 1.057 V) – und man erhält konstante Effizienzen um 12%.

---

## Table of Contents

---

|   |            |
|---|------------|
| <b>AFFIDAVIT</b> .....  | <b>ii</b>  |
| <b>ACKNOWLEDGEMENT</b> .....  | <b>iv</b>  |
| <b>ABSTRACT</b> .....   | <b>vii</b> |
| <b>ZUSAMMENFASSUNG</b> .....  | <b>ix</b>  |
| <b>Author’s contribution</b> .....  | <b>16</b>  |
| <b>Chapter 1: An Introduction to Perovskite materials and basics of Solar cells</b> ..... | <b>18</b>  |
| Perovskites and its introduction to solar cells .....                                     | 19         |
| Perovskite crystal structure.....   | 19         |
| Solar cell architectures and components .....   | 21         |
| State of the art for lead halide perovskite solar cells.....                              | 25         |
| Issues with perovskite solar cells .....  | 28         |
| Hysteresis .....  | 28         |
| Toxicity.....   | 29         |
| Solar cell working principles .....   | 30         |
| Electrical characteristics .....  | 32         |
| Power conversion efficiency, PCE, $\eta$ .....  | 32         |
| Short circuit current density, $J_{SC}$ .....   | 34         |
| Open circuit voltage, $V_{OC}$ .....  | 34         |
| Maximum power point, MPP .....  | 35         |
| Fill Factor, FF .....   | 35         |
| External Quantum Efficiency, EQE .....  | 36         |
| Aim, motivation and objectives.....   | 37         |

|   |           |
|---|-----------|
| Insight to the thesis .....   | 38        |
| References .....  | 40        |
| <b>Chapter 2: Influence of different layers on the performance of solar cells in n-i-p architecture .....</b> | <b>48</b> |
| Introduction .....  | 49        |
| Materials and methods.....  | 50        |
| Sample and solar cell preparation.....  | 50        |
| Front contact.....  | 50        |
| Titanium dioxide .....  | 50        |
| CsFAMA perovskite.....  | 51        |
| Spiro-OMeTAD.....   | 51        |
| PTAA.....   | 51        |
| Gold (Au).....  | 52        |
| Characterization techniques.....  | 52        |
| Results and discussion .....  | 52        |
| Influence of Cs content in CsFAMA perovskite absorber layer .....   | 55        |
| Influence of doping on spiro-OMeTAD HTL .....   | 62        |
| Challenges during fabrication of lead perovskite solar cells.....   | 67        |
| Stock solution method .....   | 68        |
| Conclusion.....   | 70        |
| References .....  | 72        |

|   |           |
|---|-----------|
| <b>Chapter 3: Modification of NiO<sub>x</sub> hole transport layers with 4-bromobenzylphosphonic acid and its influence on the performance of lead halide perovskite solar cells.....</b> | <b>77</b> |
| Abstract.....   | 78        |
| Keywords.....   | 78        |
| Introduction .....  | 78        |
| Experimental.....   | 80        |
| Sample and solar cell preparation.....  | 80        |
| Material synthesis .....  | 80        |
| Solar cell preparation.....   | 80        |
| Characterization techniques.....  | 82        |
| Results and discussion .....  | 83        |
| Conclusion .....  | 92        |
| Acknowledgement .....   | 93        |
| References .....  | 94        |
| <b>Chapter 4: Benzyl phosphonic acid SAMs in p-i-n architecture .....</b>   | <b>99</b> |
| Introduction .....  | 100       |
| Materials and methods.....  | 102       |
| Sample and solar cell preparation.....  | 102       |
| Front contact.....  | 102       |
| NiO <sub>x</sub> nanoparticles.....   | 102       |
| NiO <sub>x</sub> sol-gel .....  | 103       |

|   |            |
|---|------------|
| Deposition of R-BPA SAM.....                    | 103        |
| Dip coating .....                               | 103        |
| Dynamic spin coating .....                      | 103        |
| Preparation of CsFAMA perovskite .....          | 104        |
| Electron transport layer and back contact ..... | 104        |
| Characterization techniques.....                | 104        |
| Results and discussion.....                     | 105        |
| Dip coated R-BPA SAMs.....                      | 105        |
| Spin coated R-BPA SAMs .....                    | 121        |
| Conclusion.....                                 | 128        |
| References .....                                | 130        |
| <b>Chapter 5: Conclusion and Outlook .....</b>  | <b>133</b> |
| Conclusion.....                                 | 134        |
| Outlook: Future and alternatives .....          | 136        |
| References .....                                | 138        |
| <b>APPENDIX .....</b>                           | <b>143</b> |
| <b>LIST OF FIGURES.....</b>                     | <b>150</b> |
| <b>LIST OF TABLES.....</b>                      | <b>155</b> |
| <b>CURRICULUM VITAE .....</b>                   | <b>158</b> |



---

## **Author's contribution**

---

### **Jimmy Mangalam**

Literature survey, planning of experiments, solar cells fabrication, sol-gel NiO<sub>x</sub> synthesis, current density–voltage measurements, maximum power point tracking measurements, samples for material and device characterization, ultraviolet-visible spectroscopy (absorbance and transmittance) measurements, surface profile measurements, manuscript preparation (writing, analysis and discussion), result analysis and thesis compilation

### **Thomas Rath**

External Quantum Efficiency measurements, contact angle measurements, surface profile measurements, manuscript preparation (writing, analysis and discussion) and correspondence to the journal

### **Stefan Weber**

NiO<sub>x</sub> nanoparticle synthesis

### **Birgit Kunert**

X-ray Diffraction

### **Theodoros Dimopoulos**

Scanning Electron Microscopy images

### **Alexander Fian**

X-ray Photoelectron Spectroscopy

### **Gregor Trimmel**

Supervision and guidance





# **Chapter 1: An Introduction to Perovskite materials and basics of Solar cells**

---

*A good introduction stimulates the curious mind...*

- *Yours truly*

## Perovskites and its introduction to solar cells

In 1839, a German mineralogist, G. Rose, unearthed a new mineral, calcium titanate ( $\text{CaTiO}_3$ ), in the Ural Mountains of Russia. This new mineral was later named “Perovskite” after the Russian mineralogist L. Perovski [1]. Perovskite oxides such as  $\text{CaTiO}_3$ , barium titanate ( $\text{BaTiO}_3$ ), magnesium metasilicate ( $\text{MgSiO}_3$ ), and strontium cerate ( $\text{SrCeO}_3$ ) have useful properties such as dielectricity, ferroelectricity, lithium-ion conduction, piezoelectricity and superconductivity [2-5]. Reports have shown that sodium tantalum oxide ( $\text{NaTaO}_3$ ) with nickel(II) oxide ( $\text{NiO}$ ) has been an effective UV-photocatalyst for water splitting [6,7]. Alongside the oxide based composition of perovskites, these materials also have an organic-inorganic metal halide based composition which are suited for photovoltaic applications. In 2009, the photovoltaic family was joined by a highly potent and promising new member in the form of methylammonium lead bromide and methylammonium lead iodide ( $\text{CH}_3\text{NH}_3\text{PbBr}_3$  and  $\text{CH}_3\text{NH}_3\text{PbI}_3$ ) [8]. The properties of these materials make them highly useful for solar cell applications [9-23]. The ability to form compounds with varying organic, inorganic and halide compositions allow control over the optical behaviour of these materials [24]. Perovskites also tend to have low trap density and electron-hole diffusion lengths above  $100\ \mu\text{m}$  [25-27]. These properties help in wide uptake of the solar energy resulting in efficient charge generation and collection. The widely used organic or inorganic cations are formamidinium ( $\text{FA}^+$ ), methylammonium ( $\text{MA}^+$ ), rubidium ( $\text{Rb}^+$ ) and cesium ( $\text{Cs}^+$ ). For metal centres an attempt to replace lead ( $\text{Pb}^{2+}$ ) by tin ( $\text{Sn}^{2+}$ ) has been widely researched. Similarly, different halides such as iodide ( $\text{I}^-$ ), bromide ( $\text{Br}^-$ ), and chloride ( $\text{Cl}^-$ ) have been tried. There have been successful attempts in creating multi-cation systems and or multi-halide systems [10-23]. These attempts have led towards improvement of power conversion efficiency (PCE) from 3.18% to above 20% (example:  $\text{Cs}_{0.1}(\text{FA}_{0.83}\text{MA}_{0.17})_{0.9}\text{Pb}(\text{I}_{0.83}\text{Br}_{0.17})_3$ ) [8,22,23].

### Perovskite crystal structure

To achieve the best possible composition for highly efficient solar cells based on perovskite materials as absorber layers it is necessary to understand the crystal structure. In 1926, a Norwegian mineralogist, V. M. Goldschmidt, published a description about the, now popular, crystal structure of perovskite [28]. Later in 1945, X-ray diffraction (XRD) data on  $\text{BaTiO}_3$  was published by an Irish crystallographer, H. D. Megaw where he described an ideal perovskite structure to be a simple cubic [29]. The perovskite crystal structure is

composed of an  $ABO_3$  composition where “A” and “B” are divalent and trivalent metal cations respectively, and “O” is oxygen [29]. In the case of lead halide perovskite, the “O” is replaced by monovalent halides (X) and the composition and “A” and “B” are monovalent and divalent metal cation respectively and looks like  $ABX_3$ . The ideal perovskite crystal is cubic and has a Goldschmidt tolerance factor,  $t = 1$ . However, relying upon the value of “ $t$ ”, the perovskite can have cubic ( $1.00 \geq t \geq 0.90$ ) or distorted perovskite with orthorhombic crystal structure ( $0.89 \geq t \geq 0.80$ ) [28, 30-36]. The value of “ $t$ ” is dependent upon the ionic radii of “A”, “B”, and “X” which are represented by  $r_A$ ,  $r_B$  and  $r_X$  respectively.

$$t = \frac{(r_A + r_X)}{\sqrt{2}(r_B + r_X)} \quad (1)$$

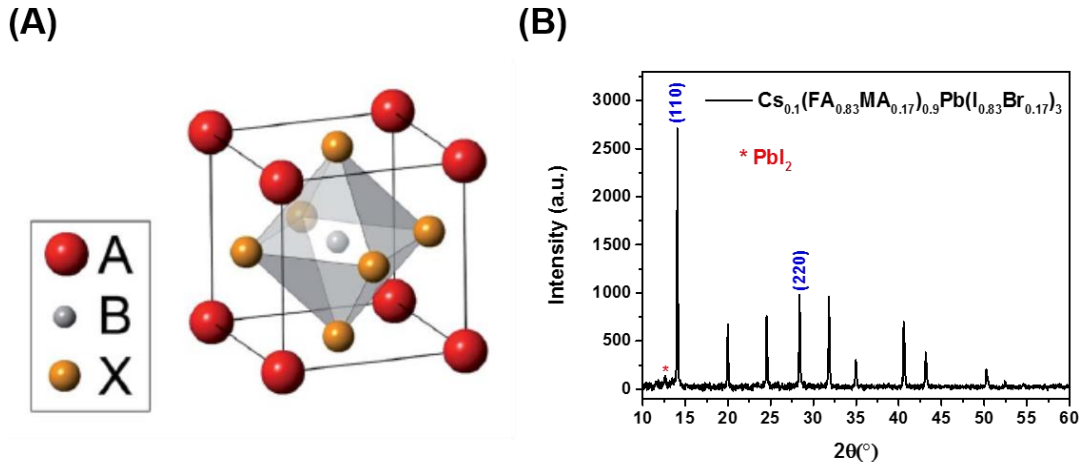


**Figure 1:** (A) The  $ABX_3$  perovskite crystal structure with “A”-site monovalent cation, “B”-site divalent metal cation, and “X”-site monovalent halide anion. Reproduced with permission from Ref. [18]. Copyright © 2014. The Royal Society of Chemistry. (B) XRD reflexes for a triple cation and a double halide perovskite with lead as a metal centre having a  $Cs_{0.1}(FA_{0.83}MA_{0.17})_{0.9}Pb(I_{0.83}Br_{0.17})_3$  composition [22,38].

The crystal structure of a lead perovskite can be further understood using XRD spectroscopy. In **Figure 1B**, for a triple cation lead double halide perovskite, investigated by Saliba et al. in 2016, with composition of  $Cs_{0.1}(FA_{0.83}MA_{0.17})_{0.9}Pb(I_{0.83}Br_{0.17})_3$ , the XRD reflections show prominent perovskite peaks at  $2\theta$  equals  $14.08^\circ$  and  $28.36^\circ$  for the (110) and (220) lattice planes respectively. In addition, other signature peaks at  $2\theta$  equals  $19.96^\circ$ ,  $24.54^\circ$ ,  $31.81^\circ$ ,  $34.98^\circ$ ,  $40.58^\circ$ ,  $43.15^\circ$  and  $50.24^\circ$  were observed [22,37,38]. To attain elevated

photovoltaic performances, lead iodide ( $\text{PbI}_2$ ) is added in slight excess [39]. The corresponding cubic lead iodide peak can be seen at  $2\theta$  equals  $12.6^\circ$  indicated by the \* mark [22,40]. The solvents such as dimethylsulfoxide (DMSO), dimethylformamide (DMF), and  $\gamma$ -butyrolactone (GBL) allow precipitation of perovskite [41,42]. In a study done by Liang et al., effects of additive such as 1, 8-diiodooctane (DIO) on modulating the perovskite thin film formation were investigated. They suggest that DIO chelates with  $\text{Pb}^{2+}$  ions in the solution state which in turn helps to achieve a smoother film [43]. They confirmed the assistance using XRD reflections. Similarly, there are reports which suggest, for  $\text{CH}_3\text{NH}_3\text{PbI}_3$  (MAPI), methylammonium iodide (MAI) –  $\text{PbI}_2$  – DMSO form a complex,  $\text{MA}_2\text{Pb}_3\text{I}_8(\text{DMSO})_2$ , that aid the process of perovskite formation when antisolvent is dripped during the spin coating process [44]. In another report by Guo et al., they report a  $\text{PbI}_2$  – MAI – DMF complex formation. They were able to show it as an intermediate phase forming a monoclinic structure [37]. However, they also argue that the excess  $\text{PbI}_2$  act like a double-edged sword for the perovskite encompassing the favourable crystallization and the inevitable instability.

### **Solar cell architectures and components**

By understanding the crystal structure of perovskites, these materials can be incorporated in the solar cells as an absorber layer. The performance of the solar cells is heavily dependent upon the various components used to design it. The perovskite solar cell can be basically fabricated in two different arrangements, better known as architectures. The arrangements depend upon the placement of the p-type hole transport layer (HTL) and the n-type electron transport layer (ETL) with respect to the contacts namely; transparent conducting oxide (TCO) and the back metal electrode (BE). Conventionally an n-i-p architecture consists of TCO/ETL/Perovskite/HTL/BE setup and an inverted p-i-n architecture consists of TCO/HTL/Perovskite/ETL/BE setup. Other than the primary arrangement difference, in a conventional setup, the TCO acts like a cathode and the BE acts like an anode. The role is reversed for the inverted architecture. The different architectures can be further branched out into two different forms. This depends upon the nature of the layer on which the perovskite is deposited. In case of the conventional n-i-p architecture, the ETL can be either planar or mesoporous (mp) in nature. Similarly, in the inverted p-i-n architecture, the HTL can be either planar or mesoporous in nature. The different architectures along with their variations are depicted in the **Figure 2**. The mesoporous nature of the layers allow infiltration into the perovskite absorber layer and this in turn improves the charge extraction capabilities at the

interface of the concerned charge transport layer (CTL). The infiltration also allows reduced mean free path for the charges and therefore the probability of recombination is reduced [45-48].

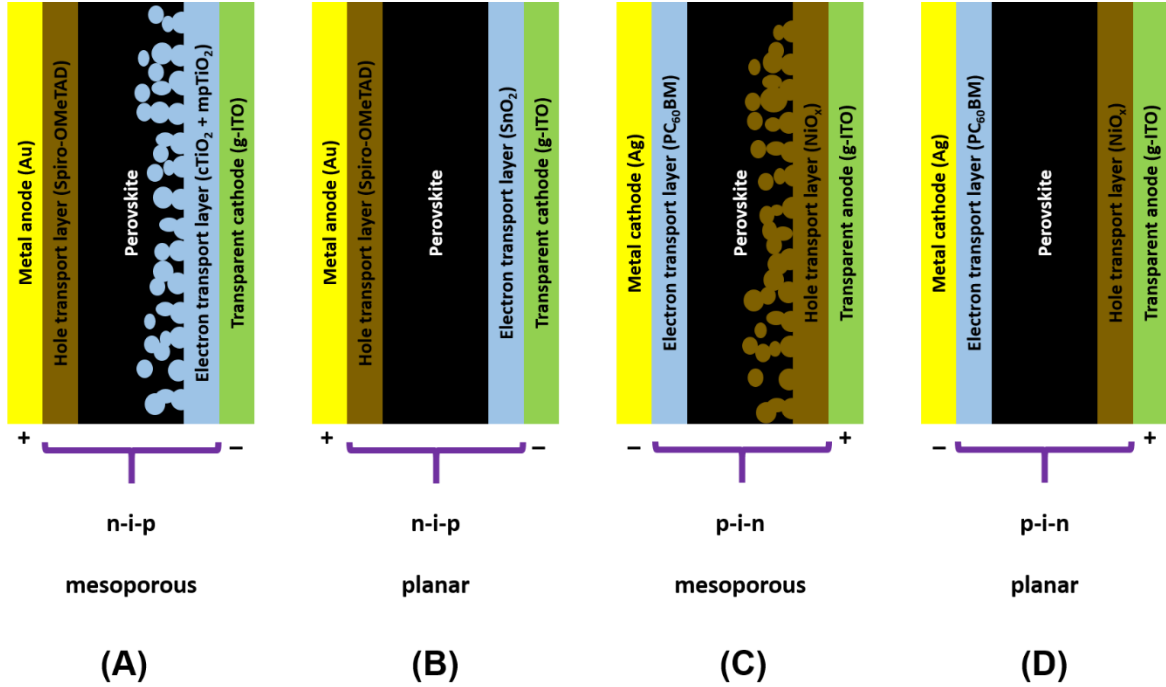


**Figure 2:** (A) mesoporous and (B) planar n-i-p architecture, and (C) mesoporous (mp) and (D) planar p-i-n architecture for perovskite solar cells. The metal (anode / cathode) is used as BE, spiro-OMeTAD or NiO<sub>x</sub> is used as HTL, cTiO<sub>2</sub> and mpTiO<sub>2</sub>, and PCBM are used as ETL, and ITO patterned on glass (g-ITO) is used as TCO (cathode / anode).

To achieve high efficiency in solar cells, it is imperative to choose the optimal combination of CTLs, perovskite composition and contact electrodes (TCO and BE). There are various organic (polymers or small molecules) and inorganic (metal oxide) options available for CTLs. The alignment of the respective highest occupied molecular orbital (HOMO) and lowest unoccupied molecular orbital (LUMO) (for organic), and valence band (VB) and conduction band (CB) (for inorganic) levels with the HOMO and LUMO levels of the perovskite has to be optimized. Some of the commonly used TCOs, ETLs, perovskites, HTLs and BEs arranged according to their energy levels are shown in the **Figure 3**.

In the case of HTLs, 2,2',7,7'-tetrakis[*N*, *N*-di(4-methoxyphenyl)amino]-9,9'-spirobifluorene (spiro-OMeTAD) has been a crucial component alongside poly[bis(4-phenyl)(2,4,6-trimethylphenyl)amine] (PTAA) for the conventional n-i-p architecture [23,49,50]. The single crystal of spiro-OMeTAD has hole mobility in the range of 10<sup>-4</sup>-10<sup>-3</sup>

$\text{cm}^2 \text{V}^{-1} \text{s}^{-1}$  [51]. However, when doped with bis(trifluoromethylsulfonyl)imide lithium (LiTFSI) salt, (tris(2-(1H-pyrazol-1yl)-4-tert-Butylpyridine)cobalt(III) bis(trifluoromethylsulfonyl)imide) (FK209 cobalt salt), and 4-tert-butylpyridine (TBP), the mobility values can increase by one order of magnitude [52]. In comparison, PTAA has a hole mobility in the range of  $10^{-3}$ - $10^{-2} \text{cm}^2 \text{V}^{-1} \text{s}^{-1}$  [53]. The HOMO levels of spiro-OMeTAD and PTAA are -5.2 eV and -5.1 eV respectively [54]. In case of the inverted p-i-n architecture, unlike n-i-p architecture,  $\text{NiO}_x$  is used as a HTL alongside poly(3,4-ethylenedioxythiophene) polystyrene sulfonate (PEDOT:PSS). The hole mobility for  $\text{NiO}_x$ , PEDOT:PSS and poly (3-hexylthiophen-2,5-diyl) (P3HT) have been reported to be in the range of  $10^{-3}$ - $10^{-2} \text{cm}^2 \text{V}^{-1} \text{s}^{-1}$ ,  $10^{-2}$ - $10^{-1} \text{cm}^2 \text{V}^{-1} \text{s}^{-1}$  and  $10^{-5}$ - $10^{-4} \text{cm}^2 \text{V}^{-1} \text{s}^{-1}$  respectively [55-57]. The HOMO levels of PEDOT:PSS and P3HT are at -5.1 eV and -5.0 eV respectively and the valence band (VB) of  $\text{NiO}_x$  is at -5.49 eV [54,58,59]. It is important to note that  $\text{NiO}_x$  and P3HT have also been used in n-i-p architectures and similarly, PTAA has been used in p-i-n architectures [60-62].

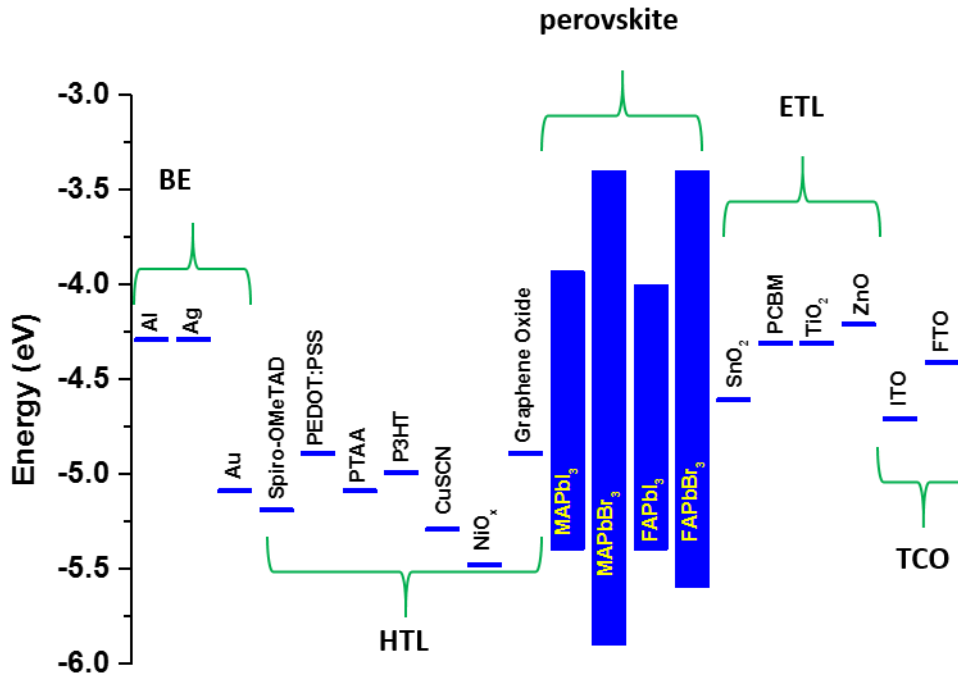


**Figure 3:** The HOMO and LUMO level alignments for different CTLs (HTLs and ETLs), perovskites, TCOs, and BEs [63-70].

In case of ETLs for perovskite solar cells, the partnership of mesoporous and compact titanium dioxide (cTiO<sub>2</sub> and mpTiO<sub>2</sub>) have been vital to achieving higher power conversion efficiencies. The electron mobility for TiO<sub>2</sub> has been reported in the range of 10<sup>-1</sup>-10<sup>2</sup> cm<sup>2</sup> V<sup>-1</sup> s<sup>-1</sup> depending upon the temperature where the value rises for low temperatures [71,72]. Similar to spiro-OMeTAD, the electrical performance of cTiO<sub>2</sub> and mpTiO<sub>2</sub> improves by doping it with LiTFSI salt [46]. Alongside, TiO<sub>2</sub>, tin oxide (SnO<sub>2</sub>) has also performed well as an ETL [73]. This is primarily because the electron mobility values for SnO<sub>2</sub> is as high as ~10<sup>2</sup> cm<sup>2</sup> V<sup>-1</sup> s<sup>-1</sup> at room temperature [74]. SnO<sub>2</sub> has a CB of -4.5 eV compared to TiO<sub>2</sub> with -4.3 eV [75]. Similar to PTAA as HTL, TiO<sub>2</sub> can be used as ETL in both conventional n-i-p and inverted p-i-n architecture [76].

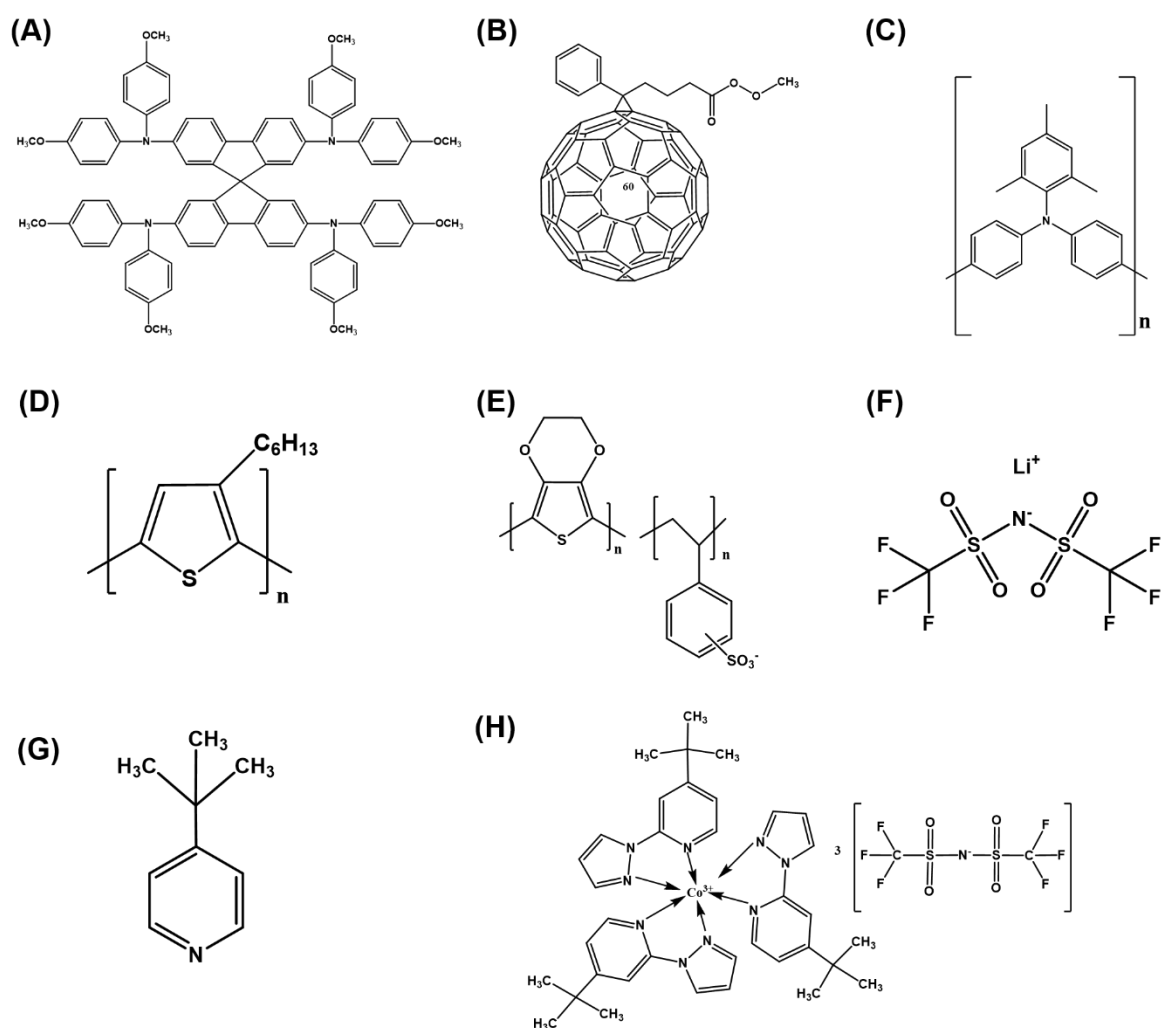


**Figure 4:** Chemical structures of (A) spiro-OMeTAD, (B) PC<sub>60</sub>BM, (C) PTAA, (D) P3HT (E) PEDOT:PSS, (F) LiTFSI, (G) TBP, and (H) FK209.



## State of the art for lead halide perovskite solar cells

In the past decade, the hybrid inorganic – organic perovskite materials have been comprehensively researched due to their promising photovoltaic properties. The flexibility to vary the A-site cations and X-site halides have allowed the lead based perovskites to reach above 20% power conversion efficiencies [21-23, 77-80]. According the 53<sup>rd</sup> version of the solar cell efficiency tables, a 23.7% efficient cell has been certified by Newport (9/18) for Institute for Semiconductors of Chinese Academy of Science (ISCAS) Beijing [81]. In 2018, Jeon et al. published an article where they presented a solar cell with 22.5% and 23.2% power conversion efficiencies (PCEs) in forward and reverse sweeps (FS and RS) with a 22.85% steady state efficiency for 0.0939 cm<sup>2</sup> cells [82].

They used (FAPbI<sub>3</sub>)<sub>0.95</sub>(MAPbBr<sub>3</sub>)<sub>0.05</sub> as the perovskite absorber layer and introduced a fluorine-terminated HTL in comparison to spiro-OMeTAD. They synthesized the new material for HTL namely, (N<sup>2</sup>,N<sup>2'</sup>,N<sup>7</sup>,N<sup>7'</sup>- tetrakis(9,9-dimethyl-9H-fluoren-2-yl)-N<sup>2</sup>,N<sup>2'</sup>,N<sup>7</sup>,N<sup>7'</sup>-tetrakis(4-methoxyphenyl)-9,9'-spirobi[fluorine]-2,2',7,7'-tetraamine) (DM). They fabricated an n-i-p architecture based solar cell, commonly known as the conventional solar cell architecture. To reach highly efficient solar cells with PCEs > 20%, Saliba et al. incorporated rubidium into perovskite solar cells and formed an RbCsMAFA based quadruple cation perovskite. They realized a solar cell with 21.3% and 21.8% PCEs in FS and RS directions respectively by achieving fill factors (FFs) of 0.8 and 0.81. They also observed an open circuit voltage (V<sub>OC</sub>) of 1.180 V for the RS for their champion cell. However, their champion V<sub>OC</sub> was at 1.24 V against the bandgap of 1.6 eV [23]. Coincidentally, in contrast to Saliba's mesoporous system, Anaraki et al. published a solution processed planar SnO<sub>2</sub> based perovskite solar cells with a V<sub>OC</sub> of 1.214 V [78]. They compared spin coating, chemical bath deposition, and atomic layer deposition techniques for SnO<sub>2</sub> deposition on the substrates. They reported PCEs greater than 19%. However, it has to be noted that the achieved V<sub>OC</sub> was for an unmasked device. Similarly, Tavakoli et al. published 21.65% efficient cell with a V<sub>OC</sub> of 1.193 V for a (FAPbI<sub>3</sub>)<sub>0.87</sub>(MAPbBr<sub>3</sub>)<sub>0.13</sub> perovskite absorber layer with a solar cell area of 0.16 cm<sup>2</sup> [83]. They increased the grain size of the perovskites by adding methylammonium chloride (MAcI) to their precursor solution. This facilitated decreased carrier recombination and increased diffusion length. According to Tress et al., a V<sub>OC</sub> of 1.33±0.02 V would be predicted by Shockley Queisser limit for band edge absorber with band gap of 1.59 to 1.63 eV [84]. They studied the role of radiative and non-radiative recombinations for MAPI perovskite solar cells. In a two-step

spin-coating method for depositing  $(\text{FAPbI}_3)_{1-x}(\text{MAPbBr}_3)_x$  on planar  $\text{SnO}_2$ , Jiang et al. communicated a 21.6% efficient solar cell for an area of  $0.0737 \text{ cm}^2$  [85]. They studied the importance of excess  $\text{PbI}_2$  on the quality and performance of the perovskite solar cell. They concluded that too much residual  $\text{PbI}_2$  could contribute to hysteresis and poor stability.

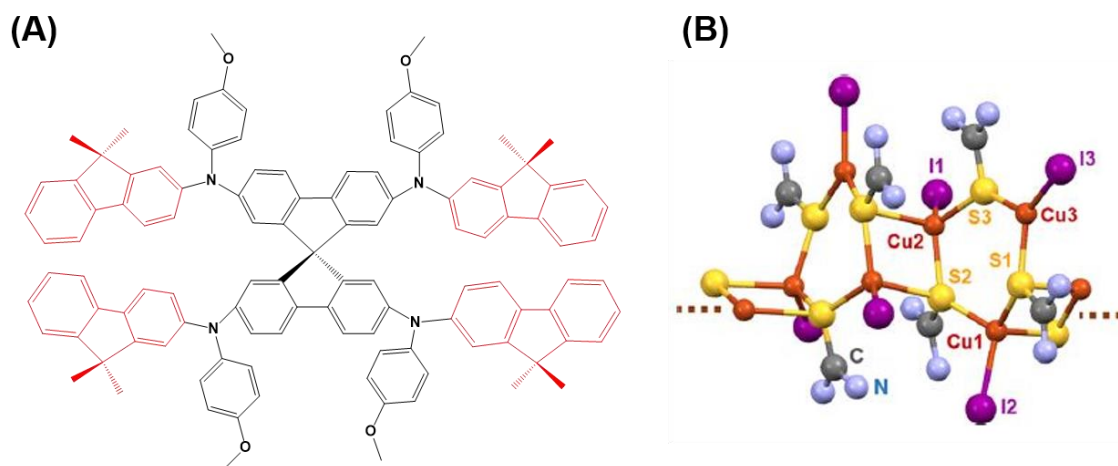


**Figure 5:** (A) Chemical structure of the new HTM, DM, used by Jeon et al. to achieve 23.2% efficient cells in a conventional architecture based solar cell [82]. (B) Crystal structure of  $\text{Cu}(\text{thiourea})\text{I}$  used by Ye et al. to achieve 19.9% efficient cells in an inverted architecture based perovskite solar cell. The crystal structure of  $\text{Cu}(\text{thiourea})\text{I}$  was Reprinted with permission from reference 87. Copyright © 2017. American Chemical Society.

However, when used moderately, stable performances could be achieved. They reported integrated  $J_{\text{SC}} > 23.0 \text{ mAcm}^{-2}$  for all of their combinations of cells in matching with the corresponding EQEs. They also reported PCEs of 20.11% and 20.12% for a device with an area of  $1 \text{ cm}^2$ . In another attempt, Tan et al. showed chlorine capped  $\text{TiO}_2$  ( $\text{TiO}_2\text{-Cl}$ ) nanocrystals, as electron selective layer, could be valuable to reduce hysteresis in perovskite solar cells and achieve average of 19.6% efficient cells for more than 200 devices. They showed hysteresis free solar cells, with an area of  $0.049 \text{ cm}^2$ , with an efficiency of 21.4% for  $\text{Cs}_{0.05}\text{FA}_{0.81}\text{MA}_{0.14}\text{PbI}_{2.55}\text{Br}_{0.45}$  perovskite absorber layer. However, solar cells with an area of  $1.1 \text{ cm}^2$  showed slight hysteresis with 20.1% and 20.3% PCEs. In the end they concluded that  $\text{TiO}_2\text{-Cl}$  have a stronger binding to the perovskite interface and therefore suppress the interfacial recombination and improve stability. Similarly, Wu et al. communicated a PCE of 19.19% for solar cells with an area of  $1.025 \text{ cm}^2$ . The best performing cell had PCEs of 19.46% and 19.58% in FS and BS directions [86]. The focus of the study was to use additives like methylammonium acetate and thio-semicarbazide in

MAPI to improve the thermal stability. As the PCEs for n-i-p architecture based perovskite solar cells have crossed 22% mark, p-i-n architecture based perovskite solar cells have also shown promise. Therefore, in contrast to the conventional architecture, for inverted architecture, Ye et al. reported an impressive 19.9% efficient solar cell. They used p-type Cu(thiourea)I as a trap state passivator in perovskites in a ITO/perovskite-Cu(thiourea)I/C<sub>60</sub>/BCP/Ag setup [87]. They showed 19.9% and 20.0% PCEs in FS and BS for a MAPbI<sub>3-x</sub>Cl<sub>x</sub> based perovskite absorber layer having a solar cell area of 0.1 cm<sup>2</sup>. They concluded that the trap state passivators interact with the under-coordinated metal cations and halide anions at the perovskite crystal surface thereby shallowing the traps.

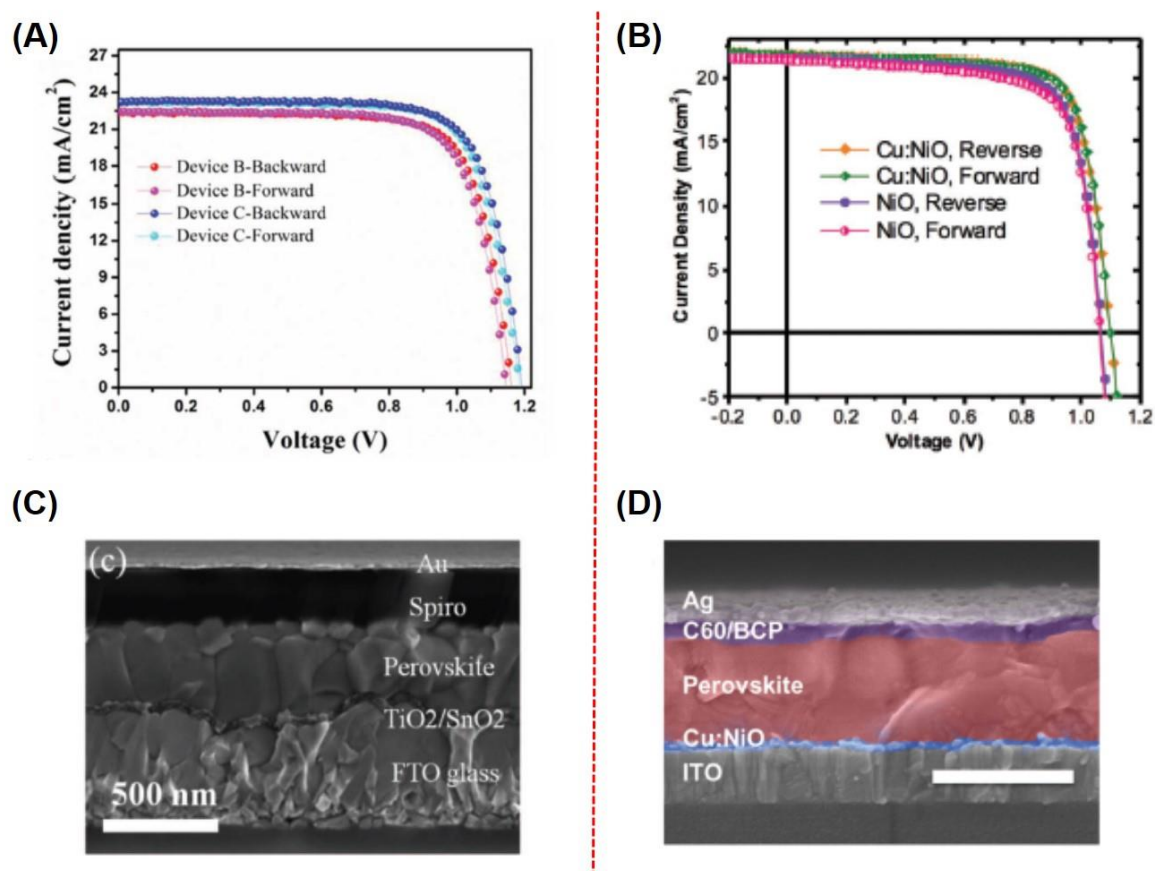


**Figure 6:** (A) JV curves for champion devices and (C) cross sectional SEM image of the device published by Tavakoli et al., and (B) JV curves for large-area NiO<sub>x</sub> and Cu:NiO<sub>x</sub> based inverted devices and (D) cross sectional SEM image of the device published by Chen et al.. Reprinted with permission from reference 83 and 49 respectively. Copyright © 2018 WILEY-VCH Verlag GmbH & Co. KGaA, Weinheim.

Focusing on improving the quality and properties of NiO<sub>x</sub>, Chen et al. doped NiO<sub>x</sub> with copper in a low-temperature solution process. They attained notable PCEs of 20.26% for

Cu:NiO<sub>x</sub> as HTM in comparison to 18.18% PCE for the non doped NiO<sub>x</sub> [49]. They used MAPI as the perovskite absorber layer having a solar cell area of 0.08 cm<sup>2</sup>. In similar attempts, Chen et al. doped NiO<sub>x</sub> with cesium (Cs:NiO<sub>x</sub>) [88]. They reported PCEs of 19.23% and 19.35% in FS and BS directions with FFs reaching 79% for MAPI as the perovskite absorber layer having a solar cell area of 10 mm<sup>2</sup> (0.1 cm<sup>2</sup>). Similarly, Kim et al. achieved a 17.2% efficient cell with Cs:NiO<sub>x</sub> with 78% fill factor for solar cell with an area of 0.16 cm<sup>2</sup> [89]. They used a mixture of FAPbI<sub>3</sub>, MAPbBr<sub>3</sub>, and CsI in a ratio of 5:1:0.3 for their absorber layer. They concluded that the incorporation of Cs had led to an efficient separation of the holes in the perovskites. Therefore, similar to Chen et al. for Cu:NiO<sub>x</sub> and Cs:NiO<sub>x</sub>, Kim et al. advocated the improved hole extraction capabilities of the doped NiO<sub>x</sub>. In an related attempt, Zheng et al. successfully doped NiO<sub>x</sub> with silver (Ag:NiO<sub>x</sub>). They succeeded to build a 17.3% and 17.2% efficient cell in FS and BS directions with Ag:NiO<sub>x</sub> as the HTM for MAPI based perovskite absorber layer having a solar cell area of 0.159 cm<sup>2</sup>. They reported a stable PCE of 17.1% against 15.5% for non-doped NiO<sub>x</sub>.

## **Issues with perovskite solar cells**

### **Hysteresis**

The inconsistency in the photovoltaic performance of the solar cell when measured under FS (short circuit condition to open circuit condition) and BS (open circuit condition to short circuit condition) directions is observed as hysteresis. Among various reasons that may affect this behaviour, ion migration, defect states and traps, scan rate, device architecture, scan direction, and light soaking are some of the major contributors [90-98]. The origins of hysteresis have been comprehensively researched and reported [99-103]. The importance to understand and eliminate the hysteresis behaviour in perovskite solar cells arise due to the uncertainty and inconsistency observed in the JV curves. The true performance of the solar cells can only be quantified when we can comprehend the origin and take proper measures to remove the hysteresis behaviour. In recent reports, hysteresis free perovskite solar cells for conventional and inverted solar cells have been reported. The focus on fabrication process by optimizing the spin coating procedure and maintaining the glovebox conditions have helped in the cause [62].

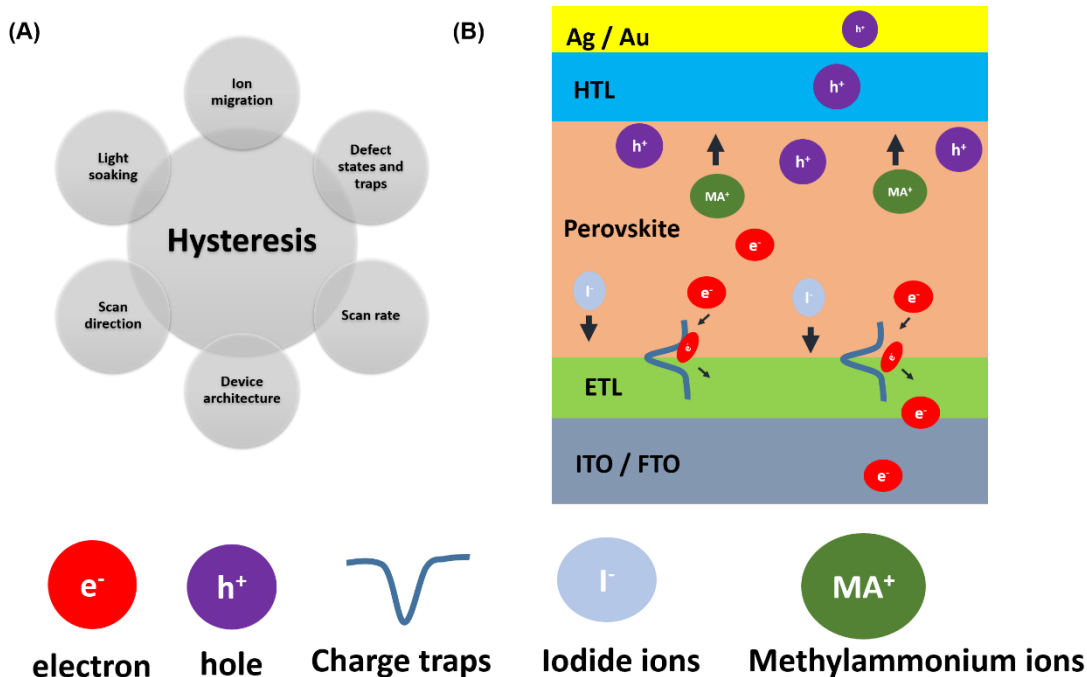


**Figure 7:** Schematic of (A) few reasons among many that affect the hysteresis behaviour in the perovskite solar cell, and (B) different processes that may contribute to the hysteresis behaviour in the perovskite solar cell.

## Toxicity

One of the grave challenges faced by lead based perovskite solar cells is the toxicity. Notwithstanding the impressive efficiencies achieved by the lead perovskite solar cells, the toxicity of lead is a major issue in many developing and some developed countries [104]. According to the report by the Centres for Disease Control and Prevention (CDC) in September 1995, children with blood lead level above  $80 \mu\text{g dL}^{-1}$  may suffer coma, convulsions, profound irreversible mental retardation, seizures and death. Even blood lead levels as low as  $10 \mu\text{g dL}^{-1}$  may cause deficits in neurobehavioural development and enzyme inhibition. In adults blood lead level in the range of  $100 - 120 \mu\text{g dL}^{-1}$  may result in encephalopathic signs and symptoms. Similarly, according to a report by the U.S. Department of health and human services, in August 2007, long term exposure to lead may cause in reduced performance of the human nervous system. It may cause anaemia, and damage to the kidneys in adults and children. It may cause miscarriage for pregnant woman. The reports from CDC and U.S. Department of health and human services are available on the internet for public to read.

To be able to use lead perovskites as absorber material for solar cells, it is imperative to understand the contribution of lead by the lead perovskites into the environment [105]. The lead escapes into the environment possibly due to the decomposition of perovskite (example MAPI) into lead iodide, methylamine, and hydrioc acid due to interaction with water [106]. The conclusion drawn by Hailegnaw et al. highlights the difference of spreading and aggregation of the leached lead iodide [106]. They conclude that if the lead iodide spread out and not concentrate due to strong adsorption then the effective contribution can be insignificant.

In attempts to counter the toxicity of lead through lead perovskite solar cells, research have been carried out to understand the moisture and lead perovskite interactions, and to stabilize the lead perovskites [107-111]. The toxic release of lead in the environment can be reduced with improved stability of the solar cells and the perovskite material itself. Encapsulation of the perovskite solar cells using polymers can potentially overcome water vulnerabilities [110]. Other than water, other issues like ion migration and thermal instabilities are also being addressed [112-115]. Since ion migration is unavoidable, it could be reduced by grain boundary management [116]. Therefore, with the concentration shifting towards improving stability of the lead perovskites, it would be possible to address the toxicity concerns and simultaneously work on improving the PCEs of the lead perovskite solar cells.

## **Solar cell working principles**

Solar cells work on the principle of photovoltaic effect, thereby acting like photovoltaic energy converters. Upon exposure to light, the solar cells produce electric current (I) which can be extracted up to a voltage (V). The process of conversion can be broken down into three steps. Firstly, the absorber layer, a semiconducting material, absorbs the light with energy ( $h\nu$ ) equal to and/or greater than its bandgap. Secondly, according to semiconductor chemistry, upon absorption of the light of previously mentioned energies, the electrons excite and jump from highest occupied molecular orbital (HOMO) level to the lowest unoccupied molecular orbital (LUMO) level within the absorbing semiconductor. This step can also be explained through semiconductor physics where the electrons absorb the energy and excite from the valence band (VB) to the conduction band (CB) of the semiconductor material. The electron and hole form a pair, known as exciton, and are separated by the bandgap but are still bound to each other due to coulomb's force. Thirdly, upon application

of voltage, these excitons can be separated, and the holes are collected at the anode and the electrons are collected at the cathode.

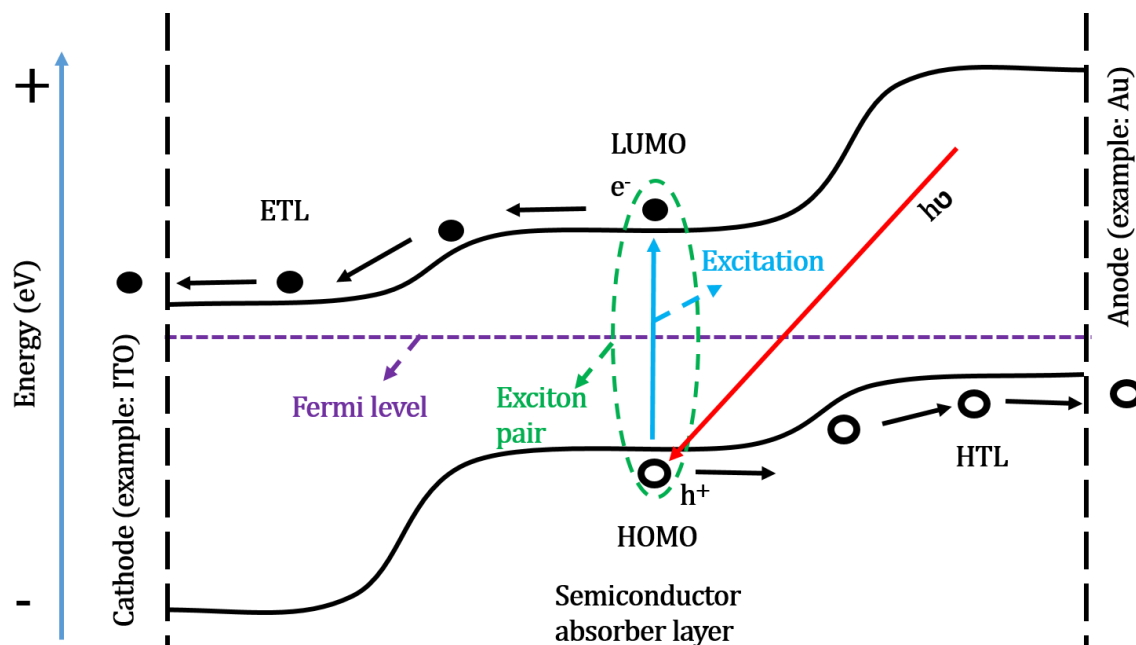


**Figure 8:** Energy band diagram for an n-i-p architecture based solar cell illustrating the light absorption and excitation (red and blue), exciton (green) formation and consequent separation and collection of the charge particles (black arrows). The electron transport layer (ETL) is responsible to carry the electrons ( $e^-$ ) to the cathode (e.g. indium doped tin oxide (ITO)) and the hole transport layer (HTL) is responsible to carry the holes ( $h^+$ ) to the anode (e.g. gold (Au)).

These processes are illustrated in the **Figure 8** for an n-i-p architecture based solar cell. During these processes, not all photoelectrons are converted into photocurrent. Some electrons are lost due to recombination. There can be different kinds of recombination losses depending upon in which region they occur. At any given time in excited state, an electron and a hole can recombine anywhere within the diode; such as traps, contacts, grain boundaries, and/or different interfaces. Upon recombination, energy is released. Depending upon the nature, it can be radiative recombination or non-radiative recombination. Therefore, an example corresponding to non-radiative recombination, causing release of non-radiative energy can be, heat. The released heat can eventually degrade the materials used in the solar cell. Some of the common types of recombinations are Shockley-Read-Hall recombination, recombination at contact (anode or cathode), and recombination at the space-charge region of the diode. These recombination pathways can be reduced by improving the material

quality (layer), and/or in some cases reducing the contact area. These losses directly affect the photocurrent density ( $J_{Ph}$ ) of the solar cell and the  $V_{OC}$  of the device. If these losses are controlled and reduced, the power conversion efficiency (PCE) of the device can be improved alongside the stability.

### Electrical characteristics

The solar cells act like a diode. In dark, the current density ( $J$ ,  $\text{mAcm}^{-2}$ ) – voltage ( $V$ ,  $V$ ) curve resembles to a diode's exponential behaviour as shown in **Figure 9A**. Here, current density, 'J', is the current 'I' (mA) measured across the solar cell with an area 'A' ( $\text{cm}^2$ ) as expressed in **equation 2**. In the presence of sunlight, the diode observes current due to the absorbed photons, also known as photocurrent ( $I_{ph}$ ). The photocurrent density can be, therefore, expressed as  $I_{ph}$  across the area 'A', denoted as  $J_{Ph}$ . The Shockley equation draws the relation between the ideal diode behaviour and the photocurrent density, for a solar cell, as shown in **equation 3**,

$$J = \frac{I}{A} \quad (2)$$

$$J = J_0 \left[ \exp\left(\frac{|e|V}{nkT}\right) - 1 \right] - J_{ph} \quad (3)$$

where, 'V' is the applied voltage, ' $J_0$ ' is the reverse saturation current density of the diode, ' $|e|$ ' is the absolute value of electron charge, 'n' is the ideality factor, 'k' is the Boltzmann constant and 'T' is the temperature.

### Power conversion efficiency, PCE, $\eta$

The power conversion efficiency is defined as the ratio of the output power of an energy conversion machine to the input power. Since solar cells are a form of energy convertors, they are characterized using their power conversion efficiencies (PCEs,  $\eta$ ). The PCE is calculated using parameters observed in the JV curve, as shown in **Figure 9B**. These parameters are illustrated in **Figure 9A-B** as short circuit current density ( $J_{SC}$ ), current density at maximum power point ( $J_{MPP}$ ),  $V_{OC}$ , voltage at maximum power point ( $V_{MPP}$ ) and fill factor (FF). These parameters allow us to calculate the PCE of the solar cell as shown in **equation 4**.



$$\eta \% = \frac{P_{out}}{P_{input}} \times 100\% = \frac{|J_{MPP}| \times V_{MPP}}{P_{input}} \times 100\% \quad (4)$$

$$= \frac{FF \times |J_{SC}| \times V_{OC}}{P_{input}} \times 100\%$$

$$FF = \frac{|J_{MPP}| \times V_{MPP}}{|J_{SC}| \times V_{OC}} \quad (5)$$

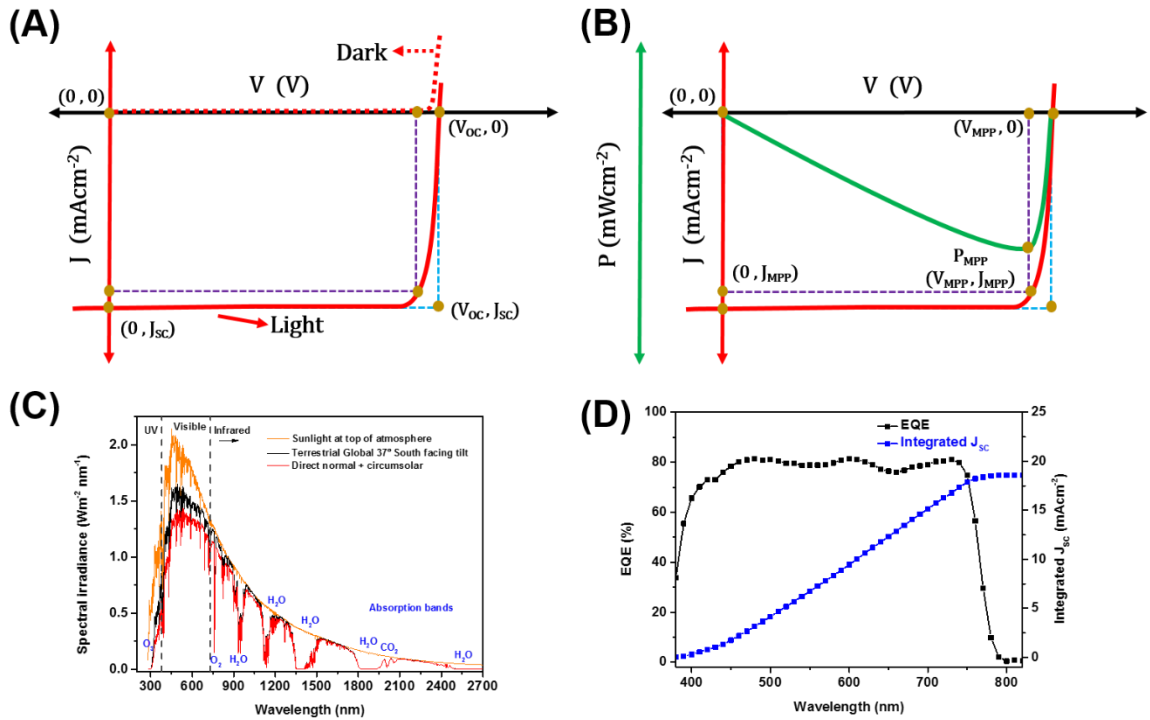


**Figure 9:** (A) Schematic of a Current Density – Voltage (JV) curve for a solar cell with dark (red dot) and light (red solid) measurements. The figure shows the coordinates for different parameters such as  $V_{OC}$ ,  $J_{SC}$  in the graph. (B) Schematic of a Power – Voltage curve for solar cell depicting the  $J_{MPP}$ ,  $V_{MPP}$  and the power curve (green). (C) The spectral irradiance graph showing the sunlight spectra before entering the earth's atmosphere (orange). The figure also shows the terrestrial global 37°C south facing tilt irradiance (black), direct normal and circumsolar irradiance (red), the ultraviolet, visible and infrared ranges, and the different absorption bands (blue) due to water ( $H_2O$ ), oxygen ( $O_2$ ), carbon dioxide ( $CO_2$ ) and the ozone ( $O_3$ ). (D) EQE curve (black) and integrated  $J_{SC}$  (blue) as a function of wavelength ( $\lambda$ ). In this figure the absorbance onset for the absorber material is depicted at  $\sim 770$  nm (normal

for lead halide perovskite based solar cell absorber material having bandgap of around 1.61 eV).

In **equation 4**, the  $P_{input}$  is the power supplied to the solar cell during JV measurements by simulating the spectrum of sunlight as a source with power of  $100 \text{ mWcm}^{-2}$ . This light source is calibrated using international standards to make it reliable and universally consistent.

Under illumination, the  $J_{SC}$  and  $J_{MPP}$  are negative values corresponding to the positive voltage values and are plotted in the fourth quadrant, as shown in **Figure 9A-B**, therefore, their absolute values are considered during calculation by applying modulus yielding positive values for  $\eta$  and FF as shown in **equation 4** and **equation 5** respectively.

### **Short circuit current density, $J_{SC}$**

The diode is said to be in a short-circuited condition when the diode observes current without experiencing any voltage. In dark condition, the diode does not experience any diode current density at 0 V and there is no other source of current in the system. However, when under illumination, the diode acts like a solar cell and photocurrent density is produced which can be measured. This is not the diode current density, as it can be observed only when the diode experiences voltage equal or more than the forward bias voltage. Therefore, the condition due to presence of photocurrent density in the diode can be explained as short circuited diode.

The current density measured in the diode at 0 V is known as short circuit current density,  $J_{SC}$ . In an ideal solar cell device,  $J_{SC}$  and  $J_{Ph}$  are equal, as the only current density observed by the diode under illumination is the photocurrent density. Therefore, a higher  $J_{SC}$  corresponds to a higher  $J_{Ph}$ .

### **Open circuit voltage, $V_{OC}$**

The open circuit voltage is the voltage at which the solar cell diode experiences  $0 \text{ mAcm}^{-2}$  current density. This is because the diode undergoes forward bias during voltage sweep and produces diode current density,  $J_D$ . This  $J_D$  is equal and opposite of the photocurrent density at a certain voltage, thereby cancelling out the net current density experienced by the solar cell diode. This voltage is termed as open circuit voltage,  $V_{OC}$ . It is the maximum voltage available to the solar cell. For  $J = 0 \text{ mAcm}^{-2}$  in **equation 3**,  $V_{OC}$  can be expressed as follows:

$$V_{OC} = \frac{nkT}{|e|} \ln \left( \frac{J_{ph}}{J_0} + 1 \right) \quad (6)$$

### Maximum power point, MPP

The power output of the solar cell is calculated by the following equation:

$$P = J \times V \quad (7)$$

During illumination and voltage sweep, the solar cell observes a maximum power point ( $P_{MPP}$ ) at which the product of  $J$  and  $V$  is maximum for their absolute values, as shown in **Figure 9**. These points are also known as current density at maximum power point ( $J_{MPP}$ ) and voltage at maximum power point ( $V_{MPP}$ ) respectively. Therefore, **equation 7** modifies to the following:

$$P_{MPP} = |J_{MPP}| \times V_{MPP} \quad (8)$$

In a solar cell, to estimate and evaluate the true performance during continuous illumination, the power at MPP,  $P_{MPP}$ , is tracked over a period. This allows to quantify the real-life performance of a solar cell. The  $P_{MPP}$  tracking can be performed by applying stress at the  $V_{MPP}$  of the solar cell and tracking the  $J_{MPP}$  over time alongside the other parameters. This allows to monitor the variation in  $P_{MPP}$  over time.

### Fill Factor, FF

In the JV curve, the  $J_{SC}$  and  $V_{OC}$  correspond to the points where the power is 0 and  $J_{MPP}$  and  $V_{MPP}$  correspond to the  $P_{MPP}$ . In an ideal case, the  $J_{SC}$  ( $= J_{ph}$ ) should be extracted from the solar cell up till the open circuit situation, thereby allowing a  $P_{MPP}$  of  $|J_{MPP}| \times V_{OC}$ . However, the solar cell observes resistance and recombination related losses and therefore the  $|J_{MPP}| < |J_{SC}|$ . This also leads to  $V_{MPP} < V_{OC}$ . The fill factor helps to describe the relation between the parameters as shown in **equation 5**. It can also be seen as the ratio of the areas of the purple rectangle and the blue rectangle from **Figure 9A-B**. The higher FF associates to higher  $P_{MPP}$  as higher FF narrows the gap between the  $J_{SC}$  and the  $J_{MPP}$ .

## External Quantum Efficiency, EQE

The External Quantum Efficiency (EQE) allows to calculate the short circuit density,  $J_{SC}$  of a solar cell with respect to the solar spectrum. The  $J_{Ph}$  generated due to the solar spectra translates into the  $J_{SC}$  as discussed earlier. Since the  $J_{Ph}$  is dependent up on the spectral response, to calculate  $J_{SC}$  it is necessary to use a standard spectrum for the calculation of the PCE. Therefore, AM1.5 G spectrum (**Figure 9C**) is the most commonly used standard spectrum for measuring spectral response of the solar cell and calculating the  $J_{SC}$ . It allows to circumvent the variation in solar spectrum observed across different parts of the world and any spectral losses due to bad weather or clouds.

The EQE of a solar cell is dependent up on the absorption of the photons that fall on the active layer. Therefore, EQE can be expressed as a function of the wavelength of the incident light and the corresponding photon flux. Therefore, the  $J_{SC}$  can be related and calculated with respect to the wavelength of the incident light, photon flux and the EQE as follows:

$$J_{SC} = \int_0^{\infty} |e|EQE(\lambda) \frac{\lambda}{hc} E_{\lambda}^{AM1.5G}(\lambda) d\lambda \quad (9)$$

where, ' $E_{\lambda}^{AM1.5G}$ ', is the spectral irradiance of AM1.5 G spectrum, ' $\lambda$ ' is the wavelength, ' $h$ ' is the Planck's constant, ' $c$ ' is the speed of light, and ' $e$ ' is the absolute value of the electron charge. The schematic for an EQE curve with integrated  $J_{SC}$  can be seen in the **Figure 9D**. The absorption onset of the EQE (black), in **Figure 9D**, corresponds to the bandgap of the absorber material. Lead halide perovskite absorber materials have a bandgap of around 1.61 eV which corresponds to the wavelength of around 770 nm. The bandgap ( $E_g$ ) and the corresponding wavelength ( $\lambda$ ) can be related in **equation 10**. The  $\lambda$  represents the absorption onset for the semiconducting absorber material. All wavelengths equal to this  $\lambda$  and all wavelengths less than this  $\lambda$  get absorbed by the semiconducting absorber material used in the solar cell.

$$E_g = \frac{hc}{\lambda} \quad (10)$$

## **Aim, motivation and objectives**

The aim of the work which is described in this thesis was to investigate the relationship between the HTLs and triple cation lead perovskite absorber layer.

The motivation to choose a lead perovskite having triple cation and double halide with the composition of  $\text{Cs}_{0.1}(\text{FA}_{0.83}\text{MA}_{0.17})_{0.9}\text{Pb}(\text{I}_{0.83}\text{Br}_{0.17})_3$  came from the publication by Saliba et al. [22]. They achieved PCEs > 20% in an n-i-p architecture based solar cells using spiro-OMeTAD as the HTL. Since spiro-OMeTAD has been an excellent HTL for lead perovskite solar cells, it has been, and still is, essential to understand the effect of spiro-OMeTAD on the lead perovskite solar cells [23,51]. Alongside, n-i-p architectures, p-i-n architecture based solar cells are being investigated. To understand the effect of HTLs on the performance of lead based perovskites, it is important to cover the p-i-n architecture based solar cells as well. Since solution based  $\text{NiO}_x$  layers have successfully helped to achieve higher PCEs in p-i-n architecture based solar cells the importance to comprehend the effect of  $\text{NiO}_x$  on lead perovskite has risen [49].

The research objectives cover careful selection of the perovskite composition used as an absorber layer, fabrication and electrical characterization of two different solar cell architectures namely n-i-p and p-i-n architectures. The electrical characterizations cover current density - voltage measurements, maximum power point tracking and external quantum efficiency measurements. The material characterizations cover ultra-violet and visible spectroscopy (absorbance and transmission), X-ray diffraction, and scanning electron microscopy. Special characterizations for better comprehension of the results that are dependent upon the progression of the work are contact angle measurements and x-ray photoelectron spectroscopy. Finally the objective also covers analysis of the data obtained to understand the relationship between the HTL and the triple cation lead perovskite absorber layer.

## **Insight to the thesis**

**Chapter 1: An Introduction to Perovskite materials and basics of Solar cells** is an attempt to get familiar with the properties of perovskite materials which are helpful to solar cells. It covers the origins of perovskite materials and their crystal structure. This chapter also introduces the different solar cell architectures, charge transport layers, and the state of the art for perovskite solar cells. The chapter by introducing the principle parameters to understand the working and to characterize a solar cell such as,  $V_{OC}$ ,  $J_{SC}$ , FF, PCE, and EQE.

**Chapter 2: Influence of different layers on the performance of solar cells in n-i-p architecture** discusses the impact of TCOs, CTLs, absorber layer composition, and metal BEs on the performance of the lead perovskite solar cells. In this process the chapter highlights the irreproducible nature of the solar cells dependent upon the fabrication process and conditions. Lead perovskite solar cells require meticulous and controlled glovebox conditions, solution preparation conditions and thin film deposition. The chapter show cases results that could not achieve state of the art PCEs due to various reasons that may relate to the fabrication process.

In **Chapter 3: Modification of NiO<sub>x</sub> hole transport layers with 4-bromobenzylphosphonic acid and its influence on the performance of lead halide perovskite solar cells** we discuss the influence of functionalized benzylphosphonic acid (Br-BPA) based self assembled monolayers (SAMs) on the NiO<sub>x</sub>/CsFAMA perovskite interface in a p-i-n architecture based solar cells. This chapter has been published in the Journal of Materials Science: Materials in Electronics. The chapter concludes that the Br-BPA SAM molecules help in improving the open circuit voltage of the device and therefore the overall power conversion efficiency.

In **Chapter 4: Benzyl phosphonic acid SAMs in p-i-n architecture** we investigate different functional groups such as Br-, F-, NH<sub>2</sub>-, NO<sub>2</sub>-, OCH<sub>3</sub>, and just BPA for NiO<sub>x</sub>/CsFAMA perovskite interface. We compare dip coating and spin coating techniques for the deposition of the SAM on the two differently deposited NiO<sub>x</sub> surface. We compare nanoparticles based NiO<sub>x</sub> thin films and sol-gel processed NiO<sub>x</sub> films. The chapter showcases the journey to achieve reliable and highly efficient solar cells. The results indicate a clear improvement of the  $V_{OC}$  of the devices upon introducing Br-BPA SAM molecules at the interface in either SAM deposition method.

In **Chapter 5: Conclusion and Outlook** summaries the thesis with an outlook. The highlights of each chapter are covered in this part along with potential topics which require exploring. The chapter briefly mentions the possible alternatives to lead based perovskites for solar cell application.

## References

1. T. Miyasaka, *Bull. Chem. Soc. Jpn.* **91**, 7, 1058 (2018)
2. S. Stølen, E. Bakken, C.E. Mohn, *Phys. Chem. Chem. Phys.* **8**, 429-447 (2006)
3. X. Zhao, W. Liu, W. Chen, S. Li, *Ceram. Int.* **41**, S111-S116 (2015)
4. K.O. Ogunniran, G. Murugadoss, R. Thangamuthu, P. Periasamy, *J. Alloys Compd.* **766**, 1014-1023 (2018)
5. Y. Li, H. Xu, P.-H. Chien, N. Wu, S. Xin, L. Xue, K. Park, Y.-Y. Hu, J.B. Goodenough, *Angew/ Chem. Int.* **57**, 8587-8591 (2018)
6. H. Kato, A. Kudo, *Catalysis Letters* **58**, 153-155 (1999)
7. H. Kato, A. Kudo, *J. Phys. Chem. B* **105** 4285-4292 (2001)
8. A. Kojima, K. Teshima, Y. Shirai, T. Miyasaka, *J. Am. Chem. Soc.* **131**, 6050 (2009)
9. J.-P.C.-Baena, A. Abate, M. Saliba, W. Tress, T.J. Jacobsson, M. Grätzel, A. Hagfeldt, *Energy Environ. Sci.*, **10**, 710-727 (2017)
10. M. Yavari, M.M.-Ardakani, S. Gholipour, N. Marinova, J.L. Delgado, S.-H. T.-Cruz, K. Domanski, N. Taghavinia, M. Saliba, M. Grätzel, A. Hagfeldt, W. Tress, *Adv. Energy Mater.* **8**, 1702719 (2018)
11. B. Philippe, M. Saliba, J.-P.C.-Baena, U.B. Cappel, S.-H.T.-Cruz, M. Grätzel, A. Hagfeldt, H. Rensmo, *Chem. Mater.* **29**, 3589 (2017)
12. M.I. Dar, M. Franckevičius, N. Arora, K. Redeckas, M. Vengris, V. Gulbinas, S.M. Zakeeruddin, M. Grätzel, *Chem. Phys. Lett.* **683**, 211 (2017)
13. M. Hadadian, J.-P.C.-Baena, E.K. Goharshadi, A. Ummadisingu, J.-Y. Seo, J. Luo, S. Gholipour, S.M. Zakeeruddin, M. Saliba, A. Abate, M. Grätzel, A. Hagfeldt, *Adv. Mater.* **28**, 8681 (2016)
14. A.D. Jodlowski, C.R.-Caremona, G. Grancini, M. Salado, M. Ralairisoa, S. Ahmad, N. Koch, L. Camacho, G. de Miguel, M.K. Nazeeruddin, *Nature Energy* **2**, 972 (2017)
15. S.D. Stranks, H.J. Snaith, *Nature Nanotechnology* **10**, 391 (2015)
16. M. Najafi, F.D. Giacomo, D. Zhang, S. Shanmugam, A. Senes, W. Verhees, A. Hadipour, Y. Galagan, T. Aernouts, S. Veenstra, R. Andriessen, *Small* **14**, 1702775 (2018)
17. N.J. Jeon, J.H. Noh, W.S. Yang, Y.C. Kim, S. Ryu, J. Seo, S.I. Seok, *Nature* **517**, 476 (2015)
18. G.E. Eperon, S.D. Stranks, C. Menelaou, M.B. Johnston, L.M. Herz, H.J. Snaith, *Energy Environ. Sci.* **7**, 982 (2014)



19. A. Amat, E. Mosconi, E. Ronca, C. Quarti, P. Umari, M.K. Nazeeruddin, M. Grätzel, F. De Angelis, *Nano Lett.* **14**, 3608 (2014)
20. M. Kulbak, D. Cahen, G. Hodes, *J. Phys. Chem. Lett.* **6**, 2452 (2015)
21. W.S. Yang, B.-W. Park, E.H. Jung, N.J. Jeon, Y.C. Kim, D. U. Lee, S.S. Shin, J. Seo, E.K. Kim, J.H. Noh, S.I. Seok, *Science* **356**, 1376 (2017)
22. M. Saliba, T. Matsui, J.-Y. Seo, K. Domanski, J.-P.C.-Baena, M.K. Nazeeruddin, S.M. Zakeeruddin, W. Tress, A. Abate, A. Hagfeldt, M. Grätzel, *Energy Environ. Sci.* **9**, 1989 (2016)
23. M. Saliba, T. Matsui, K. Domanski, J.-Y. Seo, A. Ummadisingu, S.M. Zakeeruddin, J.-P.C.-Baena, W.R. Tress, A. Abate, A. Hagfeldt, M. Grätzel, *Science* **354**, 206 (2016)
24. J.H. Noh, S.H. Im, J.H. Heo, T.N. Mandal, S.I. Seok, *Nano Lett.* **13**, 1764 (2013)
25. Q. Dong, Y. Fang, Y. Shao, P. Mulligan, J. Qiu, L. Cao, J. Huang, *Science* **347**, 967 (2015)
26. D. Shi, V. Adinolfi, R. Comin, M. Yuan, E. Alarousu, A. Buin, Y. Chen, S. Hoogland, A. Rothenberger, K. Katsiev, Y. Losovyj, X. Zhang, P.A. Dowben, O.F. Mohammed, E.H. Sargent, O.M. Bakr, *Science* **347**, 519 (2015)
27. S.D. Stranks, G.E. Eperon, G. Grancini, C. Menelaou, M.J.P. Alcocer, T. Leijtens, L.M. Herz, A. Petrozza, H.J. Snaith, *Science* **342**, 341 (2013)
28. V.M. Goldschmidt, *Naturwissenschaften.* **14**, 21, 477 (1926)
29. H. Megaw, *Nature.* **155**, 485 (1945)
30. W. Travis, E.N.K. Glover, H. Bronstein, D.O. Scanlon, R.G. Palgrave, *Chem. Sci.* **7**, 4548 (2016)
31. M. Johansson, P. Lemmens, *Crystallography and Chemistry of Perovskites, Handbook of Magnetism and Advanced Magnetic Materials, Wiley Online Library* (2007)
32. S. Chatterjee, A.J. Pal, *J. Mater. Chem. A* **6**, 3793 (2018)
33. J.I. Uribe, D. Ramirez, J.M.O.-Guillén, J. Osorio, F. Jaramillo, *J. Phys. Chem. C* **120**, 16393 (2016)
34. G. Kieslich, S. Sun, A.K. Cheetham, *Chem. Sci.* **5**, 4712 (2014)
35. G. Kieslich, S. Sun, A.K. Cheetham, *Chem. Sci.* **6**, 3430 (2015)
36. S.F. Hoefler, G. Trimmel, T. Rath, *Monatsh Chem* **148**, 795 (2017)
37. X. Guo, C. McCleese, C. Kolodziej, A.C.S. Samia, Y. Zhao, C. Burda, *Dalton Trans.* **45**, 3806 (2016)
38. T. Singh, T. Miyasaka, *Adv. Energy Mater.* **8**, 1700677 (2018)

39. D. Bi, W. Tress, M.I. Dar, P. Gao, J. Luo, C. Renevier, K. Schenk, A. Abate, F. Giordano, J.-P.C.-Baena, J.-D. Decoppet, S.M. Zakeeruddin, M.K. Nazeeruddin, M. Grätzel, A. Hagfeldt, *Sci. Adv.* **2**, e1501170 (2016)
40. T.J. Jacobsson, J.-P.C.-Baena, E.H. Anaraki, B. Philippe, S.D. Stranks, M.E.F. Bouduban, W. Tress, K. Schenk, J. Teuscher, J.-E. Moser, H. Rensmo, A. Hagfeldt, *J. Am. Chem. Soc.* **138**, 10331 (2016)
41. Y. Guo, K. Shoyama, W. Sato, Y. Matsuo, K. Inoue, K. Harano, C. Liu, H. Tanaka, E. Nakamura, *J. Am. Chem. Soc.* **137**, 15907 (2015)
42. M.I. Saidaminov, A.L. Abdelhady, G. Maculan, O.M. Bakr, *Chem. Commun.* **51**, 17658 (2015)
43. P.-W. Liang, C.-Y. Liao, C.-C. Chueh, F. Zuo, S.T. Williams, X.-K. Xin, J. Lin, A.K.-Y. Jen, *Adv. Mater.* **26**, 3748 (2014)
44. Y. Bai, S. Xiao, C. Hu, T. Zhang, X. Meng, Q. Li, Y. Yang, K.S. Wong, H. Chen, S. Yang, *Nano Energy* **34**, 58 (2017)
45. A.R. Pascoe, M. Yang, N. Kopidakis, K. Zhu, M.O. Reese, G. Rumbles, M. Fekete, N.W. Duffy, Y.-B. Cheng, *Nano Energy* **22**, 439-452 (2016)
46. F. Giordano, A. Abate, J.P.C.-Baena, M. Saliba, T. Matsui, S.H. Im, S.M. Zakeeruddin, M.K. Nazeeruddin, A. Hagfeldt, M. Grätzel, *Nat. Commun.* **7**, 10379 (2016)
47. M.A.-Jalebi, M.I. Dar, A. Sadhanala, S.P. Senanayak, F. Giordano, S.M. Zakeeruddin, M. Grätzel, R.H. Friend, *J. Phys. Chem. Lett.* **7**, 3264-3269 (2016)
48. J. Yang, K.M. Fransishyn, T.L. Kelly, *Chem. Mater.* **28**, 7344-7352 (2016)
49. W. Chen, Y. Wu, J. Fan, A. B. Djurišić, F. Liu, H.W. Tam, A. Ng, C. Surya, W.K. Chan, D. Wang, Z-B. He, *Adv. Energy Mater.* **8**, 1703519 (2018)
50. Z. Hawash, L.K. Ono, Y. Qi, *Adv. Mater. Interfaces* **5**, 1700623 (2018)
51. D. Shi, X. Qin, Y. Li, Y. He, C. Zhong, J. Pan, H. Dong, W. Xu, T. Li, W. Hu, J.-L. Brédès, O.M. Bakr, *Sci. Adv.* **2**, e1501491 (2016)
52. H.J. Snaith, M. Grätzel, *Appl. Phys. Lett.* **89**, 26114 (2006)
53. P. Vivo, J.K. Salunke, A. Priimagi, *Materials* **10**, 1087 (2017)
54. C.-C. Chueh, C.-Z. Li, A.K.-Y. Jen, *Energy Environ. Sci.* **8**, 1160-1189 (2015)
55. F. Shan, A. Liu, H. Zhu, W. Kong, J. Liu, B. Shin, E. Fortunato, R. Martins, G. Liu, *J. Mater. Chem. C.* **40**, 9438-9444 (2016)
56. C. Tanase, E.J. Meijer, P.W.M. Blom, D.M. de Leeuw, *Phys. Rev. Lett.* **91**, 216601 (2003)
57. Q. Wei, M. Mukaida, Y. Naitoh, T. Ishida, *Adv. Mater.* **25**, 2831-2836 (2013)

58. S. Weber, T. Rath, J. Mangalam, B. Kunert, A.M. Coclite, M. Bauch, T. Dimopoulos, G. Trimmel, *J. Mater. Sci: Mater. Electron.* **29**, 1847-1855 (2018)
59. M. Neophytou, J. Griffiths, J. Fraser, M. Kirkus, H. Chen, C.B. Nielsen, I. McCulloch, *J. Mater. Chem. C.* **5** 4940 (2017)
60. H.A. Abbas, R. Kottokkaran, B.Ganapathy, M. Samiee, L. Zhang, A. Kitahara, M. Noack, V.L. Dalal, *APL Mater.* **3** 016105 (2015)
61. Z. Liu, A. Zhu, F. Cai, L. Tao, Y. Zhou, Z. Zhao, Q. Chen, Y.-B. Cheng, H. Zhou, *J. Mater. Chem. A* **5**, 6597 (2017)
62. M. Saliba, J.-P. C.-Baena, C. M. Wolff, M. Stollerfoht, N. Phung, S. Albrecht, D. Neher, A. Abate, *Chem. Mater.* **30**, 4193-4201 (2018)
63. J. Cui, H. Yuan, J. Li, X. Xu, Y. Shen, H. Lin, M. Wang, *Sci. Technol. Adv. Mater.* **16**, 036004 (2015)
64. N.K. Elumalai, M.A. Mahmud, D. Wang, A. Uddin, *Energies* **9**, 861 (2016)
65. P. Gao, M. Grätzel, M.K. Nazeeruddin, *Energy Environ. Sci.* **7**, 2448 (2014)
66. F.C. Hanusch, E. Wiesenmayer, E. Mankel, A. Binek, P. Angloher, C. Fraunhofer, N. Giesbrecht, J.M. Feckl, W. Jaegermann, D. Johrendt, T. Bein, P. Docampo, *J. Phys. Chem. Lett.* **5**, 2791 (2014)
67. T.J. Jacobsson, J.-P.C.-Baena, M. Pazoki, M. Saliba, K. Schenk, M. Grätzel, A. Hagfeldt, *Energy Environ. Sci.*, **9**, 1706 (2016)
68. S. Adjokatse, H.-H. Fang, M.A. Loi, *Materials Today* **20**, 8 (2017)
69. Z.H. Bakr, Q. Wali, A. Fakharuddin, L.S.-Mende, T.M. Brown, R. Jose, *Nano Energy* **34**, 271 (2017)
70. S. Ameen, M.A. Rub, S.A. Kosa, K.A. Alamry, M.S. Akhtar, H.-S. Shin, H.-K Seo, A. M. Asiri, M.K. Nazeeruddin, *ChemSusChem* **9**, 10(2016)
71. T.S. Krasienapibal, T. Fukumura, Y. Hirose, T. Hasegawa, *Jpn. J. Appl. Phys.* **53**, 090305 (2014)
72. L. Forro, O. Chauvet, D. Emin, L. Zuppiroli, H. Berger, F. Lévy, *J. Appl. Phys.* **75**, 633 (1994)
73. Q. Jiang, X. Zhang, J. You, *Small* **14**, 1801154 (2018)
74. L. Xiong, Y. Guo, J. Wen, H. Liu, ZG. Yang, P. Qin, G. Gang, *Adv. Funct. Mater.* **28**, 1802757 (2018)
75. J.-I. Fujisawa, T. Eda, M. Hanaya, *Chemical Physics Letters* **685**, 23-26 (2017)
76. B. Hailegnaw, G. Adam, H. Heilbrunner, D.H. Apaydin, C. Ulbricht, N.S. Sariciftci, M.C. Scharber, *RSC. Adv.* **8**, 24836-24846 (2018)

77. W.S. Yang, J.H. Noh, N.J. Jeon, Y.C. Kim, S. Ryu, J. Seo, S.I. Seok, *Science* **348**, 1234 (2015)
78. E.H. Anaraki, A. Kermanpur, L. Steier, K. Domanski, T. Matsui, W. Tress, M. Saliba, A. Abate, M. Grätzel, A. Hagfeldt, J.-P.C.-Baena, *Energy Environ. Sci.* **9**, 3128 (2016)
79. H. Tan, A. Jain, O. Voznyy, X. Lan, F.P.G. de Arquer, J.Z. Fan, R. Q.-Bermudez, M. Yuan, B. Zhang, Y. Zhao, F. Fan, P. Li, L.N. Quan, Y. Zhao, Z.-H. Lu, Z. Yang, S. Hoogland, E.H. Sargent, *Science* **355**, 722 (2017)
80. S.S. Shin, E.J. Yeom, W.S. Yang, S. Hur, M.G. Kim, J. Im, J. Seo, J.H. Noh, S.I. Seok, *Science* **356**, 167 (2017)
81. M.A. Green, Y. Hishikawa, E.D. Dunlop, D.H. Levi, J.H.-Ebinger, M. Yoshita, A.W.Y. H.-Baillie, *Prog Photovolt Res Appl.* **27**, 3-12 (2019)
82. N.J. Jeon, H. Na, E.H. Jung, T.-Y. Yang, Y.G. Lee, G. Kim, H.-W. Shin, S.I. Seok, J. Lee, J. Seo, *Nature Energy* **3**, 682 (2018)
83. M.M. Tavakoli, M. Saliba, P. Yadav, P. Holzhey, A. Hagfeldt, S.M. Zakeeruddin, M. Grätzel, *Adv. Energy Mater.* **9**, 1802646 (2019)
84. W. Tress, N. Marinova, O. Inganäs, M.K. Nazeeruddin, S.M. Zakeeruddin, M. Grätzel, *Adv. Energy Mater.* **5**, 1400812 (2015)
85. Q. Jiang, Z. Chu, P. Wang, X. Yang, H. Liu, Y. Wang, Z. Yin, J. Wu, X. Zhang, J. You, *Adv. Mater.* **29**, 1703852 (2017)
86. Y. Wu, F. Xie, H. Chen, X. Yang, H. Su, M. Cai, Z. Zhao, T. Noda, L. Han, *Adv. Mater.* **29**, 1701073 (2017)
87. S. Ye, H. Rao, Z. Zhao, L. Zhang, H. Bao, W. Sun, Y. Li, F. Gu, J. Wang, Z. Liu, Z. Bian, C. Huang, *J. Am. Chem. Soc.* **139**, 7504 (2017)
88. W. Chen, F.-Z. Liu, X.-Y. Feng, A.B. Djurišić, W.K. Chan, Z.-B. He, *Adv. Energy Mater.* **7**, 1700722 (2017)
89. H.-S. Kim, J.-Y. Seo, H. Xie, M. L.-Cantu, S.M. Zakeeruddin, M. Grätzel, A. Hagfeldt, *ACS Omega* **2**, 9074 (2017)
90. E.L. Unger, E. T. Hoke, C.D. Bailie, W.H. Nguyen, A.R. Bowring, T. Heumüller, M.G. Christoforo, M.D. McGehee, *Energy Environ. Sci.* **7**, 3690 (2017)
91. W. Tress, N. Marinova, T. Moehl, S.M. Zakeeruddin, M.K. Nazeeruddin, M. Grätzel, *Energy Environ. Sci.* **8**, 995 (2015)
92. J. Wei, Y. Zhao, H. Li, G. Li, J. Pan, D. Xu, Q. Zhao, D. Yu, *J. Phys. Chem. Lett.* **5**, 3937 (2014)

93. N. Pellet, P. Gao, G. Gregori, T.-Y. Tang, M.K. Nazeeruddin, J. Maier, M. Grätzel, *Angew. Chem. Int. Ed.* **53**, 3151 (2014)
94. J. Schoonman, *Chemical Physics Letters*, **619**, 193 (2015)
95. J. Kim, S.-H. Lee, J.H. Lee, K.-H. Hong, *J. Phys. Chem. Lett.* **5**, 1312 (2014)
96. P. Decampo, J.M. Ball, M. Darwich, G.E. Eperon, H.J. Snaith, *Nature Commun.* **4**, 2761 (2014)
97. A.T. Barrows, A.J. Pearson, C.K. Kwak, A.D.F. Dunbar, A.R. Buckley, D.G. Lidzey, *Energy Environ. Sci.* **7**, 2944 (2014)
98. C. Zhao, B. Chen, X. Qiao, L. Luan, K. Lu, B. Hu, *Adv. Energy Mater.* **5**, 1500279 (2015)
99. N.K. Elumalai, A. Uddin, *Solar Energy Materials & Solar cells* **157**, 476 (2016)
100. J.-W. Lee, S.-G. Kim, S.-H. Bae, D.-K. Lee, O. Lin, Y. Yang, N.-G. Park, *Nano Lett.* **17**, 4270 (2017)
101. G.A. Nemnes, C. Besleaga, A.G. Tomulescu, A. Palici, L. Pintilie, A. Monolescu, I. Pintilie, *Solar Energy* **173**, 976 (2018)
102. H.-S. Kim, N.-G. Park, *J. Phys. Chem. Lett.* **5**, 2927 (2014)
103. G.A. Nemnes, C. Besleaga, V. Stancu, D.E. Dogaru, L.N. Leonat, L. Pintilie, K. Torfason, M. Ilkov, A. Manolescu, I. Pintilie, *J. Phys. Chem. C* **121**, 11207 (2017)
104. Q. Zhang, F. Hao, J. Li, Y. Zhou, Y. Wei, H. Lin, *Science and Technology of Advanced Materials* **19**, 425 (2018)
105. D. Fabini, *J. Phys. Chem. Lett.* **6**, 3546-3548 (2015)
106. B. Hailegnaw, S. Kirmayer, E. Edri, G. Hodes, D. Cahen, *J. Phys. Chem. Lett.* **6**, 1543-1547 (2015)
107. L. Zhang, M.-G. Ju, W. Liang, *Phys. Chem. Chem. Phys.* **18**, 23174 (2016)
108. M. Salado, L.C.-Bernal, L. Calió, A. Todinova, C.L.-Santos, S. Ahmad, A. Borrás, J. Idígoras, J.A. Anta, *J. Mater. Chem. A*, **5**, 10917 (2017)
109. Y. Fu, T. Wu, J. Wang, J. Zhai, M.J. Shearer, Y. Zhao, R.J. Hamers, E. Kan, K. Deng, X.-Y. Zhu, S. Jin, *Nano Lett.* **17**, 4405 (2017)
110. I. Hwang, I. Jeong, J. Lee, M.J. Ko, K. Yong, *ACS Appl. Mater. Interfaces* **7**, 17330 (2015)
111. Y. Wei, Z. Cheng, J. Lin, *Chem. Soc. Rev.* **48**, 310 (2019)
112. W. Zhou, Y. Zhao, X. Zhou, R. Fu, Q. Li, Y. Zhao, K. Liu, D. Yu, Q. Zhao, *J. Phys. Chem. Lett.* **8**, 4122 (2017)

113. N. Arora, M.I. Dar, A. Hunderhofer, N. Pellet, F. Schreiber, S.M. Zakeeruddin, M. Grätzel, *Science* **358**, 768 (2017)
114. P. Wang, X. Zhang, Y. Zhou, Q. Jiang, Q. Ye, Z. Chu, X. Li, X. Yang, Z. Yin, J. You, *Nature Comm.* **9**, 2225 (2018)
115. Y. Zong, Y. Zhou, Y. Zhang, Z. Li, L. Zhang, M.-G. Ju, M. Chen, S. Pang, X.C. Zeng, N.P. Padture, *Chem* **4**, 1404 (2018)
116. L. Meng, J. You, Y. Yang, *Nature Comm.* **9**, 5262 (2018)



# Chapter 2: Influence of different layers on the performance of solar cells in n-i-p architecture

---

*A bad neighbour is a misfortune as much as a good one is a great blessing...*

- Hesiod



## Introduction

The lead halide perovskite based solar cells have reached power conversion efficiencies (PCEs) greater than 23% with highest claim of 24.2% according to NREL efficiency chart [1-3]. Achieving PCEs above 20% for n-i-p architecture based solar cells became possible by introducing multi cation – multi halide system which allows manipulation and fine tuning of photovoltaic properties [4-18]. In 2016, Saliba et al. introduced a cesium, formamidinium, methylammonium based triple cation and iodine and bromide base double halide perovskite absorber material having a composition of  $\text{Cs}_x(\text{FA}_{0.83}\text{MA}_{0.17})_{1-x}\text{Pb}(\text{I}_{0.83}\text{Br}_{0.17})_3$  [17]. The importance to explore mixed cation and halide systems have stemmed to address concerns of stability against moisture and temperature. For example, pure formamidinium lead iodide (FAPbI<sub>3</sub>) has structures dependent upon the solvents and moisture conditions [13,19-21].

Other than the absorber layer, the efficiently performing solar cells can be achieved by optimizing and understanding the contribution of the other components involved in the solar cell architectures. The selection of transparent conducting oxide (TCO), electron transport layer (ETL), perovskite absorber layer, hole transport layer (HTL) and the metal electrode is crucial and depends upon their energy level alignments as shown (**Figure 2** and **Figure 3**) and discussed in the previous chapter [22-29]. This chapter draws comparison between different TCOs, perovskite deposition conditions, and HTLs for achieving efficient solar cells. Indium doped tin oxide (ITO) and fluorine doped tin oxide (FTO) have been excellent TCOs for perovskite solar cells and have been extensively used in n-i-p and p-i-n architectures [17,18,30]. FTO allows the possibility of high temperature treatments as required for processing titanium dioxide films [4-9,17,18]. Other than TCOs, comparison of HTLs allows the fair selection of appropriate layer of hole transportation. Spiro-OMeTAD has been responsible for highly efficient perovskite solar cells. However, the dopants involved in enhancing the hole mobility of these devices have also been damaging to the stability of perovskite [31-34]. According to Li et al., PbI<sub>2</sub> undergoes dissolution in tertbutylpyridine (TBP) and causes the perovskite to decompose [33]. Therefore, influence of dopant variations in spiro-OMeTAD along with comparison with poly[bis(4-phenyl)(2,4,6-trimethylphenyl)amine] (PTAA) was carried out in this work.

## **Materials and methods**

### **Sample and solar cell preparation**

All chemicals and solvents were used as purchased without any further purification. The mesoporous titanium dioxide paste DSL 30NR-D and formamidinium iodide was purchased from Greatcell Solar. Lead iodide, and lead bromide, were purchased from TCI, and Alfa Aesar, respectively. The other chemicals including cesium iodide and solvents were purchased from Merck (Sigma Aldrich).

### **Front contact**

In conventional architecture, indium doped tin oxide on glass substrates (g-ITO) or fluorine doped tin oxide on glass substrates (g-FTO) with substrate size of ( $15 \times 15 \times 1.1 \text{ mm}^3$ ) were used as anodes. These are transparent conducting oxides (TCOs). They both have surface resistances of  $15 \Omega \text{ cm}^2$  each. The substrates were cleaned in a three-step process. Firstly, the substrates were wiped using acetone, followed by an ultra-sonication bath in isopropanol for 10 min. The substrates were then dried using a nitrogen gun. Lastly, the substrates were treated with oxygen plasma for 3 min.

### **Titanium dioxide**

A compact titanium dioxide (cTiO<sub>2</sub>) solution was prepared by mixing titanium isopropoxide (70  $\mu\text{L}$ ), ethanolamine (55  $\mu\text{L}$ ), in 2-methoxyethanol (1 mL). The solution was spin coated onto the g-ITO substrates at 4000 rpm for 30 sec in a glovebox environment filled with N<sub>2</sub> gas. The layers were then annealed at 450°C for 45 min in air outside the glovebox. Further a mesoporous titanium dioxide (mpTiO<sub>2</sub>) solution was prepared by mixing a commercially bought mpTiO<sub>2</sub> paste in terpineol in the ratio of 1:2.5 w/w. The solution was stirred overnight to allow formation of a homogeneous mixture and desired consistency. The solution was spin coated on top of cTiO<sub>2</sub> with the same parameters as cTiO<sub>2</sub>.

The mpTiO<sub>2</sub> layer was doped using bis(trifluoromethylsulfonyl)imide lithium (LiTFSI) salt. The doping treatment was done using a 0.1 M solution of LiTFSI salt in acetonitrile. The spin coating steps were identical to cTiO<sub>2</sub> and mpTiO<sub>2</sub>. The layers were then annealed at 450°C for 30 min in air outside the glovebox.

## **CsFAMA perovskite**

The cesium, formamidinium, and methylammonium based triple cation lead halide perovskite absorber layer was adapted from Saliba et al. [17]. The final composition chosen was  $\text{Cs}_{0.1}(\text{FA}_{0.83}\text{MA}_{0.17})_{0.9}\text{Pb}(\text{I}_{0.83}\text{Br}_{0.17})_3$ . The precursor solution consisted of 1 M formamidinium iodide (FAI), 1.1 M  $\text{PbI}_2$ , 0.2 M methylammonium bromide (MABr), and 0.2 M  $\text{PbBr}_2$  in a mixed dimethyl formamide (DMF)/dimethyl sulfoxide (DMSO) solvent with a 4:1 volume ratio. To this solution, 1.5 M CsI in DMSO, was added to obtain a 10% Cs content. The final precursor solution was stirred overnight in inert conditions to allow sufficient reaction time. The solution was then filtered using a 0.45  $\mu\text{m}$  PTFE syringe filter prior to spin coating. The perovskite absorber layer was spin coated on the non-modified and modified glass/ITO/ $\text{NiO}_x$  substrates in a two-step spin coating process with 1000/6000 rpm for 10/20 s. In the last 5 s of spinning, chlorobenzene was dripped onto the substrate as an antisolvent. The substrates were annealed at 100 °C for 1 h. The thin film turns brown on application of anti-solvent and later black due to annealing. The black phase is the photoactive phase of the perovskite.

## **Spiro-OMeTAD**

A 70 mM 2,2',7,7'-tetrakis[*N,N*-di(4-methoxyphenyl)amino]-9,9'-spirobifluorene (spiro-OMeTAD) solution was prepared in chlorobenzene inside the glovebox. This solution was doped using LiTFSI salt, (tris(2-(1H-pyrazol-1yl)-4-tert-Butylpyridine)cobalt(III) bis(trifluoromethylsulfonyl)imide) (FK209 cobalt salt), and 4-tert-butylpyridine (TBP) in the molar ratio of 0.5:0.03:3.3. The above solution was then spin coated at 4000 rpm for 20 sec on the perovskite layer.

## **PTAA**

A 10 mg/mL poly[bis(4-phenyl)(2,4,6-trimethylphenyl)amine] (PTAA) solution was prepared in toluene inside the glovebox. The solution was doped by using 7.5  $\mu\text{L}$  of a 170 mg/mL solution of LiTFSI salt in acetonitrile. The above solution was coated on top of the perovskite at 4000 rpm for 20 sec.

## Gold (Au)

A 70-80 nm thin gold (Au) electrode was coated using thermal evaporator under very low pressure of about  $8 \times 10^{-6}$  bar. The size of each cell was defined using a  $0.09 \text{ cm}^2$  shadow mask.

## Characterization techniques

XRD was performed on a PANalytical Empyrean system using  $\text{Cu K}\alpha$  radiation. Ultraviolet-visible (UV-Vis) spectroscopy measurements were done using the UV/VIS Spectrometer – Lambda 35 by Perkin Elmer. The layer thicknesses were measured by surface profilometry using a DektakXT device by Bruker.

The current density – voltage (JV) curves of the solar cells were performed using Keithley 2400 source meter and a LabView-based software inside a glove box (nitrogen atmosphere). For the JV curves, the scan rates were adjusted to  $100 \text{ mVs}^{-1}$  in the forward (fwd) direction (-0.1 V to 1.5 V) and backward (bwd) direction (1.5 V to -0.1 V) for both light and dark measurements. In few cases the illumination area was defined using a shadow mask ( $0.0702 \text{ cm}^2$ ) and the light was provided by a Dedolight DLH500 lamp calibrated to an intensity of  $100 \text{ mWcm}^{-2}$  using a pyranometer from Kipp & Zonen. The External Quantum Efficiency (EQE) spectra were acquired using a MuLTImode 4 monochromator (Amko) equipped with a 75 W xenon lamp (LPS 210-U, Amko), a lock-in amplifier (Stanford Research Systems, Model SR830), and a Keithley 2400 source meter.

## Results and discussion

The UV-Vis transmission spectra for  $\sim 35 \text{ nm}$  and  $\sim 24 \text{ nm}$  thin  $\text{TiO}_2$  for compact and mesoporous layers respectively as shown in **Figure 10** indicate above 80% transmission of light. This allows significant amount of light to reach the absorber layer. Further, the CsFAMA perovskite was deposited onto the  $\text{cTiO}_2+\text{mpTiO}_2$  substrates. The yellow perovskite solution was spread onto the substrates and the black phase perovskite layer was obtained by dropping chlorobenzene as antisolvent on the spinning substrate followed by annealing. The antisolvent step allows the formation of black perovskite phase fitting for photovoltaic application. In **Figure 11** the XRD patterns for CsFAMA perovskites (with 10% Cs content) thin films prepared using solutions with DMF:DMSO in 4:1 and 1:4 ratios

show reflexes at  $2\theta$  equals  $14.12^\circ$  and  $28.44^\circ$  for (110) and (220) lattice planes for cubic crystal structure with mean crystal size of  $\sim 75$  nm and  $\sim 64$  nm respectively. These values were calculated using Scherrer's equation by measuring full width half maxima for the samples at  $2\theta$  equals  $14.12^\circ$ . The XRD patterns also indicate presence of cubic  $\text{PbI}_2$  in the perovskite films as indicated by  $2\theta$  equals  $12.67^\circ$  and  $12.69^\circ$  for ratios of 4:1 and 1:4 respectively. In **Figure 12**, the UV-Vis absorption spectra for CsFAMA prepared using 4:1 DMF:DMSO perovskite solvent ratio show an absorption onset at  $\sim 770$  nm which correspond to a bandgap of  $\sim 1.61$  eV [22].

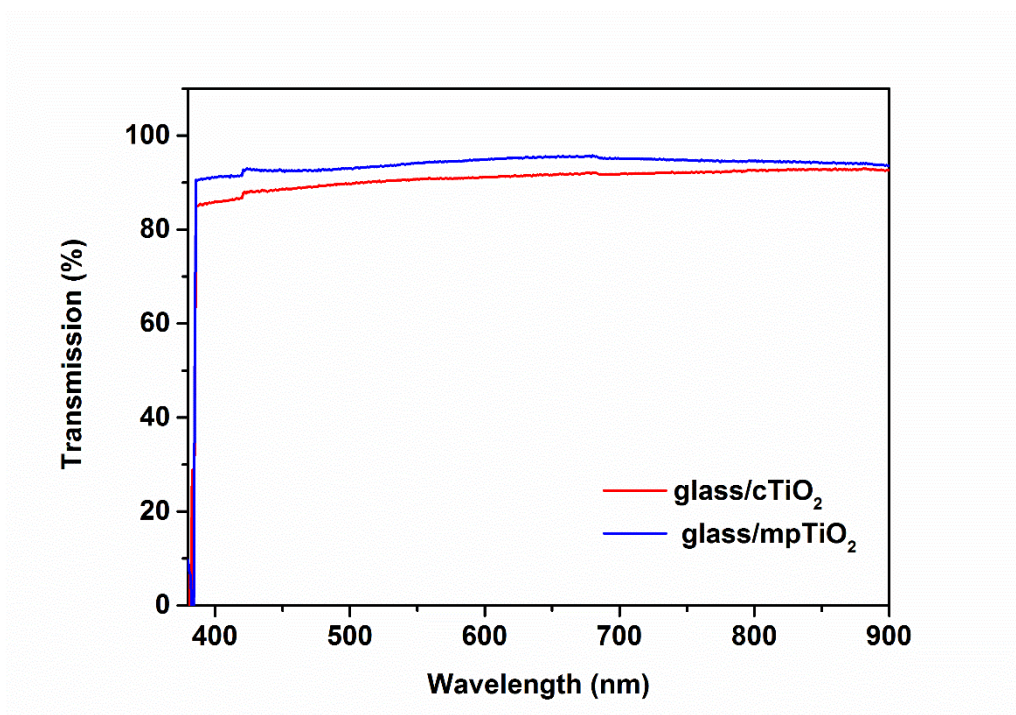


**Figure 10:** UV-Vis transmission spectra for  $\text{cTiO}_2$  and  $\text{mpTiO}_2$  on glass substrate with air as background.

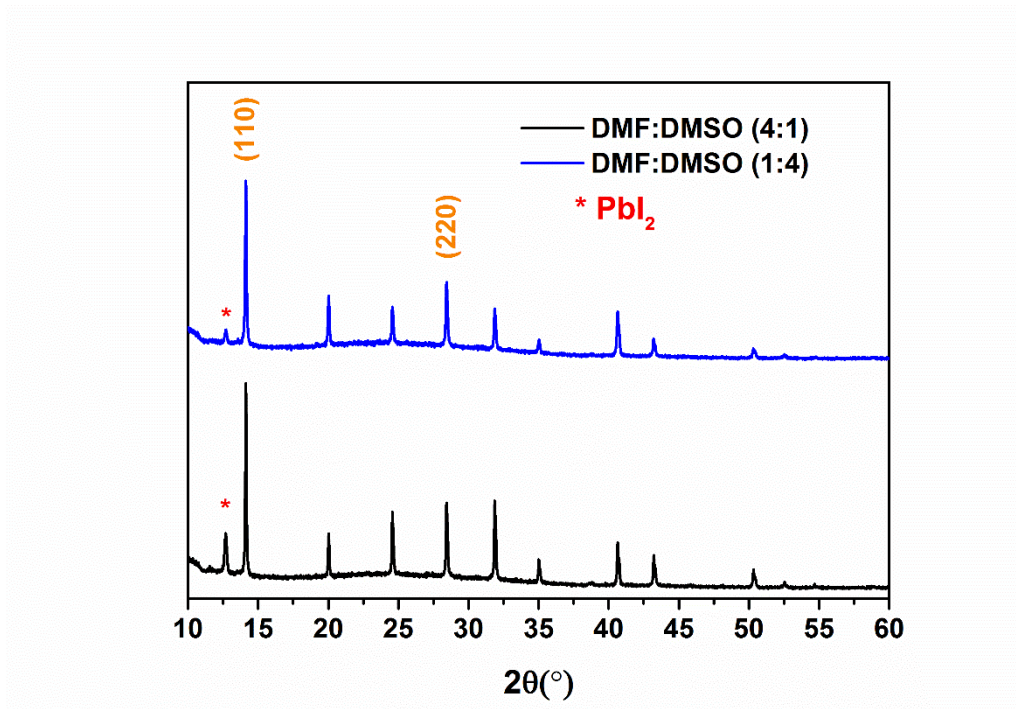


**Figure 11:** XRD reflexes for CsFAMA perovskite (10% Cs) thin films prepared using DMF:DMSO perovskite solution in ratios of 4:1 and 1:4.

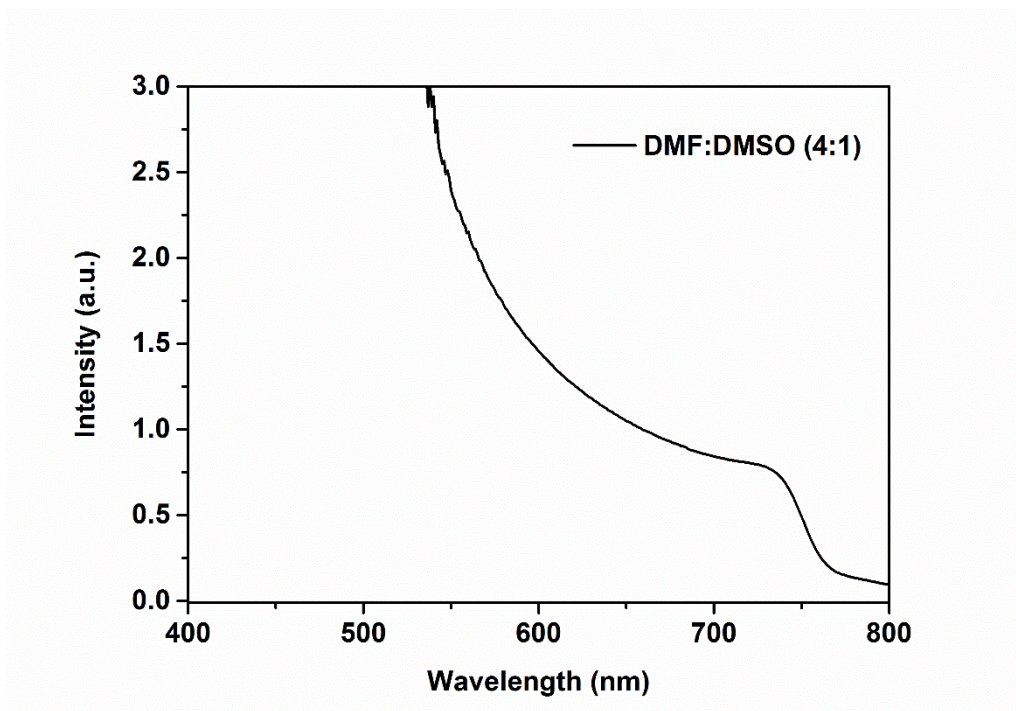


**Figure 12:** UV-Vis absorption spectra for CsFAMA perovskite (10% Cs) thin films prepared using DMF:DMSO solution in ratio of 4:1.

### **Influence of Cs content in CsFAMA perovskite absorber layer**

**Figure 13A-D** shows current density-voltage (JV) curves for perovskite composition  $\text{Cs}_x(\text{FA}_{0.83}\text{MA}_{0.17})_{1-x}\text{Pb}(\text{I}_{0.83}\text{Br}_{0.17})_3$  with  $x = 0, 0.05, 0.1, \text{ and } 0.15$  which correspond to 0%, 5%, 10% and 15% Cs content respectively. The solar cells were fabricated on ITO based TCO. The cells with 0% Cs (**Figure 13A**) content achieved 10.20% (11.55%) PCEs in forward (backward) sweep directions. The cells achieved  $V_{\text{OCs}}$  of 0.705 V (1.017 V) according to the measurements however, the JV curves suggest resistance issues during the forward sweep as indicated by the spikes in the voltage range of 0.4 V to 0.9 V. This behaviour could arise from defects in the perovskite absorber layer which may affect the diode. The series resistance ( $R_{\text{SER}}$ ) for the backward sweep direction in case of 0% Cs content was calculated to be  $6.36 \Omega \text{ cm}^2$  and the shunt resistance ( $R_{\text{SH}}$ ) was calculated to be  $172.72 \Omega \text{ cm}^2$  ( $2222.27 \Omega \text{ cm}^2$ ) in forward (backward) sweep directions. Due to irregular JV curve in the forward sweep direction, calculating  $R_{\text{SER}}$  was not possible. Further, these cells were irreproducible. For 5% Cs content ((**Figure 13B**) based solar cells, PCEs of 13.45% (14.72%) were obtained for champion cells resulting from  $V_{\text{OCs}}$  of 1.007 V (1.017 V) and FFs of 62.05% (74.28%). The  $R_{\text{SER}}$  and  $R_{\text{SH}}$  for the champion cells were calculated to be  $4.58 \Omega \text{ cm}^2$  ( $4.24 \Omega \text{ cm}^2$ ) and  $97.85 \Omega \text{ cm}^2$  ( $3144 \Omega \text{ cm}^2$ ) respectively. The mean (10 cells)  $V_{\text{OCs}}$  were  $0.922 \pm 0.018 \text{ V}$  ( $1.006 \pm 0.007 \text{ V}$ ) and FFs were  $58.95 \pm 7.15\%$  ( $73.25 \pm 1.48\%$ ). The difference of these values in forward and backward sweep directions suggest inconsistency as indicated by the standard deviation for FFs.

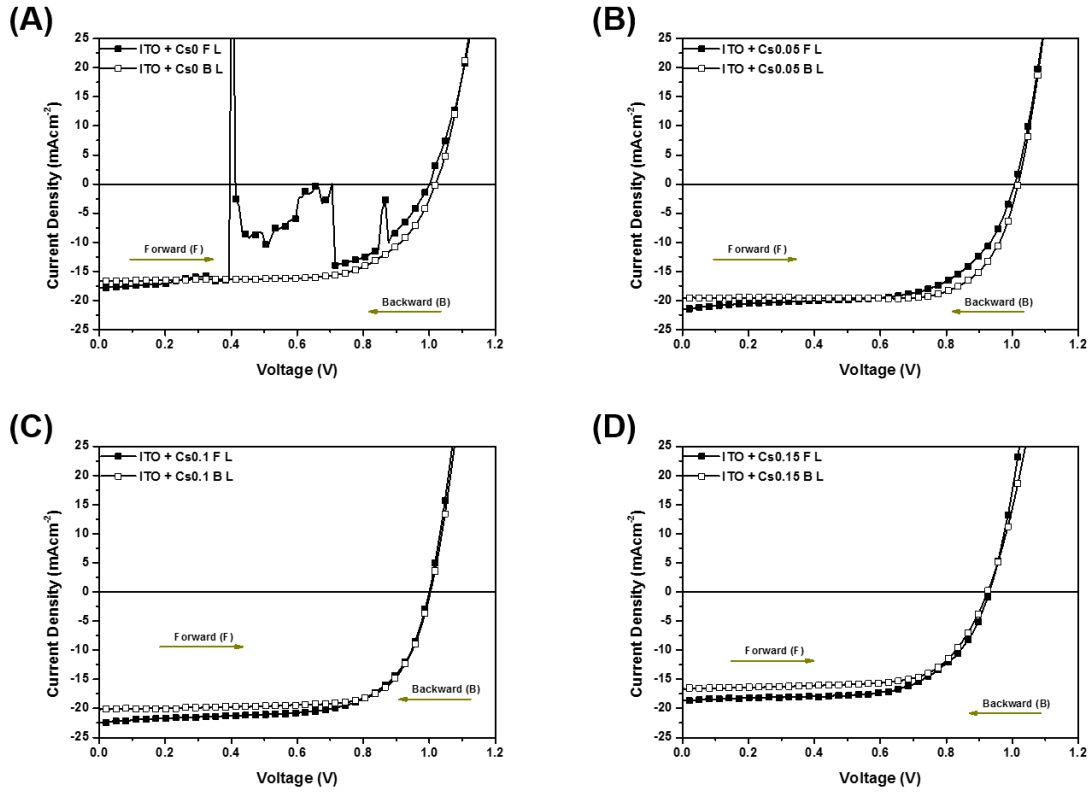


**Figure 13:** JV curves for solar cells with  $\text{Cs}_x(\text{FA}_{0.83}\text{MA}_{0.17})_{1-x}\text{Pb}(\text{I}_{0.83}\text{Br}_{0.17})_3$  with  $x =$  (A) 0 (0%), (B) 0.05 (5%), (C) 0.1 (10%), and (D) 0.15 (15%) Cs content in forward (F) and backward (B) sweep directions under illumination (Light, L). Cells were fabricated on ITO.

The JV curves for 10% Cs content (**Figure 13C**) PCEs of 14.70% (14.70%) with  $V_{\text{OCs}}$  of 0.997 V (1.007 V) and FFs of 65.70% (72.41%). The  $R_{\text{SER}}$  and  $R_{\text{SH}}$  for these cells were calculated to be  $3.58 \Omega \text{ cm}^2$  ( $3.92 \Omega \text{ cm}^2$ ) and  $120.19 \Omega \text{ cm}^2$  ( $1440.63 \Omega \text{ cm}^2$ ) respectively. These cells showed relatively less differences in performance for forward and backward sweep directions as indicated by the mean values (8 cells) of these devices as shown in **Table 1**. These differences in the forward and backward sweep directions (similar to 0% and 5% Cs) stem from hysteresis of the individual cells. The cells with 15% Cs content also showed hysteresis as can be seen in **Figure 13D**.

**Table 1:**  $V_{\text{OC}}$ , absolute  $J_{\text{SC}}$ , FF, and PCE values for light measurements for the graphs shown in **Figure 13**. The values are listed in forward (backward) sweep directions.

| $0.09 \text{ cm}^2$ | $V_{\text{oc}}$ (V) | $J_{\text{sc}}$ ( $\text{mAcm}^{-2}$ ) | FF (%) | PCE (%) |
|---------------------|---------------------|--|--------|---------|
|---------------------|---------------------|--|--------|---------|



|                          |                              |                            |                             |                            |
|--------------------------|------------------------------|----------------------------|-----------------------------|----------------------------|
| ITO + Cs <sub>0</sub>    | 0.705 (1.017)                | 17.91 (16.71)              | 80.41 (67.48)               | 10.20 (11.55)              |
| Mean (2 cells)           | 0.836±0.171<br>(1.007±0.014) | 17.30±0.86<br>(17.23±0.73) | 64.83±22.03<br>(61.26±8.79) | 9.01±1.69<br>(10.68±1.23)  |
| ITO + Cs <sub>0.05</sub> | 1.007 (1.017)                | 21.61 (19.58)              | 62.05 (74.28)               | 13.45 (14.72)              |
| Mean (10 cells)          | 0.922±0.018<br>(1.006±0.007) | 19.60±1.65<br>(18.69±0.54) | 58.95±7.15<br>(73.25±1.48)  | 11.56±2.22<br>(13.69±0.50) |
| ITO + Cs <sub>0.1</sub>  | 0.997 (1.007)                | 22.44 (20.18)              | 65.70 (72.41)               | 14.70 (14.70)              |
| Mean (8 cells)           | 0.987±0.009<br>(0.993±0.007) | 20.91±0.81<br>(19.22±0.56) | 66.73±1.21<br>(72.18±1.16)  | 13.77±0.70<br>(13.75±0.64) |
| ITO + Cs <sub>0.15</sub> | 0.926 (0.926)                | 18.65 (16.61)              | 64.39 (67.92)               | 10.86 (10.28)              |
| Mean (5 cells)           | 0.912±0.021<br>(0.886±0.038) | 18.04±1.51<br>(15.68±2.11) | 64.53±1.55<br>(64.42±2.75)  | 10.36±0.89<br>(8.87±1.68)  |

These devices with varying Cs content in the perovskite absorber layer fabricated on ITO substrates had poor reproducibility. This was evident by the fewer cells available for mean calculations. Therefore, to further the understanding of these devices, solar cells on FTO as TCO were chosen to identify any temperature effect on the performance of ITO.

Compared to ITO, solar cells with FTO as TCO for 0% Cs content showed similar PCEs for the champion device as shown in **Figure 14A** and **Table 2**. However, the mean (5 cells) PCEs of these devices fell to 5.93±3.33% (8.45±3.56%) due to lower FFs of 44.89±21.37% (51.36±14.84%) and V<sub>oc</sub>s 0.727±0.208 (0.866±0.192). The devices with 5% Cs content on FTO substrates achieved PCEs of 12.75% (13.43%), nonetheless the mean (4 cells) PCEs obtained were 7.63±3.78% (8.42±3.82%). Consistent with the ITO based cells, FTO based cells also exhibited lower sample size for mean value calculation as an outcome of poor reproducibility.

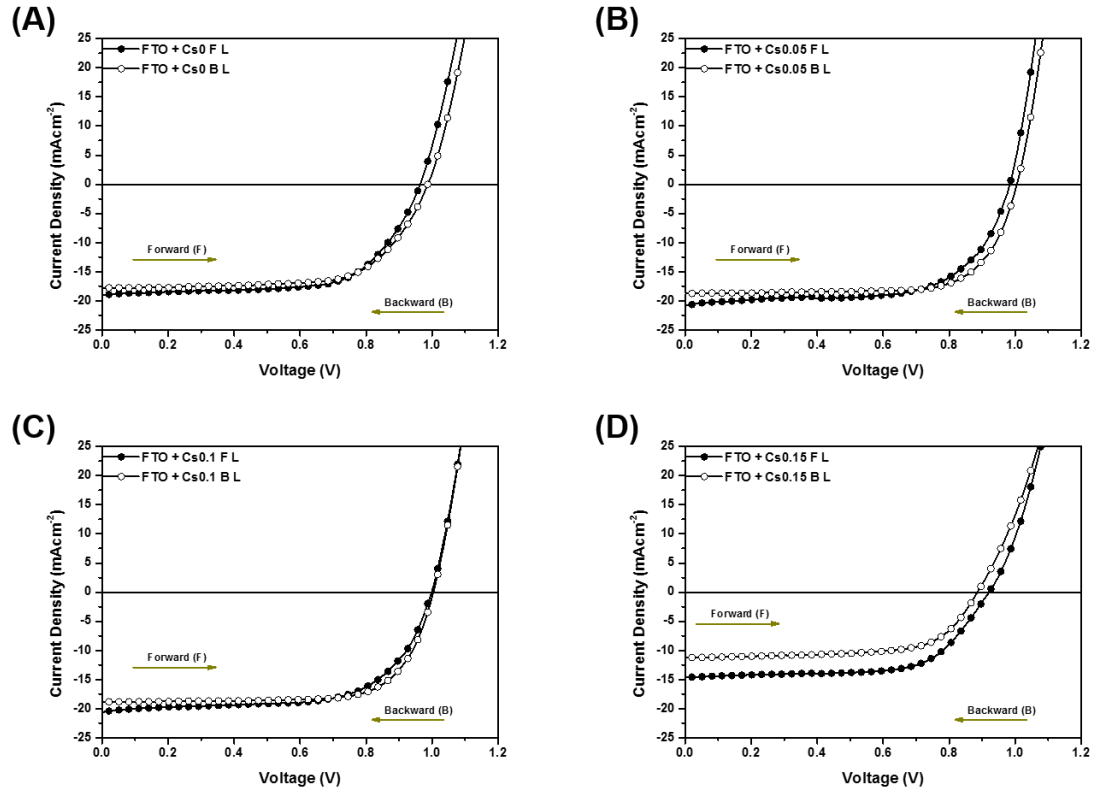


**Figure 14:** JV curves for solar cells with  $\text{Cs}_x(\text{FA}_{0.83}\text{MA}_{0.17})_{1-x}\text{Pb}(\text{I}_{0.83}\text{Br}_{0.17})_3$  with  $x =$  (A) 0 (0%), (B) 0.05 (5%), (C) 0.1 (10%), and (D) 0.15 (15%) Cs content in forward (F) and backward (B) sweep directions under illumination (Light, L). Cells were fabricated on FTO.

**Table 2:**  $V_{oc}$ , absolute  $J_{sc}$ , FF, and PCE values for light measurements for the graphs shown in **Figure 14**. The values are listed in forward (backward) sweep directions.

| $0.09 \text{ cm}^2$      | $V_{oc}$ (V)                               | $J_{sc}$ ( $\text{mAcm}^{-2}$ )          | FF (%)                                     | PCE (%)                                |
|--------------------------|--|--|--|--|
| FTO + $\text{Cs}_0$      | 0.967 (0.977)                              | 18.99 (17.76)                            | 65.10 (66.93)                              | 11.74 (11.42)                          |
| Mean (5 cells)           | $0.727 \pm 0.208$<br>( $0.866 \pm 0.192$ ) | $18.98 \pm 0.72$<br>( $18.16 \pm 1.03$ ) | $44.89 \pm 21.37$<br>( $51.36 \pm 14.84$ ) | $5.93 \pm 3.33$<br>( $8.45 \pm 3.56$ ) |
| FTO + $\text{Cs}_{0.05}$ | 0.977 (0.997)                              | 20.70 (18.78)                            | 63.71 (71.91)                              | 12.75 (13.43)                          |

|                          |                              |                            |                              |                           |
|--------------------------|------------------------------|----------------------------|------------------------------|---------------------------|
| Mean (4 cells)           | 0.909±0.056<br>(0.899±0.114) | 19.12±1.15<br>(18.89±0.25) | 42.46±16.21<br>(48.43±17.47) | 7.63±3.78<br>(8.42±3.82)  |
| FTO + Cs <sub>0.1</sub>  | 0.987 (0.997)                | 20.54 (18.88)              | 64.09 (72.20)                | 12.88 (13.42)             |
| Mean (4 cells)           | 0.939±0.052<br>(0.972±0.021) | 19.89±0.90<br>(18.42±0.52) | 46.72±12.24<br>(64.25±6.45)  | 8.81±3.00<br>(11.41±1.62) |
| FTO + Cs <sub>0.15</sub> | 0.906 (0.876)                | 14.64 (11.25)              | 65.26 (65.99)                | 8.65 (6.53)               |
| Mean (8 cells)           | 0.840±0.080<br>(0.832±0.034) | 13.99±0.93<br>(11.12±1.19) | 46.63±16.24<br>(54.75±7.70)  | 5.61±2.45<br>(5.08±1.06)  |

For further investigation 10% Cs content based Cs<sub>0.1</sub>(FA<sub>0.83</sub>MA<sub>0.17</sub>)<sub>0.9</sub>(I<sub>0.83</sub>Br<sub>0.17</sub>)<sub>3</sub> perovskite absorber layer was chosen as it showed consistently V<sub>OCS</sub> above 0.970 V as compared to other variations as observed and listed in **Figure 13**, **Figure 14**, **Table 1**, and **Table 2**.

**Figure 15** depicts JV curves for solar cells where a comparison between ITO and FTO was made for Cs<sub>0.1</sub>(FA<sub>0.83</sub>MA<sub>0.17</sub>)<sub>0.9</sub>(I<sub>0.83</sub>Br<sub>0.17</sub>)<sub>3</sub> perovskite absorber layer spin coated with 4000 and 6000 rpm. Solar cells with ITO as TCO (**Figure 15A**) and perovskite spun at 6000 rpm observed champion PCEs of 5.70% (9.81%) with V<sub>OCS</sub> of 0.969 V (1.010 V). As listed in **Table 3**, these cells exhibited maximum mean (16 cells) V<sub>OCS</sub> of 0.923±0.039 V (0.959±0.038 V) as expected based on previous results. The R<sub>SER</sub> and R<sub>SH</sub> calculated for the champion cells were 31.79 Ω cm<sup>2</sup> (15.20 Ω cm<sup>2</sup>) and 71.83 Ω cm<sup>2</sup> (561.79 Ω cm<sup>2</sup>) respectively. The cells also exhibited hysteresis. In comparison to the perovskite spun at 6000 rpm, the 4000 rpm based perovskite layers on ITO substrates had a champion cell with PCEs of 2.90% (5.38%) with V<sub>OCS</sub> of 0.929 V (0.929 V). The corresponding R<sub>SER</sub> and R<sub>SH</sub> were 41.68 Ω cm<sup>2</sup> (27.07 Ω cm<sup>2</sup>) and 144.02 Ω cm<sup>2</sup> (255.10 Ω cm<sup>2</sup>) respectively. The mean (21 cells) PCEs obtained were 1.89±0.57% (3.67±1.33%) with V<sub>OCS</sub> of 0.896±0.053 V (0.919±0.104 V).

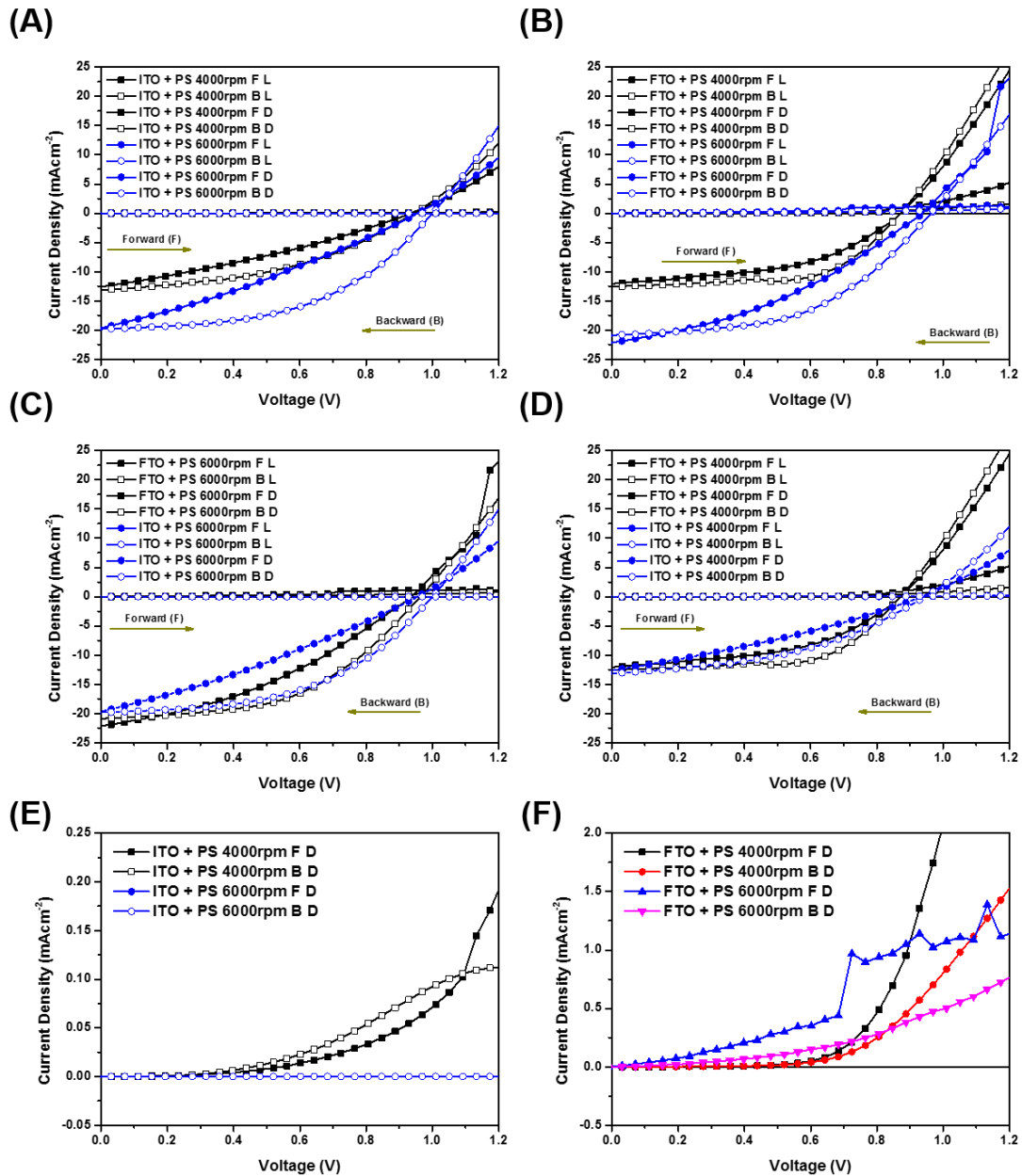


**Figure 15:** JV curves for (A) ITO and (B) FTO as TCO and perovskite (PS) spun at 4000 rpm and 6000 rpm. JV curves for FTO and ITO as TCO and PS spun at (C) 6000 rpm and (D) 4000 rpm. The graphs represent light and dark curves in forward sweep and backward sweep directions. (E and F) Zoomed in JV curves for dark conditions for ITO and FTO as TCO with PS spun at 6000 rpm and 4000 rpm.

These devices with spinning rate of 6000 rpm and 4000 rpm had poor FFs of  $28.06 \pm 3.10\%$  ( $46.24 \pm 9.37\%$ ) and  $31.15 \pm 3.71\%$  ( $49.81 \pm 10.09\%$ ) respectively owing to the poor resistance values causing the PCEs in range of 2-5% resulting from loss of  $J_{SC}$ .

**Table 3:**  $V_{OC}$ , absolute  $J_{SC}$ , FF, and PCE values for light measurements for the graphs shown in **Figure 15**. The values are listed in forward (backward) sweep directions.

| $0.09 \text{ cm}^2$ | $V_{OC}$ (V)                               | $J_{SC}$ ( $\text{mAcm}^{-2}$ )          | FF (%)                                    | PCE (%)                                |
|---------------------|--|--|---|--|
| ITO + PS 4000       | 0.929 (0.929)                              | 11.71 (12.96)                            | 26.83 (43.12)                             | 2.90 (5.38)                            |
| Mean (21 cells)     | $0.896 \pm 0.053$<br>( $0.919 \pm 0.104$ ) | $6.83 \pm 2.13$<br>( $7.87 \pm 2.30$ )   | $31.15 \pm 3.71$<br>( $49.81 \pm 10.09$ ) | $1.89 \pm 0.57$<br>( $3.67 \pm 1.33$ ) |
| ITO + PS 6000       | 0.969 (1.010)                              | 19.26 (19.84)                            | 25.97 (48.71)                             | 5.70 (9.81)                            |
| Mean (16 cells)     | $0.923 \pm 0.039$<br>( $0.959 \pm 0.038$ ) | $13.50 \pm 5.42$<br>( $13.16 \pm 5.13$ ) | $28.06 \pm 3.10$<br>( $46.24 \pm 9.37$ )  | $3.47 \pm 1.44$<br>( $5.80 \pm 2.69$ ) |
| FTO + PS 4000       | 0.888 (0.888)                              | 12.12 (12.54)                            | 46.33 (59.06)                             | 4.95 (6.52)                            |
| Mean (2 cells)      | $0.786 \pm 0.144$<br>( $0.786 \pm 0.144$ ) | $9.32 \pm 3.96$<br>( $9.85 \pm 3.81$ )   | $41.38 \pm 7.00$<br>( $51.62 \pm 10.52$ ) | $3.28 \pm 2.36$<br>( $4.33 \pm 3.09$ ) |
| FTO + PS 6000       | 0.929 (0.969)                              | 22.24 (20.93)                            | 36.47 (49.04)                             | 7.45 (9.83)                            |
| Mean (16 cells)     | $0.834 \pm 0.194$<br>( $0.832 \pm 0.235$ ) | $17.30 \pm 3.52$<br>( $16.90 \pm 3.02$ ) | $33.51 \pm 5.55$<br>( $45.64 \pm 8.03$ )  | $5.04 \pm 2.14$<br>( $6.72 \pm 3.08$ ) |

Similar to ITO, FTO based cells (**Figure 15B**) also exhibited poor solar cell performance owing to the  $R_{SER}$  and  $R_{SH}$  of the devices. The champion PCEs for perovskite spun at 6000 rpm and 4000 rpm were 7.45% (9.83%) and 4.95% (6.52%) respectively as listed in **Table 3**. These devices achieved FFs of 36.47% (49.04%) and 46.33% (59.06%) due to  $R_{SER}$  and  $R_{SH}$  resistances. The  $R_{SER}$  and  $R_{SH}$  of  $19.12 \Omega \text{ cm}^2$  ( $15.61 \Omega \text{ cm}^2$ ) and  $107.52 \Omega \text{ cm}^2$  ( $374.53 \Omega \text{ cm}^2$ ) were calculated for cells with perovskite spun at 6000 rpm. Similarly for perovskite spun at 4000 rpm the  $R_{SER}$  and  $R_{SH}$  were  $18.51 \Omega \text{ cm}^2$  ( $14.69 \Omega \text{ cm}^2$ ) and  $217.86 \Omega \text{ cm}^2$

(847.45  $\Omega \text{ cm}^2$ ). The high  $R_{\text{SER}}$  leads to loss of charges (holes and electrons) at the interfaces of the layers forming the solar cells. The acceptable range for the  $R_{\text{SER}}$  is less than 5  $\Omega \text{ cm}^2$ . The comparison of all the cells fabricated by spinning the perovskite at 4000 rpm were done with 6000 rpm irrespective of their TCOs, solar cells with spinning rate of 6000 rpm exhibited higher  $J_{\text{SC}}$  compared to 4000 rpm based cells. This is counterintuitive as thicker films are expected to attain higher  $J_{\text{SC}}$ s owing to the more absorption of light. This could be due to reduction in the film quality at lower rpm. The potential issue with the film quality is supported by the irregular dark curves resulting into poor diode characteristics of the device and consequential poor performance of the solar cells as seen in **Figure 15E-F**.

### **Influence of doping on spiro-OMeTAD HTL**

After evaluating ITO and FTO as TCOs and varying spin coating conditions for the perovskite absorber layer, cells with varying HTLs were fabricated. Spiro-OMeTAD and PTAA have been excellent HTLs for lead perovskite based solar cells. **Figure 16A and B** show JV curves for comparison between these HTLs and perovskite films prepared from solvents DMF and DMSO in the ratio of 1:4 and 4:1. The corresponding  $V_{\text{OC}}$ ,  $J_{\text{SC}}$ , FF, and PCE of the devices are listed in **Table 4**. As evident by the JV curves for spiro-OMeTAD, the cells display poor FFs originating from  $R_{\text{SER}}$ . The champion cell made from perovskite precursor solution with DMF:DMSO solvent ratio of 4:1 had  $R_{\text{SER}}$  of 143.06  $\Omega \text{ cm}^2$  (93.28  $\Omega \text{ cm}^2$ ) and  $R_{\text{SH}}$  of 735.29  $\Omega \text{ cm}^2$  (425.53  $\Omega \text{ cm}^2$ ). The high  $R_{\text{SER}}$  gives a parallel shape to the JV curves with regards to the voltage (x-axis) which represents loss of current density across the voltage sweep. The measured  $V_{\text{OC}}$ s of these devices were 1.031 V (1.047 V) which indicated the potential of these devices to reach higher PCEs if the FF improves. Similarly, the devices with 1:4 solution ratio also displayed poor mean (10 cells) PCE of  $3.24 \pm 2.24\%$  ( $4.80 \pm 3.21\%$ ) compared to  $7.72 \pm 1.77\%$  ( $8.41 \pm 2.20\%$ ) for 4:1 ratio.

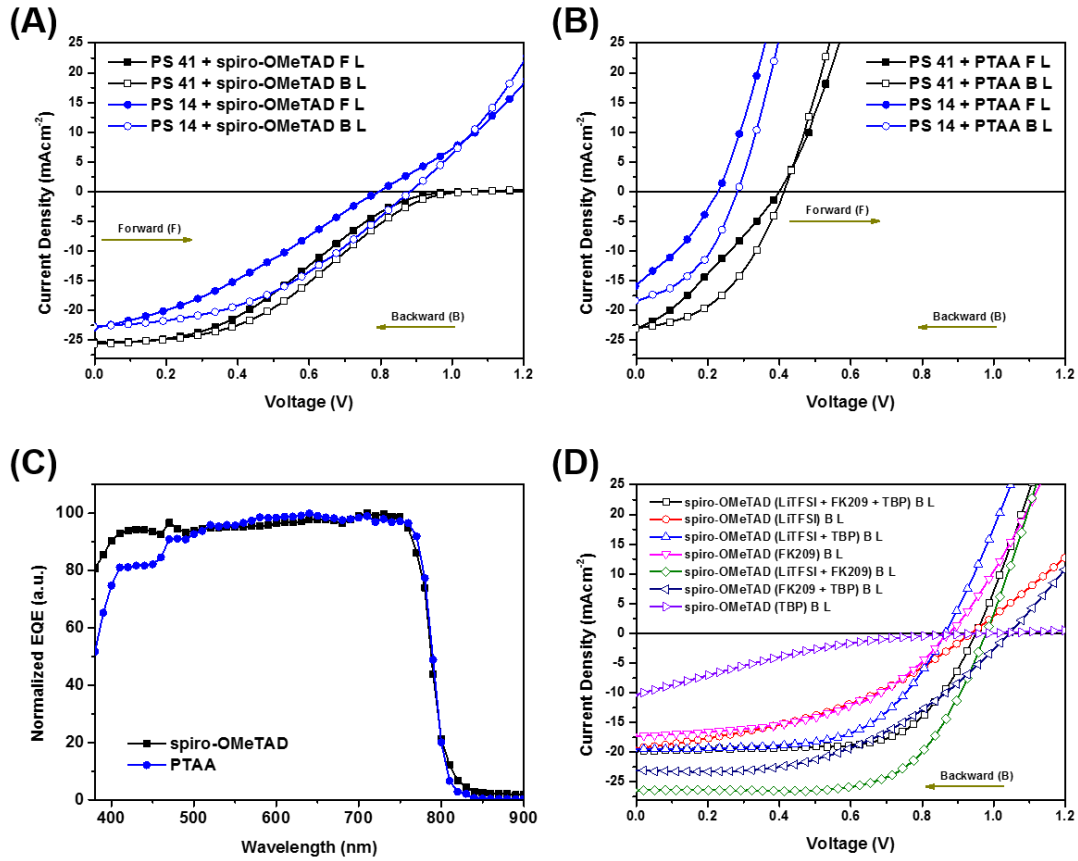


**Figure 16:** JV curves for (A) spiro-OMeTAD and (B) PTAA as HTL for perovskite absorber layer deposited using DMF:DMSO solution in ratios of 4:1 and 1:4. (C) Normalized (100%) EQE for comparing spiro-OMeTAD and PTAA based solar cells with 4:1 perovskite solvent ratio. (D) spiro-OMeTAD as HTL with different doping profiles using LiTFSI, FK209 and TBP as dopants with 4:1 perovskite solvent ratio.

The cells based on PTAA as HTL and perovskite solution with DMF:DMSO solvent ratio for 4:1 and 1:4 showed mean (10 cells)  $V_{OC}$ s of  $0.386 \pm 0.030$  V ( $0.328 \pm 0.103$  V) and  $0.141 \pm 0.067$  V ( $0.186 \pm 0.078$  V) resulting in PCEs of  $2.28 \pm 0.48\%$  ( $3.28 \pm 1.40\%$ ) and  $0.54 \pm 0.39\%$  ( $1.02 \pm 0.75\%$ ) respectively. Therefore, unmistakably, the PTAA based cells showed reduced  $V_{OC}$ s compared to spiro-OMeTAD based cells. The champion cells for perovskite solution with DMF:DMSO solvent ratio for 4:1 with PTAA showed  $V_{OC}$ s of 0.401 V (0.417 V) and PCEs of 2.74% (4.13 %). In contrast, the champion for DMF:DMSO solvent ratio of 1:4 had  $V_{OC}$ s of 0.223 (0.288) and PCEs of 1.15% (2.19%). These devices also showed poor FFs owing to the resistance. The  $R_{SER}$  and  $R_{SH}$  of the champion cells showed in **Figure 16B** for perovskite with DMF:DMSO solvent ratio of 4:1 were  $7.25 \Omega \text{ cm}^2$  ( $5.87 \Omega \text{ cm}^2$ ) and  $19.80 \Omega \text{ cm}^2$  ( $57.17 \Omega \text{ cm}^2$ ). In this case, the  $R_{SH}$  was low leading to the

current density loss across the voltage sweep. The combination of high  $R_{SH}$  and low  $R_{SER}$  allows the shaping of the JV curves which in turn causes better FF. The normalized EQE for spiro-OMeTAD and PTAA based cells for perovskite solution with DMF:DMSO solvent ratio of 4:1 display similar shape as shown in **Figure 16C**.

**Table 4:**  $V_{OC}$ , absolute  $J_{SC}$ , FF, and PCE values for light measurements for the graphs shown in **Figure 16A-B**. The values are listed in forward (backward) sweep directions.

| $0.09 \text{ cm}^2$  | $V_{OC}$ (V)                 | $J_{SC}$ ( $\text{mAcm}^{-2}$ ) | FF (%)                     | PCE (%)                  |
|----------------------|------------------------------|---------------------------------|----------------------------|--------------------------|
| PS 41 + spiro-OMeTAD | 1.031 (1.047)                | 25.28 (25.65)                   | 33.46 (36.40)              | 8.63 (9.57)              |
| Mean (10 cells)      | 0.923±0.227<br>(0.936±0.245) | 24.46±0.53<br>(24.77±0.55)      | 34.47±2.24<br>(36.58±1.94) | 7.72±1.77<br>(8.41±2.20) |
| PS 14 + spiro-OMeTAD | 0.789 (0.886)                | 22.95 (22.67)                   | 32.66 (42.18)              | 5.89 (8.40)              |
| Mean (10 cells)      | 0.522±0.245<br>(0.559±0.235) | 18.89±3.40<br>(18.80±3.53)      | 29.00±3.47<br>(40.23±5.99) | 3.24±2.24<br>(4.80±3.21) |
| PS 41 + PTAA         | 0.401 (0.417)                | 22.97 (23.01)                   | 29.99 (43.84)              | 2.74 (4.13)              |
| Mean (10 cells)      | 0.386±0.030<br>(0.328±0.103) | 23.94±1.07<br>(22.65±2.65)      | 30.98±2.37<br>(40.48±8.85) | 2.28±0.48<br>(3.28±1.40) |
| PS 14 + PTAA         | 0.223 (0.288)                | 15.88 (18.34)                   | 32.60 (41.51)              | 1.15 (2.19)              |
| Mean (10 cells)      | 0.141±0.067<br>(0.186±0.078) | 11.24±3.22<br>(13.60±3.46)      | 29.75±3.45<br>(35.25±4.80) | 0.54±0.39<br>(1.02±0.75) |



**Table 5:**  $V_{OC}$ , absolute  $J_{SC}$ , FF, and PCE values for light measurements for the graphs shown in **Figure 16C**. The values are listed in forward (backward) sweep directions.

| $0.09\text{ cm}^2$      | $V_{OC}$ (V)                 | $J_{SC}$ ( $\text{mAcm}^{-2}$ ) | FF (%)                     | PCE (%)                   |
|-------------------------|------------------------------|---------------------------------|----------------------------|---------------------------|
| LiTFSI +<br>FK209 + TBP | 0.937 (0.947)                | 21.51 (19.91)                   | 38.50 (65.98)              | 7.67 (12.40)              |
| Mean (9 cells)          | 0.929±0.015<br>(0.948±0.014) | 18.17±1.98<br>(16.54±2.14)      | 36.37±1.51<br>(59.15±4.08) | 6.09±0.87<br>(9.25±1.90)  |
| LiTFSI                  | 0.916 (0.937)                | 12.00 (19.34)                   | 18.72 (39.26)              | 2.05 (7.04)               |
| Mean (3 cells)          | 0.913±0.006<br>(0.923±0.012) | 11.28±0.62<br>(17.12±1.93)      | 20.14±1.29<br>(37.88±1.60) | 2.04±0.02<br>(5.92±0.98)  |
| LiTFSI + TBP            | 0.856 (0.866)                | 22.06 (19.48)                   | 41.58 (59.87)              | 7.82 (10.20)              |
| Mean (10 cells)         | 0.850±0.014<br>(0.852±0.013) | 18.53±1.89<br>(15.19±2.41)      | 39.33±4.54<br>(61.54±4.02) | 6.23±1.20<br>(8.00±1.46)  |
| FK209                   | 0.866 (0.876)                | 18.14 (17.33)                   | 29.36 (48.26)              | 4.58 (7.29)               |
| Mean (6 cells)          | 0.792±0.072<br>(0.799±0.101) | 17.74±1.07<br>(17.02±1.25)      | 26.86±1.95<br>(43.27±5.65) | 3.77±0.65<br>(5.88±1.38)  |
| LiTFSI +<br>FK209       | 0.916 (0.977)                | 28.92 (26.42)                   | 31.82 (66.03)              | 8.50 (17.53)              |
| Mean (9 cells)          | 0.831±0.053<br>(0.948.022)   | 25.39±2.66<br>(22.78±2.42)      | 27.39±3.16<br>(59.09±5.67) | 5.92±1.53<br>(13.19±2.93) |

|                 |                              |                            |                            |                          |
|-----------------|------------------------------|----------------------------|----------------------------|--------------------------|
| FK209 + TBP     | 1.037 (1.047)                | 24.64 (23.02)              | 33.08 (48.62)              | 8.40 (11.56)             |
| Mean (10 cells) | 0.987±0.085<br>(0.969±0.111) | 21.80±2.18<br>(21.57±0.92) | 30.64±4.37<br>(45.69±4.95) | 6.55±1.24<br>(9.58±2.19) |
| TBP             | 0.755 (0.977)                | 5.56 (10.31)               | 13.08 (16.40)              | 0.55 (1.64)              |
| Mean (12 cells) | 0.600±0.219<br>(0.624±0.393) | 4.48±1.89<br>(8.02±1.44)   | 16.17±5.50<br>(19.99±5.67) | 0.42±0.23<br>(0.89±0.53) |

To further explore the causes of poor and irreproducible performance of the solar cells across different TCOs, perovskite layer preparation methods, and HTLs, the focus was shifted to the impact of doping of spiro-OMeTAD using LiTFSI, FK209, and TBP for an ITO/Li:mpTiO<sub>2</sub>+cTiO<sub>2</sub>/CsFAMA perovskite (4:1)/spiro-OMeTAD/Au based solar cell. JV curves for solar cells with different doping profile for the HTL as are shown in **Figure 16D** and the values for V<sub>OCs</sub>, J<sub>SCs</sub>, FFs and PCEs are listed in **Table 5**. Seemingly, LiTFSI or FK209 or TBP individually alone are insufficient to achieve high performing devices. As evident from **Table 5**, LiTFSI doped spiro-OMeTAD HTLs showed mean (3 cells) PCEs of 2.04±0.02% (5.92±0.98%) with low J<sub>SCs</sub> of 11.28±0.62 mAcm<sup>-2</sup> (17.12±1.93 mAcm<sup>-2</sup>) and FFs of 20.14±1.29% (37.88±1.60%). The FK209 doped spiro-OMeTAD HTLs showed mean PCEs of 3.77±0.65% (5.88±1.38%) and TBP doped spiro-OMeTAD HTLs showed mean (12 cells) PCEs of 0.42±0.23% (0.89±0.53%). The devices suggest that LiTFSI or FK209 or TBP alone are insufficient to improve the performance of the HTL. As evident by the combination of LiTFSI+FK209 or LiTFSI+TBP or FK209+TBP, to achieve higher J<sub>SCs</sub> the dopants must work together. The effect can be seen for V<sub>OCs</sub> as well. The presence of FK209 with LiTFSI or TBP or both can lead to relatively better V<sub>OCs</sub> as shown by the champion cells for FK209+TBP combination with V<sub>OCs</sub> of 1.037 V (1.047 V). The improvement in the performance of the cells with the appropriate combination of the dopants can lead to increase in the hole mobility of the spiro-OMeTAD by an order of magnitude as mentioned in the previous chapter.

## Challenges during fabrication of lead perovskite solar cells

Due to the consistent irreproducibility of the experiments, drawing any pattern or conclusion was difficult. In 2018, Saliba et al. published an article explaining the fabrication process for n-i-p and p-i-n architecture based lead perovskite solar cells at the laboratory scale [35]. They listed the various issues that are expected to occur. For building highly efficient lead perovskite solar cells, in an n-i-p architecture using cTiO<sub>2</sub> and mpTiO<sub>2</sub>, the annealing step of these layers post deposition has been shown to have steps after spray pyrolysis and spin coating of cTiO<sub>2</sub> and mpTiO<sub>2</sub> respectively. Further, Saliba et al. highlight the stock solution method for preparing perovskite precursor solution for the cesium, formamidinium and methylammonium based triple cation perovskite. The stock solution preparation process includes the heat treatment of PbI<sub>2</sub> solution in DMF: DMSO (4:1) solvents at 180°C for 15 min and similar treatment is suggested for PbBr<sub>2</sub> for 5 min. The paper confesses that in the previous papers published so far, such heat treatments were not mentioned [17,18]. They also highlight the importance of glovebox conditions (water and oxygen < 1 ppm) during the spin coating of the perovskite onto the substrate. They also note the importance of antisolvent dripping technique to achieve smooth crack-free and hole-free layers. The impact of antisolvent dripping was observed in previous experiments and attempts to fabricate efficient solar cells.

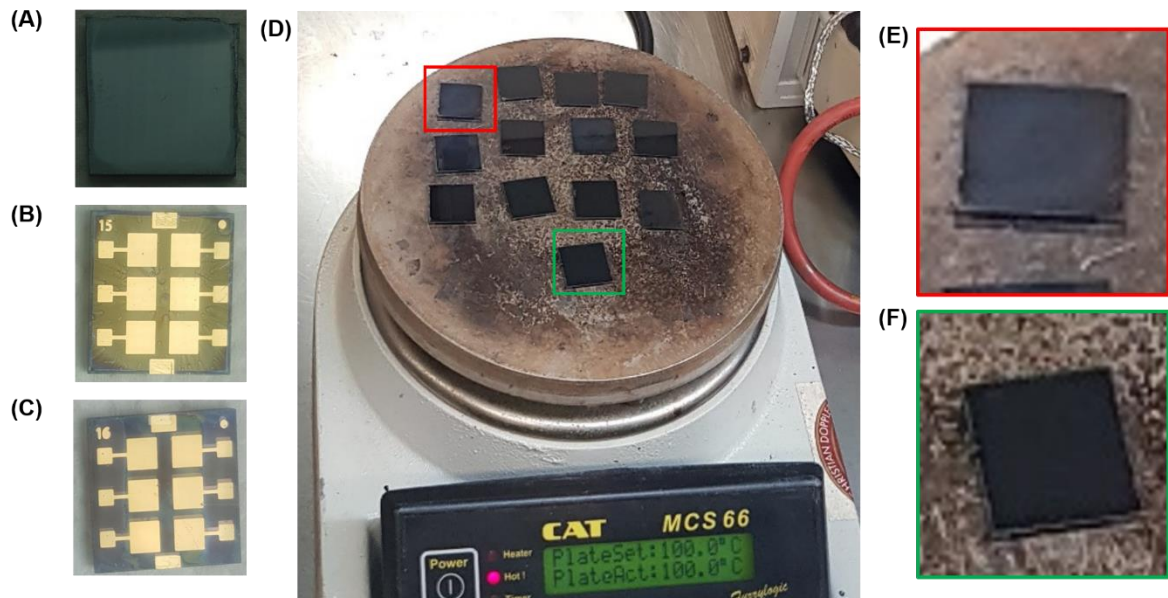


**Figure 17:** (A) perovskite (Cs<sub>0.1</sub>) on ITO/cTiO<sub>2</sub>+mpTiO<sub>2</sub> substrates after annealing at 100°C for 1 h. Solar cells with (B) PTAA and (C) spiro-OMeTAD as HTL. (D) Annealing

perovskite layers on hot plate at 100°C. (E) Greyish and (F) black perovskite layer during annealing.

**Figure 17A** shows the black phase lead perovskite films, **Figure 17B** and **C** are finished perovskite solar cells with PTAA and spiro-OMeTAD as HTLs. **Figure 17D** shows the annealing step for the perovskite layer at 100°C inside the glovebox. **Figure 17E-F** are perovskite films with and without grey appearance. The grey colour for perovskite layer could be due to the insufficient removal of the DMF or DMSO solvents from the yellow phase during spin coating. Therefore, the proper skilful application of the antisolvent must be done.

### Stock solution method

To verify if the method prescribed by Saliba et al. could lead to highly efficient lead perovskite solar cells in comparison to previous experiments, solar cells were fabricated using perovskite precursor solution prepared by stock solutions [35]. The cTiO<sub>2</sub> layer was annealed in stages of different temperatures as followed, stage1: ramp 5 min – 125°C – hold 5 min, stage2: ramp 15 min – 325°C – hold 5 min, stage3: ramp 5 min - 375°C – hold 5 min, and stage4: ramp 5 min – 450°C – hold 30min. The mpTiO<sub>2</sub> layer was spin coated and annealed similarly followed by LiTFSI salt for doping. For perovskite layers, the stock solutions of PbI<sub>2</sub> (1 g/1.446 mL) and PbBr<sub>2</sub> (1 g/1.816 mL) in DMF:DMSO (4:1) were prepared. The solutions were gradually heated till 180°C. The PbI<sub>2</sub> solution turned clear at ~100°C after 6 min and the PbBr<sub>2</sub> solution turned clear at ~100°C after 2 min. Another stock solution of CsI (1 g/2.566 mL) was prepared in DMSO. Further, FAI (0.1 g) and MABr (0.1 g) were weighed and mixed to the stock solutions (PbI<sub>2</sub> 0.468 mL and PbBr<sub>2</sub> 0.702 mL) to allow formation of FAPbI<sub>3</sub> and MABr<sub>3</sub>. Further as described CsI (0.016 mL), FAPbI<sub>3</sub> and MABr<sub>3</sub> were mixed to achieve Cs<sub>0.1</sub>(FA<sub>0.83</sub>MA<sub>0.17</sub>)<sub>0.9</sub>Pb(I<sub>0.83</sub>Br<sub>0.17</sub>)<sub>3</sub> perovskite composition.

**Figure 18A** shows the JV curves for ITO/cTiO<sub>2</sub>/mpTiO<sub>2</sub>/LiTFSI/perovskite/spiro-OMeTAD/Au solar cells prepared by using stock solutions of perovskite. The PCEs observed for the champion cells in forward (backward) sweep directions were 2.55% (2.66%). The lower PCEs are due to the low J<sub>SC</sub> of the devices at 5.05 mAcm<sup>-2</sup> (4.69 mAcm<sup>-2</sup>). The R<sub>SH</sub> calculated were 43.48 Ω cm<sup>2</sup> (1146.79 Ω cm<sup>2</sup>) and R<sub>SER</sub> were 28.04 Ω cm<sup>2</sup> (46.55 Ω cm<sup>2</sup>). The average values for the photovoltaic parameters are listed in **Table 6**. **Figure 18C-F** show graphs for V<sub>OC</sub>, J<sub>SC</sub>, FF, and PCE for one of the cells measured periodically (intervals of 15 min) during light soaking. The light soaking process is advantageous to the

solar cells due to possible reduction of trap states which in turn can increase the carrier diffusion length through the perovskite [36-41]. Light soaking is also known to affect the oxygen vacancies in the TiO<sub>2</sub> film which further improves conduction of the ETL and the charge extraction process [42-45]. Therefore, light soaking measurements were carried out to stimulate any positive change in the performance of these device. However, no significant change was observed as seen in the **Figure 18C-F**.

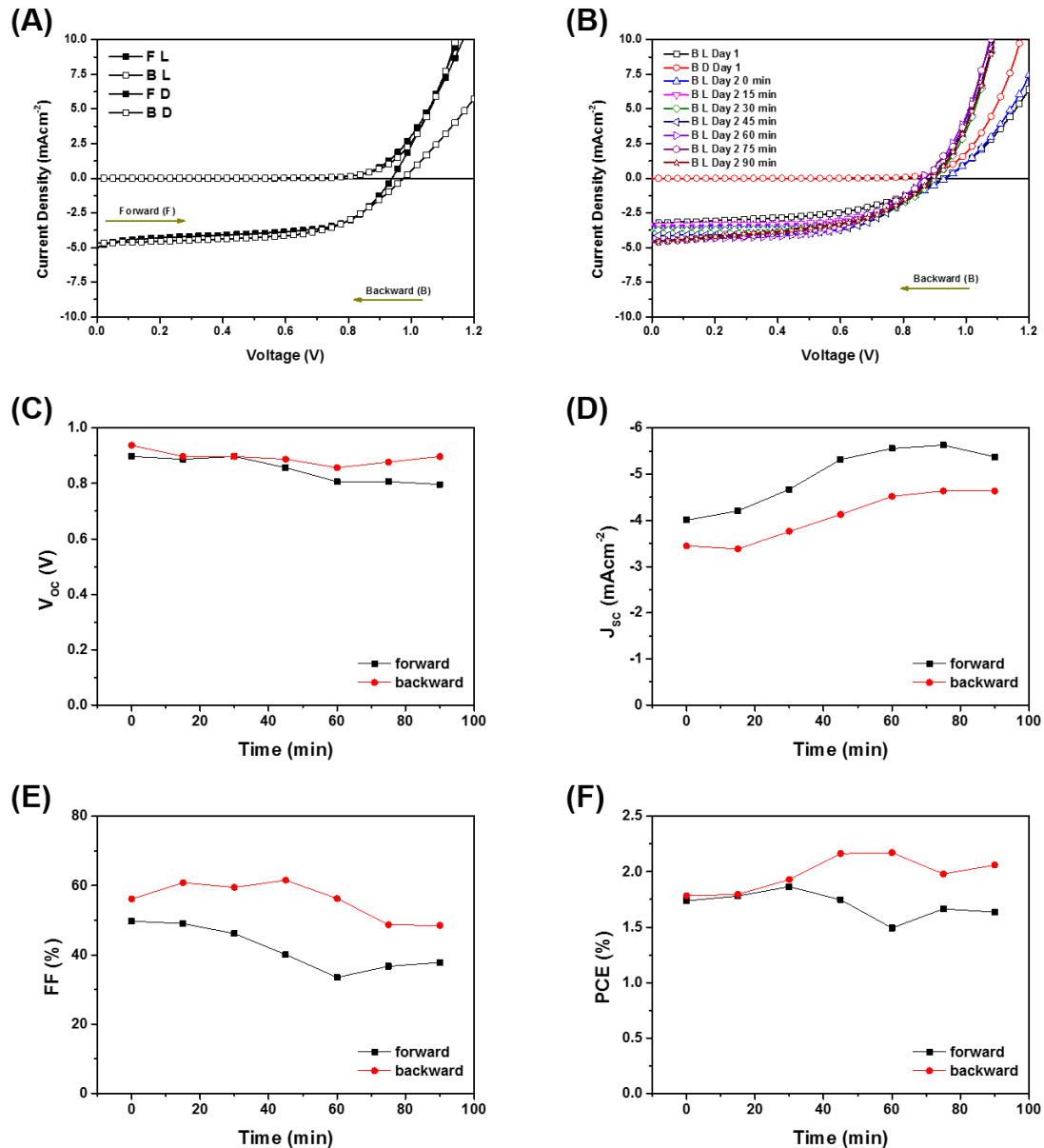


**Figure 18:** JV curves for (A) champion solar cell under light (L) and dark (D) conditions, and (B) backward sweep curves for comparing day 1, day 2 results with light soaking for 15 min, 30 min, 45 min, 60 min, 75 min, and 90 min, respectively. (C-F)  $V_{oc}$ ,  $J_{sc}$ , FF, and PCE trend after light soaking on day 2.

The stock solution based method suggested by Saliba et al. [35] led to solar cells with PCEs (mean 16 cells) of  $1.95\pm 0.32$  ( $1.93\pm 0.36$ ) which were inferior to few of the previous cases and similar to some. The poor performance did not improve through light soaking. Therefore, after trying out the prescribed methodology to achieve 20% efficient cells there is further requirement to optimize and improve the fabrication of n-i-p architecture based cell.

**Table 6:**  $V_{oc}$ , absolute  $J_{sc}$ , FF, and PCE values for light measurements for the graphs shown in **Figure 18A**. The values are listed in forward (backward) sweep directions.

| $0.0702\text{ cm}^2$ | $V_{oc}$ (V)                             | $J_{sc}$ ( $\text{mAcm}^{-2}$ )      | FF (%)                                 | PCE (%)                              |
|----------------------|--|--------------------------------------|--|--------------------------------------|
| Champion             | 0.938 (0.902)                            | 5.05 (4.69)                          | 54.67 (58.51)                          | 2.55 (2.66)                          |
| Mean (16 cells)      | $0.874\pm 0.025$<br>( $0.902\pm 0.031$ ) | $3.90\pm 0.48$<br>( $3.64\pm 0.51$ ) | $57.80\pm 0.52$<br>( $59.20\pm 0.57$ ) | $1.95\pm 0.32$<br>( $1.93\pm 0.36$ ) |

## Conclusion

In conclusion this chapter encapsulates the performance of lead perovskite solar cells in an n-i-p based architecture. The solar cells were fabricated using different TCOs (ITO and FTO) and HTLs (spiro-OMeTAD and PTAA). A cesium, formamidinium and methylammonium based triple cation perovskite ( $\text{Cs}_x(\text{FA}_{0.83}\text{MA}_{0.17})_{1-x}\text{Pb}(\text{I}_{0.83}\text{Br}_{0.17})_3$ ) was used as an absorber layer. A  $\text{cTiO}_2$  and LiTFSI doped  $\text{mpTiO}_2$  combination was used as ETL. The solar cells performance were spread to PCEs ranging between 0 – 13% dependent upon the combinations discussed in previous sections of this chapter. The common factor across the performance of these devices were the irreproducibility of the experiment. The publication by Saliba et al. discussing the stock solution method and other precautions necessary to produce highly efficient lead perovskite solar cells provide an insight and support the observations made during the experiments [35]. The difference in preparation method for perovskite precursor solution could be a cause of difference in performance. The thin film deposition of perovskite layer is dependent upon the efficacy of antisolvent dripping stage.

The improper dripping could lead to greyish layers and poor performance. The solar cells fabricated through the stock solution method also showed poor performance. They did not show any significant improvement due to light soaking. Therefore, further optimization and understanding of the fabrication process is required [46,47].

To further investigate the lead perovskite solar cells, the focus was shifted to p-i-n architecture based lead perovskite solar cells. The planar p-i-n architecture allows processing at low temperatures [48-50]. NiO<sub>x</sub> has proven to be an excellent HTL and these layers could be fabricated through various methods like solution processing, sputtering, and pulse laser deposition [51-57]. Further, NiO<sub>x</sub> allows the manipulation and tuning of properties for the benefit of photovoltaics and suitable for roll-to-roll fabrication [58-61].

## References

1. M.A. Green, Y. Hishikawa, E.D. Dunlop, D.H. Levi, J.H.-Ebinger, M. Yoshita, A.W.Y.H.-Baillie, *Prog Photovolt Res Appl.* **27**, 3-12 (2019)
2. N.J. Jeon, H. Na, E.H. Jung, T.-Y. Yang, Y.G. Lee, G. Kim, H.-W. Shin, S.I. Seok, J. Lee, J. Seo, *Nature Energy* **3**, 682 (2018)
3. <https://www.nrel.gov/pv/assets/pdfs/best-research-cell-efficiencies-190416.pdf>
4. J.-P.C.-Baena, A. Abate, M. Saliba, W. Tress, T.J. Jacobsson, M. Grätzel, A. Hagfeldt, *Energy Environ. Sci.*, **10**, 710-727 (2017)
5. M. Yavari, M.M.-Ardakani, S. Gholipour, N. Marinova, J.L. Delgado, S.-H. T.-Cruz, K. Domanski, N. Taghavinia, M. Saliba, M. Grätzel, A. Hagfeldt, W. Tress, *Adv. Energy Mater.* **8**, 1702719 (2018)
6. B. Philippe, M. Saliba, J.-P.C.-Baena, U.B. Cappel, S.-H.T.-Cruz, M. Grätzel, A. Hagfeldt, H. Rensmo, *Chem. Mater.* **29**, 3589 (2017)
7. M.I. Dar, M. Franckevičius, N. Arora, K. Redeckas, M. Vengris, V. Gulbinas, S.M. Zakeeruddin, M. Grätzel, *Chem. Phys. Lett.* **683**, 211 (2017)
8. M. Hadadian, J.-P.C.-Baena, E.K. Goharshadi, A. Ummadisingu, J.-Y. Seo, J. Luo, S. Gholipour, S.M. Zakeeruddin, M. Saliba, A. Abate, M. Grätzel, A. Hagfeldt, *Adv. Mater.* **28**, 8681 (2016)
9. A.D. Jodlowski, C.R.-Caremona, G. Grancini, M. Salado, M. Ralaiarisoa, S. Ahmad, N. Koch, L. Camacho, G. de Miguel, M.K. Nazeeruddin, *Nature Energy* **2**, 972 (2017)
10. S.D. Stranks, H.J. Snaith, *Nature Nanotechnology* **10**, 391 (2015)
11. M. Najafi, F.D. Giacomo, D. Zhang, S. Shanmugam, A. Senes, W. Verhees, A. Hadipour, Y. Galagan, T. Aernouts, S. Veenstra, R. Andriessen, *Small* **14**, 1702775 (2018)
12. N.J. Jeon, J.H. Noh, W.S. Yang, Y.C. Kim, S. Ryu, J. Seo, S.I. Seok, *Nature* **517**, 476 (2015)
13. G.E. Eperon, S.D. Stranks, C. Menelaou, M.B. Johnston, L.M. Herz, H.J. Snaith, *Energy Environ. Sci.* **7**, 982 (2014)
14. A. Amat, E. Mosconi, E. Ronca, C. Quarti, P. Umari, M.K. Nazeeruddin, M. Grätzel, F. De Angelis, *Nano Lett.* **14**, 3608 (2014)
15. M. Kulbak, D. Cahen, G. Hodes, *J. Phys. Chem. Lett.* **6**, 2452 (2015)
16. W.S. Yang, B.-W. Park, E.H. Jung, N.J. Jeon, Y.C. Kim, D.U. Lee, S.S. Shin, J. Seo, E.K. Kim, J.H. Noh, S.I. Seok, *Science* **356**, 1376 (2017)



17. M. Saliba, T. Matsui, J.-Y. Seo, K. Domanski, J.-P.C.-Baena, M.K. Nazeeruddin, S.M. Zakeeruddin, W. Tress, A. Abate, A. Hagfeldt, M. Grätzel, *Energy Environ. Sci.* **9**, 1989 (2016)
18. M. Saliba, T. Matsui, K. Domanski, J.-Y. Seo, A. Ummadisingu, S.M. Zakeeruddin, J.-P.C.-Baena, W.R. Tress, A. Abate, A. Hagfeldt, M. Grätzel, *Science* **354**, 206 (2016)
19. B. Conings, J. Drijkoningen, A. Ethirajan, J. Verbeeck, J. Manca, E. Masconi, F. De Angelis, H.G. Boyen, *Adv. Energy Mater.* **5**, 1500477 (2015)
20. R.K. Misra, S. Aharon, B. Li, D. Mogilyansky, I.V.-Fisher, L. Etgar, E.A. Katz, *J. Phys. Chem. Lett.* **6**, 326 (2015)
21. E.T. Hoke, D. J. Slotcavage, E.R. Dohner, A.R. Bowring, H.I. Karunadasa, M.D. McGehee, *Chem. Sci.* **6**, 613 (2015)
22. J. Cui, H. Yuan, J. Li, X. Xu, Y. Shen, H. Lin, M. Wang, *Sci. Technol. Adv. Mater.* **16**, 036004 (2015)
23. N.K. Elumalai, M.A. Mahmud, D. Wang, A. Uddin, *Energies* **9**, 861 (2016)
24. P. Gao, M. Grätzel, M.K. Nazeeruddin, *Energy Environ. Sci.* **7**, 2448 (2014)
25. F.C. Hanusch, E. Wiesenmayer, E. Mankel, A. Binek, P. Angloher, C. Fraunhofer, N. Giesbrecht, J.M. Feckl, W. Jaegermann, D. Johrendt, T. Bein, P. Docampo, *J. Phys. Chem. Lett.* **5**, 2791 (2014)
26. T.J. Jacobsson, J.-P.C.-Baena, M. Pazoki, M. Saliba, K. Schenk, M. Grätzel, A. Hagfeldt, *Energy Environ. Sci.*, **9**, 1706 (2016)
27. S. Adjokatse, H.-H. Fang, M. A. Loi, *Materials Today* **20**, 8 (2017)
28. Z.H. Bakr, Q. Wali, A. Fakharuddin, L.S.-Mende, T.M. Brown, R. Jose, *Nano Energy* **34**, 271 (2017)
29. S. Ameen, M.A. Rub, S.A. Kosa, K.A. Alamry, M.S. Akhtar, H.-S. Shin, H.-K Seo, A.M. Asiri, M.K. Nazeeruddin, *ChemSusChem* **9**, 10(2016)
30. J.H. Heo, H.J. Han, D. Kim, T.K. Ahn, S.H. Im, *Energy Environ. Sci.* **8**, 1602 (2015)
31. H.J. Snaith, M. Grätzel, *Appl. Phys. Lett.* **89**, 26114 (2006)
32. D. Shi, X. Qin, Y. Li, Y. He, C. Zhong, J. Pan, H. Dong, W. Xu, T. Li, W. Hu, J.-L. Brédès, O.M. Bakr, *Sci. Adv.* **2**, e1501491 (2016)
33. W. Li, H. Dong, L. Wang, N. Li, X. Guo, J. Li, Y. Qiu, *J. Mater. Chem. A* **2**, 13587 (2014)
34. Y. Shi, X. Wang, H Zhang, B. Li, H. Lu, T. Ma, C. Hao, *J. Mater. Chem. A* **3**, 22191 (2015)

35. M. Saliba, J.-P.C.-Baena, C.M. Wolff, M. Stollerfoht, N. Phung, S. Albrecht, D. Neher, A. Abate, *Chem. Mater.* **30**, 4193-4201 (2018)
36. X. Deng, X. Wen, J. Zheng, T. Young, C.F.J. Lau, J. Kim, M. Green, S. Huang, A.H.-Baillie, *Nano Energy* **46**, 356 (2018)
37. X. Wu, J. Wang, E.K. Yeow, *J. Phys. Chem. C* **120**, 12273 (2016)
38. S. Chen, X. Wen, S. Huang, F. Huang, Y.-B. Cheng, M. Green, A.H.-Baillie, *Sol. RRL*, **1**, 1600001 (2017)
39. C. Xhao, B. Chen, X. Qiao, L. Luan, K. Lu, B. Hu, *Adv. Energy Mater.* **5** 1500279 (2015)
40. S. Shao, M.A.-Aguye, L. Qin, L.-H. Lai, J. Liu, S.S. Adjokatse, F. Jahani, M.E. Kamminga, G.H.T. Brink, T. Palstra, *Energy Environ. Sci.* **9**, 2444 (2016)
41. J. Peng, Y. Sun, Y. Chen, Y. Yao, Z. Liang, *ACS Energy Lett.* **1**, 1000 (2016)
42. G. Liu, B. Yang, B. Liu, C. Zhang, S. Xiao, Y. Yuan, H. Xie, D. Niu, J. Yang, Y. Gao, C. Zhou, *Appl. Phys. Lett.* **111**, 153501 (2017)
43. T. Kuwabara, K. Yano, T. Yamaguchi, T. Taima, K. Takahashi, D. Son, K. Marumoto, *J. Phys. Chem. C* **119**, 5274 (2015)
44. S. Trost, A. Behrendt, T. Becker, A. Polywka, P. Görrn, T. Riedl, *Adv. Energy Mater.* **5**, 1500277 (2015)
45. J. Kim, G. Kim, Y. Choi, J. Lee, S.H. Park, K. Lee, *J. Appl. Phys.* **111**, 114511 (2012)
46. A.B. Djurišić, F.Z. Liu, H.W. Tam, M.K. Wong, A. Ng, C. Surya, W. Chen, Z.B. He, *Progress in Quantum Electronics* **53**, 1 (2017)
47. F. Wang, S. Bai, W. Tress, A. Hagfeldt, F. Gao, *npj Flexible Electronics* **2**, 22 (2018)
48. S. Ye, H. Rao, Z. Zhao, L. Zhang, H. Bao, W. Sun, Y. Li, F. Gu, J. Wang, Z. Liu, Z. Bian, C. Huang, *J. Am. Chem. Soc.* **139**, 7504-7512 (2017)
49. L. Hu, K. Sun, M. Wang, B. Yang, J. Fu, Z. Xiong, X. Li, X. Tang, Z. Zang, S. Zhang, L. Sun, M. Li, *ACS Appl. Mater. Interfaces* **9**, 43902-43909 (2017)
50. G. Adam, M. Kaltenbrunner, E.D. Glowacki, D.H. Apaydin, M.S. White, H. Heilbrunner, S. Tombe, P. Stadler, B. Ernecker, C.W. Klampfl, N.S. Sariciftci, M.C. Scharber, *Solar Energy Materials & Solar cells* **157**, 318-325 (2016)
51. J.H. Kim, P.-W. Liang, S.T. Williams, N. Cho, C.-C. Chueh, M.S. Glaz, D. S. Ginger, A.K.-Y. Jen, *Adv. Mater.* **27**, 695-701 (2015)
52. Z. Liu, A. Zhu, F. Cai, L. Tao, Y. Zhou, Z. Zhao, Q. Chen, Y.-B. Cheng, H. Zhou, *J. Mater. Chem. A* **5**, 6597-6605 (2017)
53. S. Weber, T. Rath, J. Mangalam, B. Kunert, A.M. Coclite, M. Bauch, T. Dimopoulos, G. Trimmel, *J. Mater. Sci: Mater. Electron.* **29**, 1847-1855 (2018)

54. X. Yin, Z. Yao, Q. Luo, X. Dai, Y. Zhou, Y. Zhang, Y. Zhou, S. Luo, J. Li, N. Wang, H. Lin, *ACS Appl. Mater. Interfaces* **9**, 2439-2448 (2017)
55. S.S. Mali, H. Kim, S.E. Shim, C.K. Hong, *Nanoscale* **8**, 19189-19194 (2016)
56. Z. Zhu, Y. Bai, T. Zhang, Z. Liu, X. Long, Z. Wei, Z. Wang, L. Zhang, J. Wang, F. Yan, S. Yang, *Angew. Chem. Int. Ed.* **53**, 12571-12575 (2014)
57. J.W. Jung, C.-C. Chueh, A.K.-Y. Jen, *Adv. Mater.* **27**, 7874-7880 (2015)
58. W. Chen, Y. Wu, J. Fan, A.B. Djurišić, F. Liu, H.W. Tam, A. Ng, C. Surya, W.K. Chan, D. Wang, Z.-B. He, *Adv. Energy Mater.* **8**, 1703519 (2018)
59. W. Chen, F.-Z. Liu, X.-Y. Feng, A. B. Djurišić, W.K. Chan, Z.-B. He, *Adv. Energy Mater.* **7**, 1700722 (2017)
60. H.-S. Kim, J.-Y. Seo, H. Xie, M. L.-Cantu, S.M. Zakeeruddin, M. Grätzel, A. Hagfeldt, *ACS Omega* **2**, 9074-9079 (2017)
61. J. Zheng, L. Hu, J. S. Yun, M. Zhang, C. F. J. Lau, J. Bing, X. Deng, Q. Ma, Y. Cho, W. Fu, C. Chen, M. A. Green, S. Huang, A. W. Y. H.-Baillie, *ACS Appl. Energy Mater.* **1**, 561-570 (2018)



# Chapter 3: Modification of NiO<sub>x</sub> hole transport layers with 4-bromobenzylphosphonic acid and its influence on the performance of lead halide perovskite solar cells

---

*The common facts of today are the products of yesterday's research...*

- *Duncan MacDonald*

This chapter was originally published in the Journal of Materials Science: Materials in Electronics.

J. Mangalam, T. Rath, S. Weber, B. Kunert, T. Dimopoulos, A. Fian, G. Trimmel

J. Mater. Sci.: Mater. Electron. (2019)

DOI: 10.1007/s10854-019-01294-0

Reproduced with permission from Springer Nature.

<http://creativecommons.org/licenses/by/4.0/>



## **Abstract**

Lead halide perovskites have proved to be exceptionally efficient absorber materials for photovoltaics. Besides improving the properties of the perovskite absorbers, device engineering and the optimization of interfaces will be equally important to further the advancement of this emerging solar cell technology. Herein, we report a successful modification of the interface between the NiO<sub>x</sub> hole transport layer and the perovskite absorber layer using 4-bromobenzylphosphonic acid based self-assembled monolayers leading to an improved photovoltaic performance. The modification of the NiO<sub>x</sub> layer is carried out by dip coating which allows sufficient time for the self-assembly. The change in the surface free energy and the non-polar nature of the resulting surface is corroborated by contact angle measurements. X-ray photoelectron spectroscopy confirms the presence of phosphor and bromine on the NiO<sub>x</sub> surface. Furthermore, the resultant solar cells reveal increased photovoltage. For typical devices without and with modification, the photovoltage improves from 0.978 V to 1.029 V. The champion V<sub>OC</sub> observed was 1.099 V. The increment in photovoltage leads to improved power conversion efficiencies for the modified cells. The maximum power point tracking measurements of the devices show stable power output of the solar cells.

## **Keywords**

triple cation perovskite, interface, self-assembled monolayer, phosphonic acid, photovoltaics

## **Introduction**

Lead halide perovskite solar cells have reached certified power conversion efficiencies (PCEs) greater than 23% in a conventional n-i-p architecture [1-3]. Similarly, also with perovskite solar cells based on a planar inverted p-i-n architecture efficiencies greater than 20% have imposingly been realized [4,5]. In addition, devices in inverted p-i-n architecture have piqued considerable interest as they offer the possibility to be processed at low temperature and also on flexible substrates [5-7]. The diminishing gap between the performance of both device architectures has been majorly possible due to optimizing the

inorganic hole transport layers (HTLs). In particular, nickel oxide ( $\text{NiO}_x$ ) films proved to be promising, as they allow facile processing, good stability and efficient hole extraction [8,9]. Furthermore, different doping procedures for  $\text{NiO}_x$  such as incorporation of copper, cesium or silver ions have led to improved device performance and are opening up pathways for further optimisations [10-12].

In recent practice, the  $\text{NiO}_x$  layers for the application in perovskite solar cells are deposited majorly via solution processes by using sol-gel methods or nanoparticle dispersions in water [10,13-19]. Moreover, atomic layer deposition, flame spray synthesis, pulsed laser deposition, sputtering and electrodeposition have been applied for the formation of  $\text{NiO}_x$  thin films [20-25].

In photovoltaics, interface engineering between charge transport layers and the absorber layer is an important approach in device optimization. One of the primary concepts utilized to achieve such engineering is the application of self-assembled monolayers (SAMs) [26-28]. The formation of a monolayer and the effective dipole of the applied molecules can be explored for designing the properties at the aforementioned interface. The SAMs allow the manipulation of the work function and the wettability of the metal oxide films, and they can also passivate the interface [29,30]. For example, Wang et al. reported on the effects of para-substituted benzoic acid SAMs on the  $\text{NiO}_x$  and perovskite interface. They highlighted an improved open circuit voltage ( $V_{OC}$ ) due to the introduction of bromobenzoic acid (dipole moment of 2.1 D) as a monolayer on the  $\text{NiO}_x$  film [31].

In this work, we discuss the influence of the modification of the  $\text{NiO}_x$  HTL with 4-bromobenzylphosphonic acid (Br-BPA) on lead halide perovskite solar cells. We chose phosphonic acids as the interface modifier as they have so far been barely investigated in perovskite solar cells even though they have been thoroughly studied in organic field effect transistors as well as organic photovoltaics and possess beneficial properties for surface modification of metal oxides [32]. In a study on the modification of zinc oxide ( $\text{ZnO}$ ) with benzylphosphonic acids (BPA), Lange et al. reported that BPA SAMs have a preferential tridentate binding on a  $\text{ZnO}$  surface. A tridentate binding suggests a stronger chemisorption of the SAM molecules on the metal oxide surface in comparison to the mono- and bi-dentate binding [32-35]. As absorber layer for the solar cells prepared in p-i-n architecture, a triple cation based perovskite with the composition  $\text{Cs}_{0.1}(\text{FA}_{0.83}\text{MA}_{0.17})_{0.9}\text{Pb}(\text{I}_{0.83}\text{Br}_{0.17})_3$ , introduced by Saliba et al. [36], was selected.

## Experimental

### Sample and solar cell preparation

All chemicals and solvents were used as purchased without any further purification. Nickel(II) nitrate hexahydrate and sodium hydroxide was purchased from Fluka and VWR, respectively. Lead iodide, lead bromide, formamidinium iodide and PC<sub>60</sub>BM were purchased from TCI, Alfa Aesar, GreatCell Solar and Solenne, respectively. The other chemicals used in this study, including the phosphonic acid molecule, and all the solvents were purchased from Merck (Sigma Aldrich).

### Material synthesis

*Synthesis and characterization of nickel oxide nanoparticles:* The synthesis of the NiO<sub>x</sub> nanoparticles was performed according to previous reports [15,37-39]. In brief, nickel (II) nitrate hexahydrate (NiNO<sub>3</sub> · 6 H<sub>2</sub>O) (0.05 mol) was dispersed in 10 mL deionized water and stirred for 5 minutes. Afterwards sodium hydroxide (NaOH, 10 mmol/mL) was added dropwise to adjust a pH of 10, which results in a colour change from dark to light green. The colloidal precipitate was then washed with deionized water to remove side products. The light green residue was further dried at 80 °C for 6 h followed by calcination at 270 °C for 2 h. This resulted in non-stoichiometric black nickel (II) oxide nanoparticles. The X-ray diffraction (XRD) pattern of the NiO<sub>x</sub> nanoparticles is very similar to as reported in Ref. [15] and reveals reflections at 37.2°, 43.2°, 62.7°, 75.4° and 79.3° 2θ, which correspond to the (111), (200), (220), (311), and (222) lattice planes in a cubic crystal structure. An estimation of the primary crystallite size based on the peak broadening via Scherrer formula led to a value of approx. 8 nm. For the preparation of the NiO<sub>x</sub> ink, 20 mg/mL of the NiO<sub>x</sub> nanoparticles were dispersed in deionized water. The ink was put in an ultrasonic bath for 2 h and then filtered using a 0.45 μm PVDF syringe filter.

### Solar cell preparation

*Back electrode:* Pre-patterned glass/ITO substrates (15 × 15 × 1.1 mm<sup>3</sup>) (15 Ω cm<sup>-2</sup>) from Luminescence Technology Corp. (Lumtec) were carefully wiped using acetone before putting them into an isopropanol bath. The bath was further subjected to an ultrasonic bath for 10 minutes. The substrates were then dried using in an N<sub>2</sub> stream. Just before spin coating the NiO<sub>x</sub> nanoparticle ink, the substrates were plasma etched using oxygen plasma for 3 minutes.



*Preparation of the NiO<sub>x</sub> films:* The NiO<sub>x</sub> nanoparticle ink was spin coated onto the glass/ITO substrates at a speed of 1000 rpm. Before the determination of the layer thickness and solar cell preparation, the films were allowed to dry in ambient conditions for 3 days. The as-prepared films revealed an average thickness distribution of ~25 nm.

*Surface modification of the NiO<sub>x</sub> films with Br-BPA:* A 5 mmol/mL solution of Br-BPA was prepared in acetonitrile and was filtered using a 0.45 μm PVDF syringe filter. The application of the Br-BPA molecule was done by dip coating. In the dip coating method, the glass/ITO/NiO<sub>x</sub> substrates were dipped in the phosphonic acid solution for 1 min to allow adsorption. These substrates were then cleaned by dipping them in fresh acetonitrile solvent to allow removal of non-adsorbed phosphonic acid molecules from the modified surface. The substrates were then dried in an N<sub>2</sub> stream. The deposition was carried out in ambient conditions.

*Preparation of the perovskite absorber layers:* The cesium, formamidinium, and methylammonium based triple cation lead halide perovskite absorber layer was adapted from Saliba et al. [36]. The final composition chosen was Cs<sub>0.1</sub>(FA<sub>0.83</sub>MA<sub>0.17</sub>)<sub>0.9</sub>Pb(I<sub>0.83</sub>Br<sub>0.17</sub>)<sub>3</sub>. The precursor solution consisted of 1 mmol/mL formamidinium iodide (FAI), 1.1 mmol/mL PbI<sub>2</sub>, 0.2 mmol/mL methylammonium bromide (MABr), and 0.2 mmol/mL PbBr<sub>2</sub> in a mixed dimethyl formamide (DMF)/dimethyl sulfoxide (DMSO) solvent with a 4:1 volume ratio. To this solution, 1.5 mmol/mL CsI in DMSO, was added to obtain a 10% Cs content. The final precursor solution was stirred overnight in inert conditions to allow sufficient reaction time. The solution was then filtered using a 0.45 μm PTFE syringe filter prior to spin coating. The perovskite absorber layer was spin coated on the non-modified and modified glass/ITO/NiO<sub>x</sub> substrates in a two-step spin coating process with 1000/6000 rpm for 10/20 s. In the last 5 s of spinning, chlorobenzene was dripped onto the substrate as an antisolvent. The substrates were annealed at 100 °C for 1 h. The thickness of the perovskite absorber layers was monitored using a Stylus profilometer and was found to be approximately 485 nm.

*PC<sub>60</sub>BM electron transport layer and top electrode:* A phenyl-C<sub>61</sub>-butyric acid methyl ester (PC<sub>60</sub>BM) solution in chlorobenzene having a concentration of 20 mg/mL was prepared. The solution was stirred overnight and filtered using a 0.45 μm PTFE syringe filter prior to spin coating at 4000 rpm for 20 seconds. In a last step of the solar cell preparation, a 120 nm thick

silver layer was deposited by thermal evaporation on top of the PC<sub>60</sub>BM layer at an evaporation rate of 1-2 Å s<sup>-1</sup> using a shadow mask (0.09 cm<sup>2</sup>).

### **Characterization techniques**

XRD was performed on a PANalytical Empyrean system using Cu K<sub>α</sub> radiation. Ultraviolet-visible (UV-Vis) spectroscopy measurements were done using the UV/VIS Spectrometer – Lambda 35 by Perkin Elmer. The layer thicknesses were measured by surface profilometry using a DektakXT device by Bruker and the surface morphology of the perovskite films was characterized by scanning electron microscopy (SEM) images acquired on a Zeiss-Supra 40 scanning electron microscope with an in-lens detector and 5 kV acceleration voltage.

Contact angle measurements of the NiO<sub>x</sub> films before and after the modification with Br-BPA were carried out on a Krüss DSA100 system using water and ethylene glycol as liquids. The surface free energy calculations were performed with the Owens-Wendt-Rabel & Kaelble method [40] using the Krüss Advance software.

X-ray photoelectron spectroscopy (XPS) measurements of the NiO<sub>x</sub> and NiO<sub>x</sub>/Br-BPA SAM films were recorded using a multiprobe surface analysis system (Omicron Nanotechnology) equipped with a DAR 400 X-ray source (Al K<sub>α1</sub> radiation, 1486.7 eV), an XM 500 quartz crystal monochromator (energy width: 0.15 eV), and an EA 125 hemispherical electron energy analyzer based on a 5-channel pulse counting channeltron.

The current density – voltage (JV) curves and maximum power point (MPP) tracking measurements of the solar cells were performed using Keithley 2400 source meter and a LabView-based software inside a glove box (nitrogen atmosphere). For the JV curves, the scan rates were adjusted to 100 mVs<sup>-1</sup> in the forward (fwd) direction (-0.02 V to 1.2 V) and backward (bwd) direction (1.2 V to -0.02 V) for both light and dark measurements. The illumination area was defined using a shadow mask (0.0702 cm<sup>2</sup>) and the light was provided by a Dedolight DLH500 lamp calibrated to an intensity of 100 mWcm<sup>-2</sup> using a pyranometer from Kipp & Zonen. The External Quantum Efficiency (EQE) spectra were acquired using a MuLTImode 4 monochromator (Amko) equipped with a 75 W xenon lamp (LPS 210-U, Amko), a lock-in amplifier (Stanford Research Systems, Model SR830), and a Keithley 2400 source meter. The monochromatic light was chopped at a frequency of 30 Hz and the measurement setup was spectrally calibrated with a silicon photodiode (Newport Corporation, 818-UV/DB).

## Results and discussion

The modification of the NiO<sub>x</sub> thin films with Br-BPA was performed by dipping the films into an acetonitrile solution containing the Br-BPA molecules followed by washing the substrates in pure acetonitrile. A detailed description of the procedure can be found in the experimental part. The chemical structure of Br-BPA and a schematic illustration of the modification together with the used solar cell setup to investigate the influence of the modification on the photovoltaic performance are shown in **Figure 19**. During the dipping process, the phosphonic acid groups bind to the NiO<sub>x</sub> surface whereby the Br-BPA molecules very likely form a SAM. Thereby, on the one hand the surface will become more non-polar due to the Br functionality which might influence wetting of the perovskite precursor solution and the crystallisation properties of the perovskite films. On the other hand, the Br-BPA molecule has a dipole moment of 2.3 D [33], which can facilitate charge extraction and also reduce the valence band energy of the NiO<sub>x</sub> film, similar to as it was experimentally and theoretically shown for the modification of ZnO surfaces [30,32,34,35].

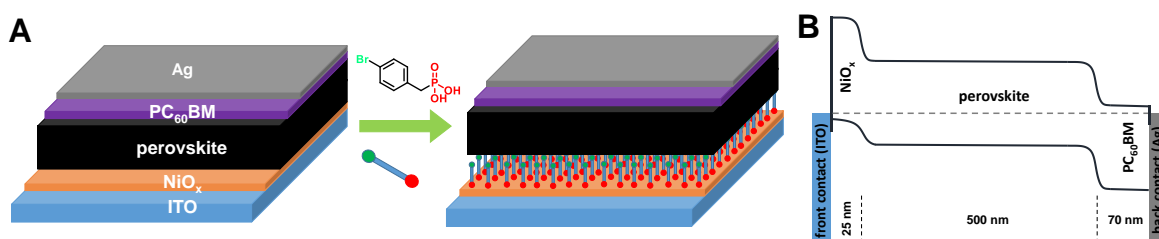


**Figure 19:** (A) Schematic illustration of the modification of the NiO<sub>x</sub>-layer with 4-bromobenzylphosphonic acid and the device architectures of the investigated solar cells (glass/ITO/NiO<sub>x</sub>/perovskite/PC<sub>60</sub>BM/Ag) without and with Br-BPA modification, (B) schematic energy band diagram for the device configuration ITO/NiO<sub>x</sub>/perovskite/PC<sub>60</sub>BM/Ag; the scheme is not drawn to scale and the Fermi level is taken as the reference energy level.

As a first step, the presence of a Br-BPA SAM and the modification of the surface properties of the NiO<sub>x</sub> films were confirmed by contact angle measurements. Figure 2 shows the changes in the shape of water and ethylene glycol drops on the non-modified and modified NiO<sub>x</sub> films. The corresponding values of the contact angles are summarized in **Table 7**. It is apparent that the contact angle of water is significantly increased from 21.9° to 93.1° due to the Br-BPA modification indicating a rise in the hydrophobicity of the surface. The high contact angle of water after the modification also indicates a dense coverage of the NiO<sub>x</sub>

surface with the Br-BPA molecules. To calculate the surface free energy of the films, additional contact angle measurements with ethylene glycol were performed showing an increase from 15.8° to 24.3° due to the introduction of the Br-BPA SAM. The surface free energy of the NiO<sub>x</sub> film was calculated to be 88.4 mN m<sup>-1</sup> with a very low disperse part of 0.47 mN m<sup>-1</sup> and a polar part of 88.0 mN m<sup>-1</sup>. After the modification, a value of 126.5 mN m<sup>-1</sup> was obtained and the polarity changed completely to a disperse part of 120.9 mN m<sup>-1</sup> and a polar part of 5.6 mN m<sup>-1</sup>. This indicates a successful incorporation of the Br-BPA molecules on the surface of the NiO<sub>x</sub> layers and the corresponding change in surface properties.

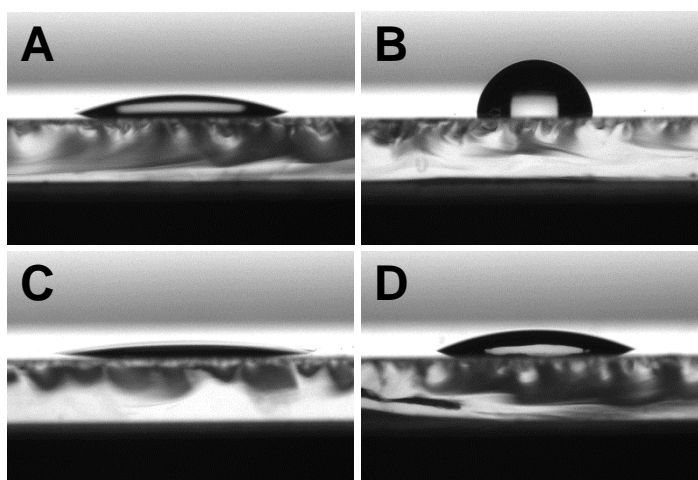


**Figure 20:** Images showing the typical drop shapes of (A) water on a NiO<sub>x</sub> film, (B) water on NiO<sub>x</sub> / Br-BPA film, (C) ethylene glycol on a NiO<sub>x</sub> film and (D) ethylene glycol on NiO<sub>x</sub> / Br-BPA film.

**Table 7:** Results of the contact angle measurements of the non-modified and modified NiO<sub>x</sub> layers.

| <i>sample</i>                   | <i>contact angle - water (°)</i> | <i>contact angle - ethylene glycol (°)</i> | <i>surface free energy (mN m<sup>-1</sup>)</i> | <i>disperse part (mN m<sup>-1</sup>)</i> | <i>polar part (mN m<sup>-1</sup>)</i> |
|---------------------------------|----------------------------------|--|--|--|---------------------------------------|
| <b>NiO<sub>x</sub></b>          | 21.9 ± 0.3                       | 15.8 ± 2.1                                 | 88.4 ± 0.4                                     | 0.47 ± 0.03                              | 88.0 ± 0.4                            |
| <b>NiO<sub>x</sub> / Br-BPA</b> | 93.1 ± 0.3                       | 24.3 ± 0.4                                 | 126.5 ± 2.0                                    | 120.9 ± 1.6                              | 5.6 ± 0.4                             |

In order to confirm the presence of the phosphonic acid molecules at the surface of the NiO<sub>x</sub> film, we performed XPS measurements. The survey XPS spectra of the non-modified and modified NiO<sub>x</sub> films are shown in **Figure 21A** and **B**. The high peak intensities of indium (In) and tin (Sn) are indicating that the NiO<sub>x</sub> layer is at least in some parts only a few nanometres thin. Due to the high surface sensitivity of this technique, we detect the P 2p doublet of the phosphonic acid at 132.5 eV and the Br 3p doublet at 183 and 190 eV in the modified sample, while these peaks are absent in the reference sample (**Figure 21C**). The signal at 284 eV can be assigned to the C 1s peak and is increased with the presence of the SAM molecules.

The corresponding high-resolution XPS core-level spectra are given in the **Figure 21D** and **E**. Peak fits were performed by using a convolution of a Gaussian and a Lorentzian profile.

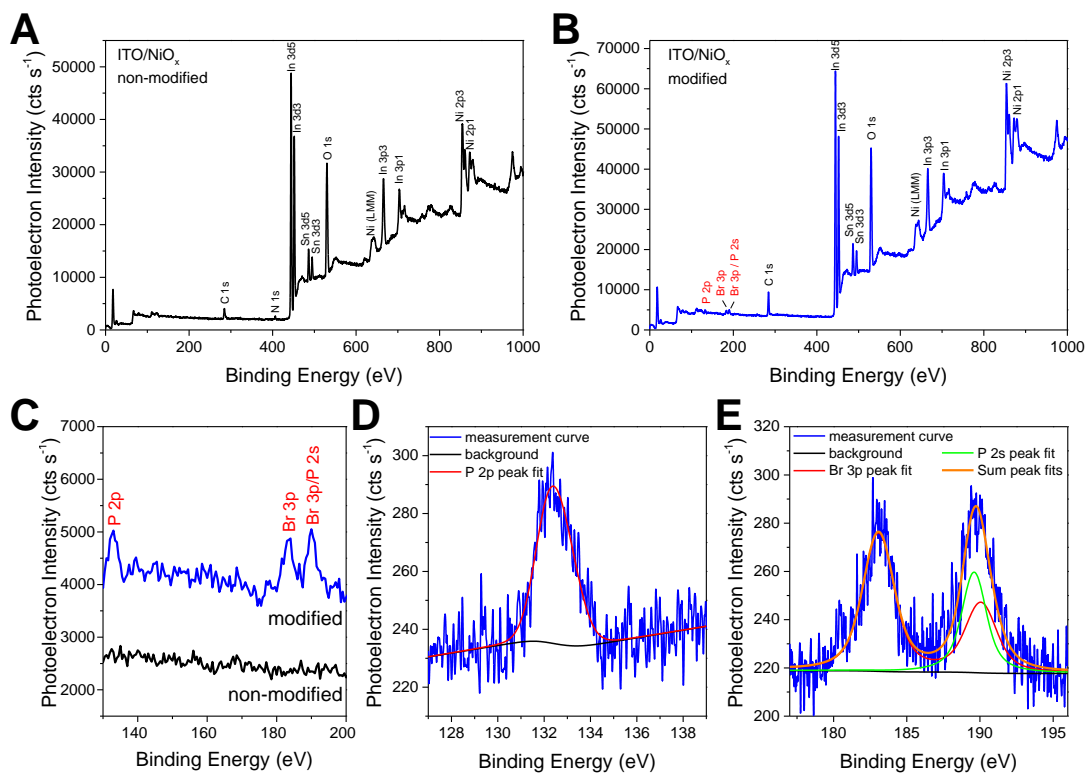


**Figure 21:** XPS survey spectra of a non-modified (A) and modified NiO<sub>x</sub> film (B); details of the region of the relevant P- and Br-peaks (C) confirming the presence of phosphor and bromine at the surface of the modified NiO<sub>x</sub> film; high resolution XPS spectra and peak deconvolution of the P 2p (D) and the Br 3p peak with additional signal of P 2s (E) in the modified sample.

A quantification of the detectable chemical elements was performed by peak deconvolution of all detailed spectra. In order to get additional information about the surface layers, XPS spectra were measured under three detection angles of 0°, 35° and 50° relative to the surface normal. As expected, we find increasing signals of surface layers with increasing detection angles. The attenuation of the photoelectron signal ( $I/I_0$ ) by inelastic scattering in a layer of the thickness ( $d$ ) can be calculated by using the equation [41]:

$$\frac{I}{I_0} = e^{-\frac{d}{\lambda \cdot \cos \theta}} \quad (11)$$

The inelastic mean free path of the photoelectrons ( $\lambda$ ) is dependent on the kinetic energy of the photoelectrons and the layer material. The values of  $\lambda$  were determined from the Tanuma, Powell, and Penn TPP2M formula [42] and the software QUASES written by Sven Tougaard.  $\theta$  is the detection angle relative to the surface normal. For a given layer system, in our case ITO/NiO<sub>x</sub>/BrBPA, the expected total photoelectron intensity of each element can be calculated by the signal sum over all atomic layers including the atomic density of the element in the layer. The layer model was optimized for the best matching of the calculated contribution of each element with the element quantification of the measured spectra at all detection angles. We found a good agreement between the measured and calculated data by assumption of a NiO<sub>x</sub> nanoparticle layer with an average thickness of around 5 nm on the ITO and a Br-BPA SAM-layer with a density of 4 molecules per nm<sup>2</sup>. This matches well with previously reported surface coverage densities of phosphonic acids molecules on metal oxides [35,43]. Previous studies on NiO<sub>x</sub> HTLs for perovskite solar cells revealed that NiO<sub>x</sub> film thicknesses of around 25 nm are beneficial for the solar cell performance. Therefore, we adjusted the thickness of the NiO<sub>x</sub> films used in the solar cells in the further cause of the study by optimizing the spin coating parameters [10,11,15,31].

In the next step, we investigated the effects of the Br-BPA SAM on the properties of the perovskite thin film. **Figure 22A** shows the XRD pattern of the Cs<sub>0.1</sub>(MA<sub>0.17</sub>FA<sub>0.83</sub>)<sub>0.9</sub>Pb(I<sub>0.83</sub>Br<sub>0.17</sub>)<sub>3</sub> perovskite films prepared on non-modified and modified NiO<sub>x</sub> films. Both samples show the typical pattern of the cubic perovskite crystal structure with characteristic peaks at 14.1° and 28.4° for the (110) and (220) lattice planes along with peaks at 20.0°, 24.5°, 31.8°, 40.6° and 43.2° 2 $\theta$ , which matches well with literature data [36,44,45]. Furthermore, the intensity ratios of the peaks in the non-modified

sample are very similar to the ones in the modified sample indicating no change in orientation of the perovskite crystals relative to the substrate. The peaks at  $35.0^\circ$  and  $50.2^\circ$   $2\theta$  stem from the ITO substrate. The minor peak at  $12.7^\circ$   $2\theta$  indicates small amounts of  $\text{PbI}_2$  in the films. A minor excess of  $\text{PbI}_2$  was reported to improve the properties of the grain boundaries and to suppress non-radiative charge carrier recombination in the perovskite films [46,47].

The absorption spectra of the perovskite films suggest a similar absorption onset ( $\sim 770$  nm) in agreement with a bandgap of  $\sim 1.61$  eV [36,45]. The slight differences in the intensity of the absorption spectrum stem from minor changes in the film thickness. The surface profile measurements revealed film thicknesses of the perovskite layers between 485 and 510 nm independent of the surface modification.

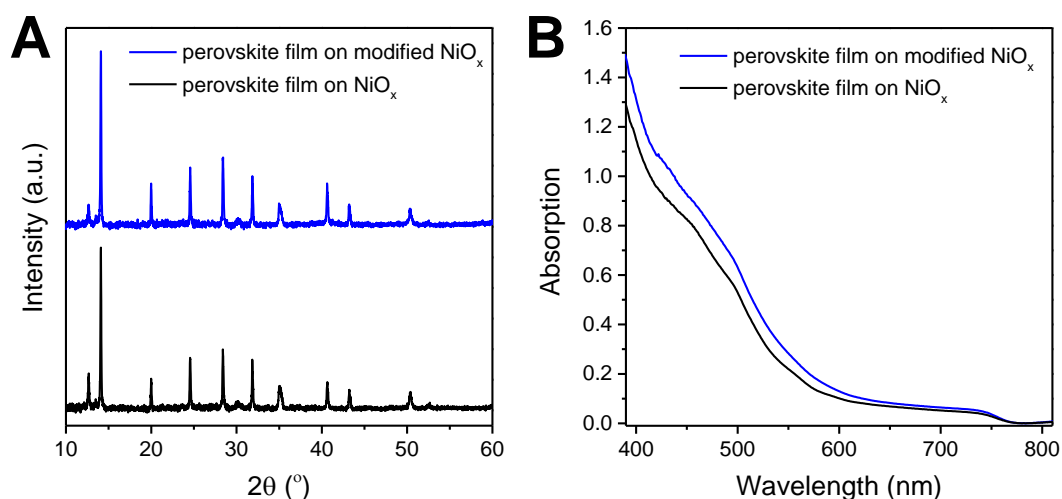


**Figure 22:** (A) XRD patterns and (B) UV-Vis absorption spectra of perovskite thin films prepared on glass/ITO/ $\text{NiO}_x$  substrates without and with Br-BPA modification.

Furthermore, the surface morphology of the perovskite films prepared on glass/ITO/ $\text{NiO}_x$  substrates without and with Br-BPA modification was investigated by scanning electron microscopy. The top view images depicted in **Figure 23** reveal homogeneous perovskite films and their complete coverage of the  $\text{NiO}_x$  films. The grain sizes range from 125 - 135 nm for the smaller sized grains to approximately 475 - 510 nm for the larger ones and no significant changes based on the surface modification are noticed.

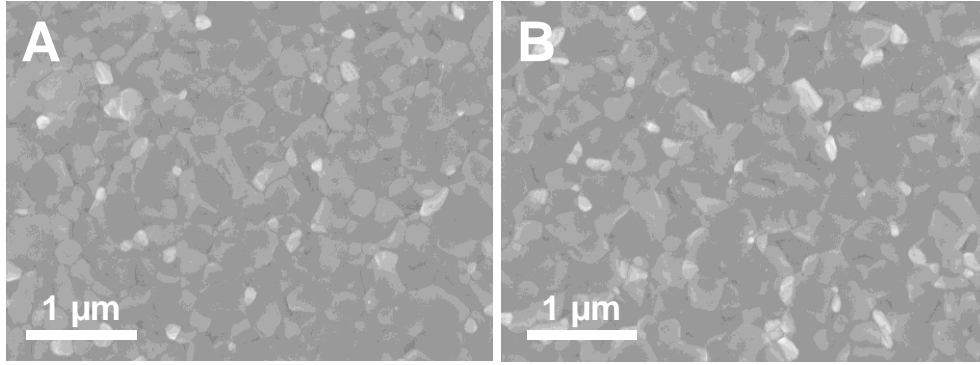


**Figure 23:** Top view SEM images of perovskite thin films prepared on a non- modified (A) and modified (B) NiO<sub>x</sub> layer.

To evaluate the influences of the modification on the photovoltaic performance, solar cells with the device architecture glass/ITO/NiO<sub>x</sub>/perovskite/PC<sub>60</sub>BM/Ag (cf. scheme and energy band diagram in **Figure 19A**) were prepared. A schematic energy band diagram based on the values published in literature [48-51] is shown in **Figure 19B**. The Fermi level has been chosen as the reference energy level instead of the vacuum level since this is more suited to describe non-ideal systems such as the herein discussed devices [51]. The JV curves of typical solar cells without and with Br-BPA modification measured in fwd and bwd direction are presented in **Figure 24A**. The corresponding characteristic parameters are summarized in **Table 8**. The most obvious change in the photovoltaic properties is the enhanced photovoltage in the devices with the Br-BPA modification. In these solar cells, the V<sub>OC</sub> is increased from 0.978 V to 1.019-1.029 V. This increase in V<sub>OC</sub> resonates with previous reports investigating benzoic acids for the NiO<sub>x</sub> modification and originates most presumably from the lowering of the valence band energy of the NiO<sub>x</sub> films by the surface modification [31]. Moreover, there is a slight increase in short circuit current density (J<sub>SC</sub>) detectable for the solar cells with Br-BPA modification which can be attributed to the dipole moment of the molecule.

The prepared solar cells exhibit an only minor hysteresis, as can be seen in the JV curves in **Figure 24A**. The hysteresis index (HI) of the solar cells was calculated according to

$$HI = \frac{\int_{SC}^{OC} (J_{bwd}(V) - J_{fwd}(V)) dv}{\int_{SC}^{OC} J_{bwd}(V) dv} \quad (12)$$



whereby,  $J_{\text{bwd}}$  (V) indicates the area of the JV curve for the backward scan and  $J_{\text{fwd}}$  (V) indicates the area for the forward scan in the region between short circuit (SC) and open circuit (OC) conditions. This equation was adapted from Ref. [52] which considers the integrated power output of the solar cells in fwd (SC to OC) and bwd (OC to SC) scan directions. Based on Nemnes et al. [53-55] this method is useful for the determination of the HI for normal and inverted hysteresis in non-crossing JV curves. If the HI approaches 0, the solar cell would have negligible hysteresis. For the typical solar cells shown, we calculated an HI of -0.0562 for the device with the non-modified  $\text{NiO}_x$  layer and the HI is slightly reduced to -0.0131 for the solar cell with the modified  $\text{NiO}_x$  HTL.

The MPP tracking measurements (**Figure 24B**) reveal a constant power output of the solar cells. While the voltage at MPP ( $V_{\text{MPP}}$ ) is slightly decreasing at the beginning of the measurement, the current density at MPP ( $J_{\text{MPP}}$ ) improves slightly leading to a constant power output and a PCE of 11.4% and 12.2% for the non-modified and the modified device after 10 minutes of continuous illumination, respectively.

The EQE spectra (**Figure 24C**) for the representative devices show a typical shape of perovskite solar cells with an onset at 770 nm and a characteristic plateau at wavelengths below 750 nm. Moreover, the spectra remain almost unchanged upon the modification of the  $\text{NiO}_x$  HTL. This is expected, as the  $J_{\text{SC}}$  for the representative devices are rather similar. The integrated  $J_{\text{SC}}$  calculated from the EQE spectrum sums up to 18.2 and 18.4  $\text{mA}/\text{cm}^2$  and is within a few percent deviation to the values extracted from the JV curves.

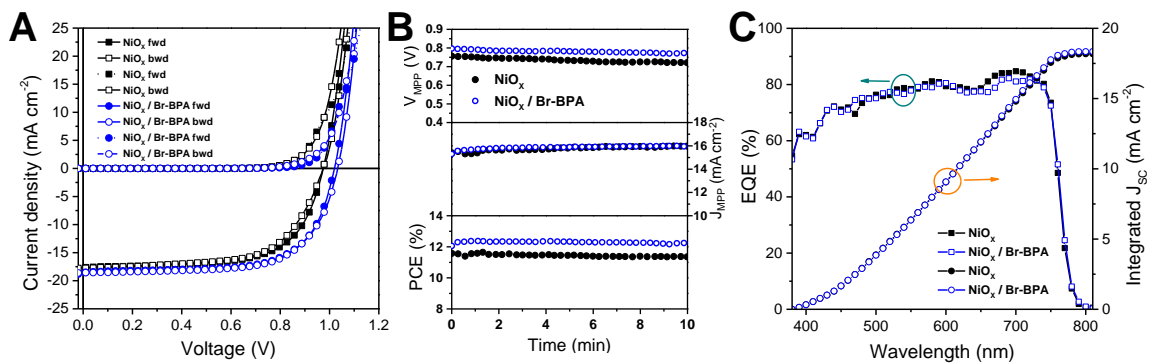


**Figure 24:** (A) JV curves (dark and illuminated) measured in forward and backward direction, (B) maximum power point tracking measurements and (C) EQE spectra of typical perovskite solar cells prepared with non-modified and modified  $\text{NiO}_x$  hole transport layers.

**Table 8:** Characteristic parameters of typical perovskite solar cells prepared with non-modified and modified NiO<sub>x</sub> hole transport layers.

|  | <i>Scan</i><br><i>Direction</i> | <i>V<sub>OC</sub></i><br>(V) | <i>J<sub>SC</sub></i><br>(mA cm <sup>-2</sup> ) | <i>FF</i><br>(%) | <i>PCE</i><br>(%) | <i>R<sub>S</sub></i><br>(Ωcm <sup>2</sup> ) | <i>R<sub>SH</sub></i><br>(Ωcm <sup>2</sup> ) | <i>HI</i> |
|--|---------------------------------|------------------------------|---|------------------|-------------------|---|--|-----------|
| <b>NiO<sub>x</sub></b>                   | bwd                             | 0.978                        | 17.77   | 62.69            | 10.82             | 8.13  | 645  | -0.0562   |
|  | fwd                             | 0.978                        | 17.68   | 65.04            | 11.16             | 5.14  | 970  |           |
| <b>NiO<sub>x</sub> /<br/>Br-<br/>BPA</b> | bwd                             | 1.029                        | 18.58   | 67.18            | 12.73             | 4.68  | 1240   | -0.0131   |
|  | fwd                             | 1.019                        | 18.57   | 66.94            | 12.54             | 4.29  | 751  |           |

The statistical data of the 20 best solar cells (non-modified and modified separately) prepared within this study are shown using box plots in **Figure 25**. These data support the discussion above. **Figure 25** reveals that the V<sub>OC</sub> of the solar cells is enhanced in both scan directions; also the average J<sub>SC</sub> is slightly improved. Regarding the fill factor (FF), there is no major change observed. This results in an average increase in PCE from 11.4±0.7% (11.1±1.1%) to 12.1±0.3% (12.6±0.3%) for the Br-BPA modification based solar cells in fwd (bwd) scan directions, respectively.

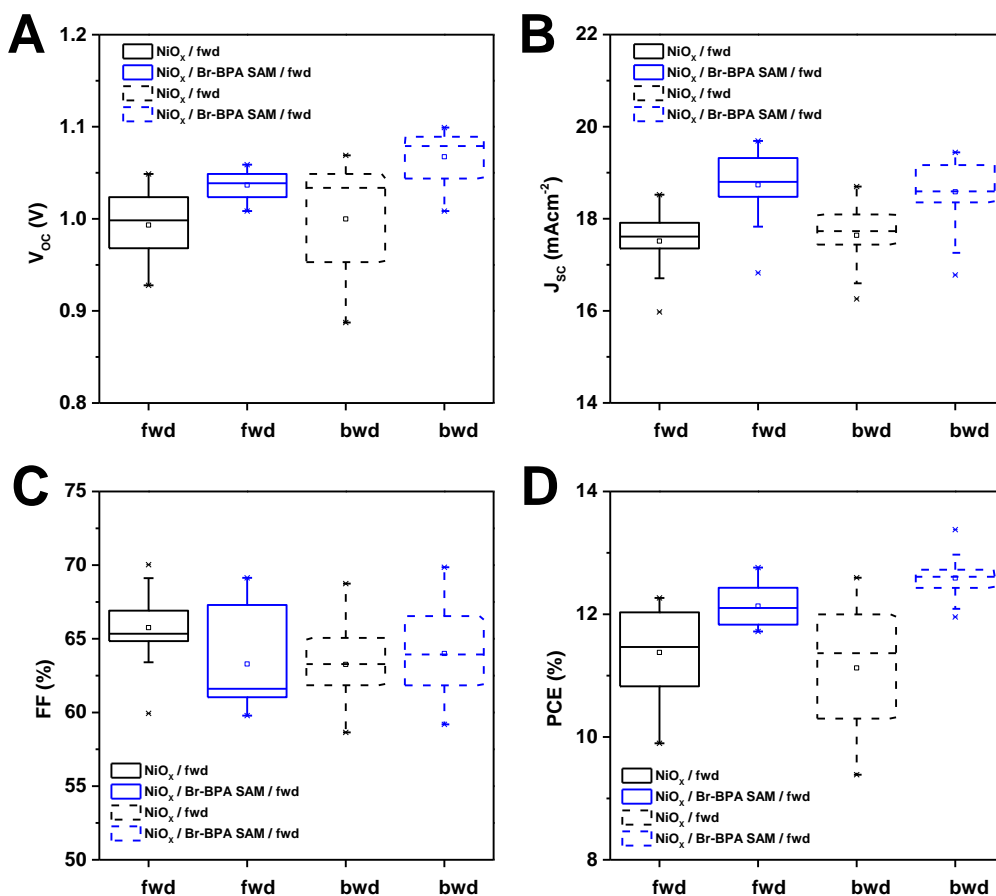


**Figure 25:** Box plots showing statistics of the characteristic parameters **(A)**  $V_{OC}$ , **(B)**  $J_{SC}$ , **(C)** FF and **(D)** PCE of the best 20 devices prepared each with non-modified and modified  $NiO_x$  hole transport layers.

With the Br-BPA modification, we observed  $V_{OC}$ s of up to 1.1 V in this study. The JV curves of such a solar cell are shown in **Figure 26**. In bwd scan direction a  $V_{OC}$  of 1.099 V was obtained corroborating the potential of this modification strategy. The EQE spectrum reveals values up to 87.9% and the derived integrated  $J_{SC}$  ( $19.55 \text{ mA cm}^{-2}$ ) shows consistency with the  $J_{SC}$  observed in the JV curve. The PCE of this solar cell was at 12.7%.

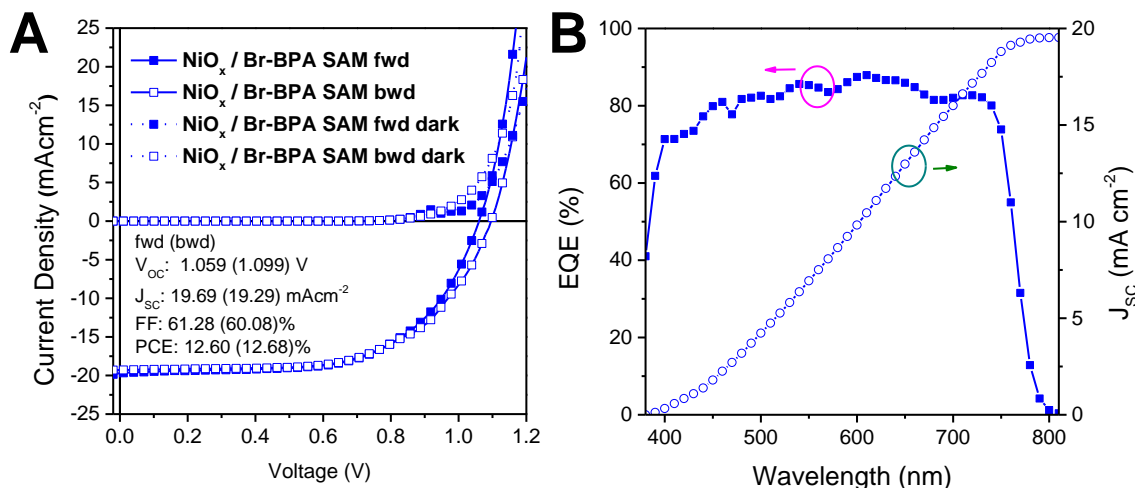


**Figure 26:** JV curves (A) and EQE spectrum (B) of one of the devices with Br-BPA modification showing the highest  $V_{OC}$  prepared within this study.

## Conclusion

In summary, we successfully functionalized solution processed NiO<sub>x</sub> HTLs by a dip coating procedure using a Br-BPA solution in acetonitrile. This is substantiated by the markedly increased contact angle of water, the surface free energies and the detection of P 2p and Br 3p peaks in the modified sample by XPS measurements. We did not observe any notable change in the optical properties and surface morphology of the perovskite layers. However, the JV curves reflect improved photovoltaic performance, particularly an increased  $V_{OC}$ . A typical device shows an improved PCE from 11.2% (10.8%) to 12.5% (12.7%) due to an improved  $V_{OC}$  from 0.978 V (0.978 V) to 1.019 V (1.029 V) in fwd (bwd) scan directions, respectively. We assume that the improvement in the  $V_{OC}$  is largely due to the realignment of the energy levels based on the dipole moment of the Br-BPA SAM molecules. With devices having Br-BPA modifications,  $V_{OC}$ s of up to 1.099 V could be obtained. Furthermore, MPP tracking measurements revealed a steady state PCE of 11.35% and 12.22% for typical devices without and with Br-BPA modified NiO<sub>x</sub> films.

## **Acknowledgement**

This work was carried out within the project “flex!PV\_2.0” (FFG No. 853603) funded by the Austrian Climate and Energy Fund within the program Energy Emission Austria. Birgit Ehmman is gratefully acknowledged for experimental support.

## References

1. N.J. Jeon, H. Na, E.H. Jung, T.-Y. Yang, Y.G. Lee, G. Kim, H.-W. Shin, S.I. Seok, J. Lee, J. Seo, *Nature Energy* **3**, 682-689 (2018)
2. <https://www.nrel.gov/pv/assets/pdfs/best-research-cell-efficiencies.pdf>
3. M.A. Green, Y. Hishikawa, E.D. Dunlop, D.H. Levi, J.H.-Ebinger, M. Yoshita, A.W.Y. H.-Baillie, *Prog Photovolt Res Appl.* **27**, 3-12 (2019)
4. W. Chen, Y. Wu, J. Fan, A.B. Djurišić, F. Liu, H.W. Tam, A. Ng, C. Surya, W.K. Chan, D. Wang, Z.-B. He, *Adv. Energy Mater.* **8**, 1703519 (2018)
5. S. Ye, H. Rao, Z. Zhao, L. Zhang, H. Bao, W. Sun, Y. Li, F. Gu, J. Wang, Z. Liu, Z. Bian, C. Huang, *J. Am. Chem. Soc.* **139**, 7504-7512 (2017)
6. L. Hu, K. Sun, M. Wang, B. Yang, J. Fu, Z. Xiong, X. Li, X. Tang, Z. Zang, S. Zhang, L. Sun, M. Li, *ACS Appl. Mater. Interfaces* **9**, 43902-43909 (2017)
7. G. Adam, M. Kaltenbrunner, E.D. Glowacki, D.H. Apaydin, M.S. White, H. Heilbrunner, S. Tombe, P. Stadler, B. Ernecker, C.W. Klampfl, N.S. Sariciftci, M.C. Scharber, *Solar Energy Materials & Solar cells* **157**, 318-325 (2016)
8. P.-K. Kung, M.-H. Li, P.-Y. Lin, Y.-H. Chiang, C.-R. Chan, T.-F. Guo, P. Chen, *Adv. Mater. Interfaces*, **5**, 1800882 (2018)
9. M.D. Irwin, D.B. Buchholz, A.W. Hains, R.P.H. Chang, T.J. Mark, *Proc. Natl. Acad. Sci.* **105**, 2783-2787 (2008)
10. W. Chen, F.-Z. Liu, X.-Y. Feng, A. B. Djurišić, W.K. Chan, Z.-B. He, *Adv. Energy Mater.* **7**, 1700722 (2017)
11. H.-S. Kim, J.-Y. Seo, H. Xie, M. L.-Cantu, S.M. Zakeeruddin, M. Grätzel, A. Hagfeldt, *ACS Omega* **2**, 9074-9079 (2017)
12. J. Zheng, L. Hu, J. S. Yun, M. Zhang, C. F. J. Lau, J. Bing, X. Deng, Q. Ma, Y. Cho, W. Fu, C. Chen, M. A. Green, S. Huang, A. W. Y. H.-Baillie, *ACS Appl. Energy Mater.* **1**, 561-570 (2018)
13. J.H. Kim, P.-W. Liang, S.T. Williams, N. Cho, C.-C. Chueh, M.S. Glaz, D. S. Ginger, A.K.-Y. Jen, *Adv. Mater.* **27**, 695-701 (2015)
14. Z. Liu, A. Zhu, F. Cai, L. Tao, Y. Zhou, Z. Zhao, Q. Chen, Y.-B. Cheng, H. Zhou, *J. Mater. Chem. A* **5**, 6597-6605 (2017)
15. S. Weber, T. Rath, J. Mangalam, B. Kunert, A.M. Coclite, M. Bauch, T. Dimopoulos, G. Trimmel, *J. Mater. Sci: Mater. Electron.* **29**, 1847-1855 (2018)

16. X. Yin, Z. Yao, Q. Luo, X. Dai, Y. Zhou, Y. Zhang, Y. Zhou, S. Luo, J. Li, N. Wang, H. Lin, *ACS Appl. Mater. Interfaces* **9**, 2439-2448 (2017)
17. S.S. Mali, H. Kim, S.E. Shim, C.K. Hong, *Nanoscale* **8**, 19189-19194 (2016)
18. Z. Zhu, Y. Bai, T. Zhang, Z. Liu, X. Long, Z. Wei, Z. Wang, L. Zhang, J. Wang, F. Yan, S. Yang, *Angew. Chem. Int. Ed.* **53**, 12571-12575 (2014)
19. J.W. Jung, C.-C. Chueh, A.K.-Y. Jen, *Adv. Mater.* **27**, 7874-7880 (2015)
20. J.H. Park, J. Seo, S. Park, S.S. Shin, Y.C. Kim, N.J. Jeon, H.-W. Shin, T.K. Ahn, J.H. Noh, S.C. Yoon, C.S. Hwang, S.I. Seok, *Adv. Mater.* **27**, 4013-4019 (2015)
21. K.-C. Wang, P.-S. Shen, M.-H. Li, S. Chen, M.-W. Lin, P. Chen, T.-F. Guo, *ACS Appl. Mater. Interfaces* **6**, 11851-11858 (2014)
22. A.S. Subbiah, A. Halder, S. Ghosh, N. Mahuli, G. Hodes, S.K. Sarkar, *J. Phys. Chem. Lett.* **5**, 1748-1753 (2014)
23. S. Seo, I.J. Park, M. Kim, S. Lee, C. Bae, H.S. Jung, N.-G. Park, J.N. Kim, H. Shin, *Nanoscale* **8**, 11403-11412 (2016)
24. Y. Hou, W. Chen, D. Baran, T. Stubhan, N.A. Luechinger, B. Hartmeier, M. Richter, J. Min, S. Chen, C.O.R. Quiroz, K. Forberich, Z.-G. Zhang, Y. Li, B. Winter, P. Schweizer, E. Spiecker, C.J. Brabec, *Adv. Mater.* **28**, 5112-5120 (2016)
25. S. Seo, S. Jeong, H. Park, H. Shin, N.-G. Park, *Chem. Commun.* **55**, 2403-2416 (2019)
26. A. Abrusci, S. D. Stranks, P. Docampo, H. L. Yip, A. K. Jen, H. J. Snaith, *Nano Lett.* **13**, 3124-3128 (2013)
27. L. Zuo, Z. Gu, T. Ye, W. Fu, G. Wu, H. Li, H. Chen, *J. Am. Chem. Soc.* **137**, 2674-2679 (2015)
28. L. Yang, G. Chen, Y. Sun, D. Han, S. Yang, M. Gao, P. Zou, H. Luan, X. Kong, J. Yang, *Electrochimica Acta* **164**, 38-47 (2015)
29. P. Zhao, B.J. Kim, H.S. Jung, *Materials Today Energy* **7**, 267-286 (2018)
30. R. Azmi, W.T. Hadmojo, S. Sinaga, C.-L. Lee, S. C. Yoon, I.H. Jung, S.-Y. Jang, *Adv. Energy Mater.* **8**, 1701683 (2018)
31. Q. Wang, C.-C. Chueh, T. Zhao, J. Cheng, M. Eslamian, W.C.H. Choy, A.K.-Y. Jen, *ChemSusChem* **10**, 3794-2803 (2017)
32. S.A. Paniagua, A.J. Giordano, O'Neil L. Smith, S. Barlow, H. Li, N.R. Armstrong, J.E. Pemberton, J.-L. Brédas, D. Ginger, S.R. Marder, *Chem. Rev.* 2016, **116** (12), 7117-7158
33. I. Lange, S. Reiter, J. Kniepert, F. Piersimoni, M. Pätzelt, J. Hildebrandt, T. Brenner, S. Hecht, D. Neher, *Appl. Phys. Lett.* **106**, 113302 (2015)

34. I. Lange, S. Reiter, M. Pätzelt, A. Zykov, A. Nefedov, J. Hildebrandt, S. Hecht, S. Kowarik, C. Wöll, G. Heimel, D. Neher, *Adv. Funct.* **24**, 7014-7024 (2014)
35. C. Wood, H. Li, P. Winget, J.-L. Brédas, *J. Phys. Chem. C* **116**, 19125-19133 (2012)
36. M. Saliba, T. Matsui, J.-Y. Seo, K. Domanski, J.-P. C.-Baena, M. K. Nazeeruddin, S. M. Zakeeruddin, W. Tress, A. Abate, A. Hagfeldt, M. Grätzel, *Energy Environ. Sci.* **9**, 1989-1997 (2016)
37. H. Zhang, J. Cheng, F. Lin, H. He, J. Mao, K.S. Wong, A.K.-Y. Jen, W.C.H. Choy, *ACS Nano* **10**, 1503-1511 (2016)
38. F. Jiang, W.C.H. Choy, X. Li, D. Zhang, J. Cheng, *Adv. Mater.* **27**, 2930-2937 (2015)
39. X. Yin, P. Chen, M. Que, Y. Xing, W. Que, C. Niu, J. Shao, *ACS Nano* **10**, 3630-3636 (2016)
40. D.K. Owens, R.C. Wendt, *J. Appl. Polym. Sci.* **13**, 1741-1747 (1969)
41. *Practical Surface Analysis (Second Edition) Volume 1: Auger and X-ray Photoelectron Spectroscopy* Edited by D. Briggs, M. P. Seah © 1990 John Wiley & Sons Ltd., page 183
42. S. Tanuma, C.J. Powell, D.R. Penn, *Surf. Interf. Anal.* **21**, 165-176 (1993)
43. R. Lushtinetz, A.F. Oliveira, J. Frenzel, J.-O. Joswig, G. Seifert, H.A. Duarte, *Surface Science* **602**, 1347-1359 (2008)
44. T. Singh, T. Miyasaka, *Adv. Energy Mater.* **8**, 1700677 (2018)
45. M. Saliba, T. Matsui, K. Domanski, J.-Y. Seo, A. Ummadisingu, S.M. Zakeeruddin, J.-P. C.-Baena, W.R. Tress, A. Abate, A. Hagfeldt, M. Grätzel, *Science* **354**, 206-209 (2016)
46. T.J. Jacobsson, J.-P.C.-Baena, E.H. Anaraki, B. Philippe, S.D. Stranks, M.E.F. Bouduban, W. Tress, K. Schenk, J. Teuscher, J.-E. Moser, H. Rensmo, A. Hagfeldt, *J. Am. Chem. Soc.* **138**, 10331-10343 (2016)
47. D. Bi, W. Tress, M.I. Dar, P. Gao, J. Luo, C. Renevier, K. Schenk, A. Abate, F. Giordano, J.-P.C.-Baena, J.-D. Decoppet, S.M. Zakeeruddin, M.K. Nazeeruddin, M. Grätzel, A. Hagfeldt, *Sci. Adv.* **2**, e1501170 (2016)
48. C.-C. Chueh, C.-Z. Li, A.K.-Y. Jen, *Energy Environ. Sci.* **8**, 1160-1189 (2015)
49. M. Deepa, M. Salado, L. Calio, S. Kazim, S.M. Shivaprasad, S. Ahmad, *Phys. Chem. Chem. Phys.* **19**, 4069-4077 (2017)
50. B. de Boer, A. Hadipour, M.M. Mandoc, T. van Woudenberg, P.W.M. Blom, *Adv. Mater.* **17**, 621-625 (2005)
51. I.M. Dharmadasa, Y. Rahaq, A.A. Ojo, T.I. Alanazi, *J. Mater. Sci: Mater. Electron.* **30**, 1227-1235 (2019)



52. J.-W. Lee, S.-G. Kim, S.-H. Bae, D.-K. Lee, O. Lin, Y. Yang, N.-G. Park, *Nano Lett.* **17**, 4270-4276 (2017)
53. G.A. Nemnes, C. Beslega, V. Stancu, D.E. Dograu, L.N. Leonat, L. Pintilie, K. Torfason, M. Ilkov, A. Monalescu, I. Pintilie, *J. Phys. Chem. C* **121**, 11207-11214 (2017)
54. G.A. Nemnes, C. Beslega, A.G. Tomulescu, A. Palici, L. Pintilie, A. Monolescu, I. Pintilie, *Sol. Energy* **173**, 976-983 (2018)
55. G.A. Nemnes, C. Besleaga, A.G. Tomulescu, L.N. Leonat, V. Stancu, M. Florea, A. Monolescu, I. Pintilie, *J. Mater. Chem. C*, DOI: 10.1039/C8TC05999C (2019), in press



# Chapter 4: Benzyl phosphonic acid SAMs in p-i-n architecture

---

*Your small support could accomplish a big dream...*

- *Md. Rishad Sakhi*

*Addendum to Chapter 3: Modification of NiOx hole transport layers with 4-bromobenzylphosphonic acid and its influence on the performance of lead halide perovskite solar cells*

## Introduction

This chapter covers the background and extended work done to support the *Chapter 3: Modification of NiO<sub>x</sub> hole transport layers with 4-bromobenzylphosphonic acid and its influence on the performance of lead halide perovskite solar cells.*

As an extension to the previous chapter, this chapter presents the influence of the functionalized benzylphosphonic acid (R-BPA) based SAMs on the photovoltaic performance of the Cs<sub>0.1</sub>(FA<sub>0.83</sub>MA<sub>0.17</sub>)<sub>0.9</sub>Pb(I<sub>0.83</sub>Br<sub>0.17</sub>)<sub>3</sub> (CsFAMA) based triple cation lead halide perovskite solar cells. The R-BPA SAMs are used to modify the interface between the HTL (i.e. NiO<sub>x</sub>), and the absorber layer (i.e. CsFAMA). According to Lange et al., free standing gas phase benzylphosphonic acid (BPA), 4-bromobenzyl phosphonic acid (Br-BPA), 4-fluorobenzyl phosphonic acid (F-BPA), 4-aminobenzyl phosphonic acid (NH<sub>2</sub>-BPA) have dipole moment of 0.4 D, 2.3 D, 2.0 D, and -0.9 D respectively [1]. Similarly, Rühle et al. reported a dipole moment for 4-nitrobenzyl phosphonic acid (NO<sub>2</sub>-BPA) to be 5.1 D [2]. The dipole moments for 4-methoxybenzyl phosphonic acid (OCH<sub>3</sub>-BPA) was calculated to be -0.93 D relative to ethylphosphonic acid modified AlO<sub>x</sub> surface [3]. The phosphonic acid groups act like anchors on top of NiO<sub>x</sub> and the functional groups act like seeds for the absorber layer on which it crystallizes [1, 4-6].

In a study done by Jiang et al., for organic solar cells, it was reported that low temperature processing of metal oxides may leave behind defects which may cause poor interfacial performance [7]. In efforts to improve photovoltaic performance of perovskite solar cells, He et al. successfully showed that the NiO<sub>x</sub> and MAPI<sub>1-x</sub>Cl<sub>x</sub> interface modification can be helpful [8].

In conventional architecture for perovskite solar cells, different self assembled monolayers (SAMs) such as fullerene based SAMs (C<sub>60</sub>-SAM) and 3-aminopropionic acid based SAMs have been studied [9, 10]. Yang et al. investigated the effects of phosphonic acid based SAM on zinc oxide (ZnO) and cadmium sulphide (CdS) interface [11]. In inverted architecture, Wang et al. modified NiO<sub>x</sub> and MAPI interface by using functionalized benzoic acid (BA) SAMs to improve the photovoltaic performance. They reported enhanced PCEs > 18% due to bromo functionalized BA SAM [12]. They outline the importance of the dipole moment of the different functional groups such as methoxy- (OCH<sub>3</sub>-), amino- (NH<sub>2</sub>-) and bromo- (Br-) in BA for affecting open circuit voltage (V<sub>OC</sub>). The importance of dipole moment was also emphasized in a review by Zhao et al. and effect of band bending was studied by Zhang

et al., where they also outline different materials for passivation of different interfaces [13,14].

**Figure 27A** represents the schematic of NiO<sub>x</sub>/R-BPA SAM/perovskite interface with the red arrows indicating the direction of the dipole with respect to NiO<sub>x</sub>. According to Goh et al. in their investigation on TiO<sub>2</sub>/polymer interface using BA SAMs and Wang et al. in their investigation on NiO<sub>x</sub>/perovskite interface using BA SAMs, the dipole of the SAMs could introduce a step in the vacuum level under the effect of an electric field [12,15]. If the dipole is directed towards the NiO<sub>x</sub> (example Br-BPA and F-BPA) then the band edge is expected to shift downward and therefore leading to an increased V<sub>OC</sub>. Similarly, if the dipole is directed away from the NiO<sub>x</sub> (example NH<sub>2</sub>-BPA and OCH<sub>3</sub>-BPA) then the reverse would happen. The band bending diagram of the shift is shown in the **Figure 27B** where the change in the value of the energy gap between valence band of NiO<sub>x</sub> and perovskite is indicated by  $\delta$ . If the value of  $\delta$  decreases to  $\delta-y$ , the hole extraction improves and therefore, higher J<sub>SC</sub> can be achieved. The better alignment of the bands also leads to improved V<sub>OC</sub> as it is dependent upon the band alignments of NiO<sub>x</sub> (valence band), perovskite (valence band and conduction band), and PC<sub>60</sub>BM (conduction band) (as shown in this work) [16].

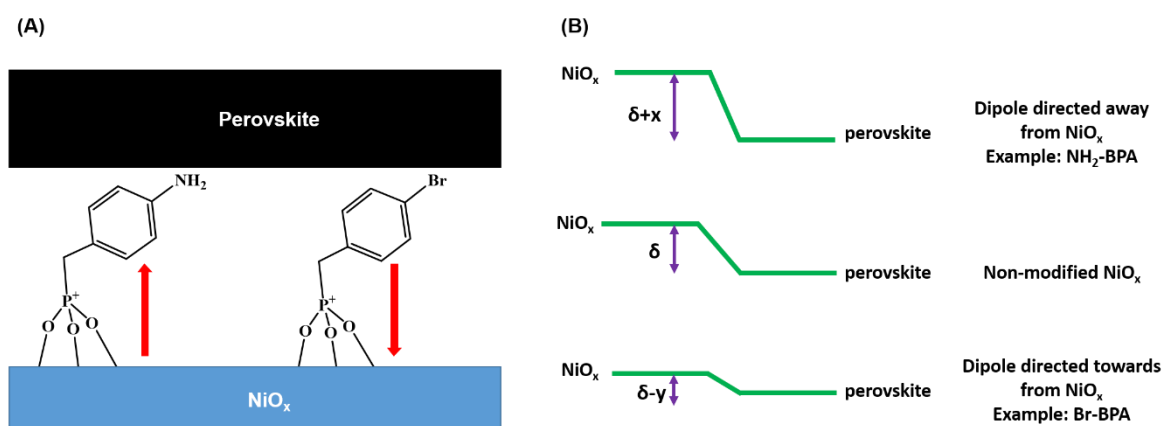


**Figure 27:** Schematic representation of (A) Br- and NH<sub>2</sub>-functionalized BPA based SAMs on NiO<sub>x</sub> surface. The red arrows indicate the directed dipole of the molecule towards or away from the NiO<sub>x</sub>. (B) Band bending diagram of the band edges of NiO<sub>x</sub> and perovskite and the effect of dipole moments on energy gap between the band edges of NiO<sub>x</sub> and perovskite. Here ' $\delta+x$ ' indicates the increase in the gap when dipole is directed away from NiO<sub>x</sub>, and ' $\delta-y$ ' indicates decrease when dipole is directed towards the NiO<sub>x</sub> with respect to the non-modified NiO<sub>x</sub> having a constant gap of ' $\delta$ '. The value of ' $x$ ' and ' $y$ ' depend upon the nature of dipole and its impact on the energy gap.

## Materials and methods

### Sample and solar cell preparation

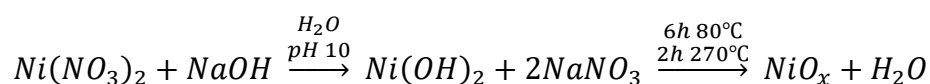
All chemicals and solvents were used as purchased without any further purification. Nickel(II) nitrate hexahydrate and sodium hydroxide was purchased from Fluka and VWR, respectively. Lead iodide, lead bromide, formamidinium iodide and PC<sub>60</sub>BM were purchased from TCI, Alfa Aesar, GreatCell Solar and Solenne, respectively. The other chemicals used in this study, including the phosphonic acid molecule, and all the solvents were purchased from Merck (Sigma Aldrich).

### Front contact

In inverted architecture, indium doped tin oxide on glass substrates (g-ITO) with substrate size of (15 × 15 × 1.1 mm<sup>3</sup>) were used as anodes. It has surface resistance of 15 Ω cm<sup>2</sup>. The substrates were cleaned in a three-step process. Firstly, the substrates were wiped using acetone, followed by an ultra-sonication bath in isopropanol for 10 min. The substrates were then dried using a nitrogen (N<sub>2</sub>) gun. Lastly, the substrates were treated with oxygen (O<sub>2</sub>) plasma for 3 min.

### NiO<sub>x</sub> nanoparticles

NiO<sub>x</sub> nanoparticles were synthesised as reported in Weber et al. [17-20]. NiO<sub>x</sub> nanoparticles were synthesized by dispersing 50 mM of nickel(II) nitrate hexahydrate in 10 mL deionized water and stirred for 5 min. The pH of the solution was adjusted to 10 by adding small amounts of 10 M sodium hydroxide dropwise. The colour of the solution changed to light green.



The side products were removed by washing the colloidal precipitate with deionized water. The light green residue was then dried at 80°C for 6 h and then calcinated at 270°C for 2 h. This resulted in a non-stoichiometric black NiO<sub>x</sub> nanoparticles. The NiO<sub>x</sub> thin films were spin coated on g-ITO substrates by using a 20 mg/mL solution of the NiO<sub>x</sub> nanoparticles in deionized water at different rpm for 30 sec.

## **NiO<sub>x</sub> sol-gel**

A NiO<sub>x</sub> thin film was prepared through a sol-gel method as reported by Chen et al. [21]. The thin films were deposited using a solution prepared by dispersing 0.1 M of nickel acetate in a 0.1 M ethanolamine in an isopropanol solution. The blue solution was then sealed and stirred at 70°C overnight. The colour of the solution turned to green from blue overnight. The thin films were spin coated on the g-ITO substrate at different rpm for 30 sec. The substrate was then annealed at 275°C for 1 h. The cesium doped NiO<sub>x</sub> (Cs:NiO<sub>x</sub>) was prepared by the same method. To achieve 1% doping of Cs, 1 mM equivalent of Cs was added in the nickel acetate and ethanolamine solution in isopropanol.

## **Deposition of R-BPA SAM**

To functionalize the g-ITO/NiO<sub>x</sub> substrates made from NiO<sub>x</sub> nanoparticles, we prepared 2 mM solutions of different functionalized benzylphosphonic acid molecules in acetonitrile. The different functionalized molecules were: BPA, Br-BPA, F-BPA, NO<sub>2</sub>-BPA, NH<sub>2</sub>-BPA, and OCH<sub>3</sub>-BPA.

## **Dip coating**

The deposition of phosphonic acid SAMs on the g-ITO/NiO<sub>x</sub> substrates made from NiO<sub>x</sub> nanoparticles were carried out using dip coating method. Here, the substrates were dipped in to the solutions for 1 min to allow the molecules to self assemble. The phosphonic group of the molecule acts like an anchor to the NiO<sub>x</sub> interface and the functional group acts like a seed layer for the perovskite on which the perovskite crystallizes. In an ideal situation, the phosphonic acid molecules chemisorb onto the NiO<sub>x</sub>. Since the phosphonic acid molecules have different functional groups, they have different dipole moments which may affect the interfacial properties of NiO<sub>x</sub> and perovskite. To achieve SAMs, after 1 min deposition time, the substrates were rinsed using fresh solvent and then dried using a N<sub>2</sub>-gun. The rinsing process allows to get rid of the non-adsorbed phosphonic acid molecules. This allows us to get rid of any aggregation of molecules which may adversely affect the device performance. The sol-gel based Cs:NiO<sub>x</sub> was also dip coated under congruent conditions.

## **Dynamic spin coating**

The NiO<sub>x</sub> nanoparticles based g-ITO/NiO<sub>x</sub> substrates were modified using BPA, Br-BPA, and NH<sub>2</sub>-BPA molecules using 5 mM solutions. The solutions were filtered using a 0.45 μm

PVDF syringe filter and was further diluted to a 2.5 mM solution to achieve a clear solution. The solutions were then used to dynamically spin coat the substrates inside the glovebox at 2000 rpm for 30 s. The solution was dropped on top of the spinning substrates after first 5 s allowing 25 s of post drop spin. The substrates were cleaned using another round of dynamic spin coating with pure acetonitrile under same spinning conditions as the phosphonic acid solution. This helps to clean the substrate of any non-adsorbed phosphonic acid molecule.

### **Preparation of CsFAMA perovskite**

The preparation of the CsFAMA perovskites were same as described in previous chapter.

### **Electron transport layer and back contact**

A phenyl-C61-butyric acid methyl ester (PC<sub>60</sub>BM) solution was prepared with a concentration of 20 mg/mL in chlorobenzene. The solution was stirred overnight and then it was filtered using a 0.45 μm PTFE syringe filter. The thin film was spin coated inside the glovebox at 2000 rpm for 1 min and later after optimization 4000 rpm for 30 sec. A 120 nm thin silver (Ag) electrode was coated using thermal evaporator under very low pressure  $1 \times 10^{-5}$  bar on the PC<sub>60</sub>BM layer using a 0.09 cm<sup>2</sup> shadow mask. The schematic depicting the process of fabricating a p-i-n architecture based g-ITO/NiO<sub>x</sub>.

### **Characterization techniques**

XRD was performed on a PANalytical Empyrean system using Cu K<sub>α</sub> radiation. Ultraviolet-visible (UV-Vis) spectroscopy measurements were done using the UV/VIS Spectrometer – Lambda 35 by Perkin Elmer. The layer thicknesses were measured by surface profilometry using a DektakXT device by Bruker and the surface morphology of the perovskite films was characterized by scanning electron microscopy (SEM) images acquired on a Zeiss-Supra 40 scanning electron microscope with an in-lens detector and 5 kV acceleration voltage.

Contact angle measurements of the NiO<sub>x</sub> films before and after the modification with R-BPA were carried out on a Krüss DSA100 system using water liquid.

The current density – voltage (JV) curves and maximum power point (MPP) tracking measurements of the solar cells were performed using Keithley 2400 source meter and a LabView-based software inside a glove box (nitrogen atmosphere). For the JV curves, the scan rates were adjusted to 100 mVs<sup>-1</sup> in the forward (fwd) direction (-0.1 V to 1.5 V) and



backward (bwd) direction (1.5 V to -0.1 V) for both light and dark measurements. In few chases the illumination area was defined using a shadow mask (0.0702 cm<sup>2</sup>) and the light was provided by a Dedolight DLH500 lamp calibrated to an intensity of 100 mWcm<sup>-2</sup> using a pyranometer from Kipp & Zonen. The External Quantum Efficiency (EQE) spectra were acquired using a MuLTImode 4 monochromator (Amko) equipped with a 75 W xenon lamp (LPS 210-U, Amko), a lock-in amplifier (Stanford Research Systems, Model SR830), and a Keithley 2400 source meter. The monochromatic light was chopped at a frequency of 30 Hz and the measurement setup was spectrally calibrated with a silicon photodiode (Newport Corporation, 818-UV/DB).

## Results and discussion

### Dip coated R-BPA SAMs

The thin film XRD pattern for NiO<sub>x</sub> nanoparticles (powder) show reflexes at 2θ equals 32.7°, 43.2°, 62.7°, 75.4° and 79.3° for (111), (200), (220) (311) and (222) lattice planes respectively as illustrated by **Figure 28A**. The mean crystal size of the NiO<sub>x</sub> nanoparticles were calculated to be 9.4 nm using Scherrer's equation (**equation 13**) where τ represent the mean crystal size of the material, *K* represents the shape factor (~0.9), λ represents the wavelength of the X-ray used, β (in radians) represents the full width half maxima of the peak, and θ (in radians) represent the Bragg's angle.

The XRD patterns for NiO<sub>x</sub> sol-gel thin films were difficult to obtain due to the resolution of the device and therefore, could not be done. However, it was possible to perform successful ultraviolet-visible (UV-Vis) spectroscopy for the different kinds of NiO<sub>x</sub> under investigation as shown in **Figure 28B**. It was found that the transmission properties of NiO<sub>x</sub> nanoparticles based thin films were better than the NiO<sub>x</sub> sol-gel.

$$\tau = \frac{K\lambda}{\beta \cos\theta} \quad (13)$$

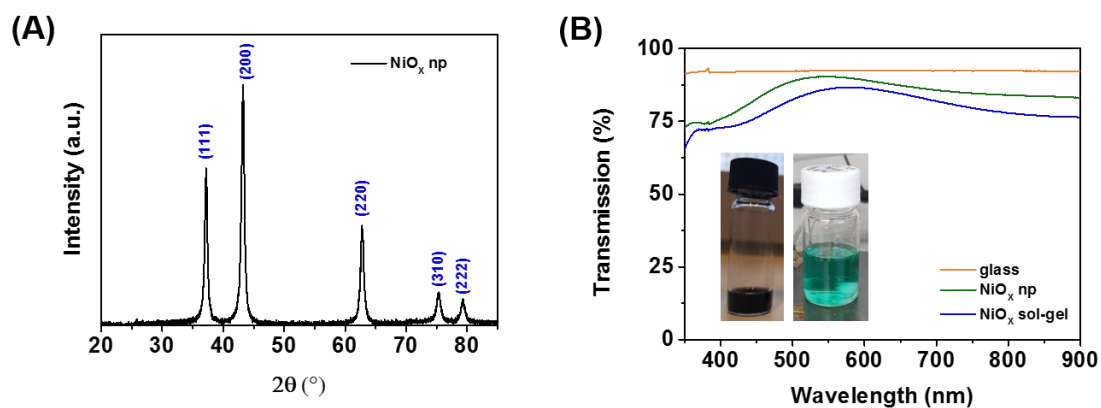


**Figure 28:** (A) XRD reflexes for  $\text{NiO}_x$  nanoparticles based thin films and (B) UV-Vis transmission curves for glass and nanoparticles and sol-gel based  $\text{NiO}_x$  thin films. The inset contains pictures of the solutions for  $\text{NiO}_x$  nanoparticles in deionized water and  $\text{NiO}_x$  sol-gel solution before thin film deposition.

The modification of the  $\text{NiO}_x$  surface by R-BPA molecules through dip coating was confirmed by performing contact angle measurements. The measured values are listed in the **Table 9** and the images of water drops can be seen in **Figure 29**.



**Figure 29:** Images of water drops on  $\text{NiO}_x$  nanoparticles based thin films modified by dip coated R-BPA molecules.

**Table 9:** Contact angles (CAs) of water measured on NiO<sub>x</sub> nanoparticles based thin films modified by dip coated R-BPA molecules.

|        | <i>NiO<sub>x</sub></i> | <i>NiO<sub>x</sub>/Br-BPA</i> | <i>NiO<sub>x</sub>/F-BPA</i> | <i>NiO<sub>x</sub>/NH<sub>2</sub>-BPA SAM</i> | <i>NiO<sub>x</sub>/NO<sub>2</sub>-BPA</i> | <i>NiO<sub>x</sub>/OC-H<sub>3</sub>-BPA</i> | <i>NiO<sub>x</sub>/BP-A</i> |
|--------|------------------------|-------------------------------|------------------------------|---|---|---|-----------------------------|
| CA (°) | 12.8±0.1               | 71.1±0.9                      | 48.8±0.9                     | 42.3±1.2                                      | 29.5±0.6                                  | 51.2±1.8                                    | 48.8±1.3                    |

The measured values show a clear change in the contact angles for the modified samples. The NiO<sub>x</sub> layer with Br-BPA molecule modification showed highest change with respect to the non-modified NiO<sub>x</sub>. The value changed from 12.8±0.1° to 71.1±0.9°. The contact angle for F-BPA molecule modified NiO<sub>x</sub> film were 48.8±0.9°. Since fluorine has higher electronegativity compared to bromine therefore, F-BPA should be more polar compared to Br-BPA. Therefore, the contact angle of F-BPA modified NiO<sub>x</sub> layer must be higher than Br-BPA modified NiO<sub>x</sub> layer. However since the contact angle values suggest otherwise, and therefore, this brings the concern of the coverage of F-BPA SAMs on the NiO<sub>x</sub> thin film compared to Br-BPA SAMs.

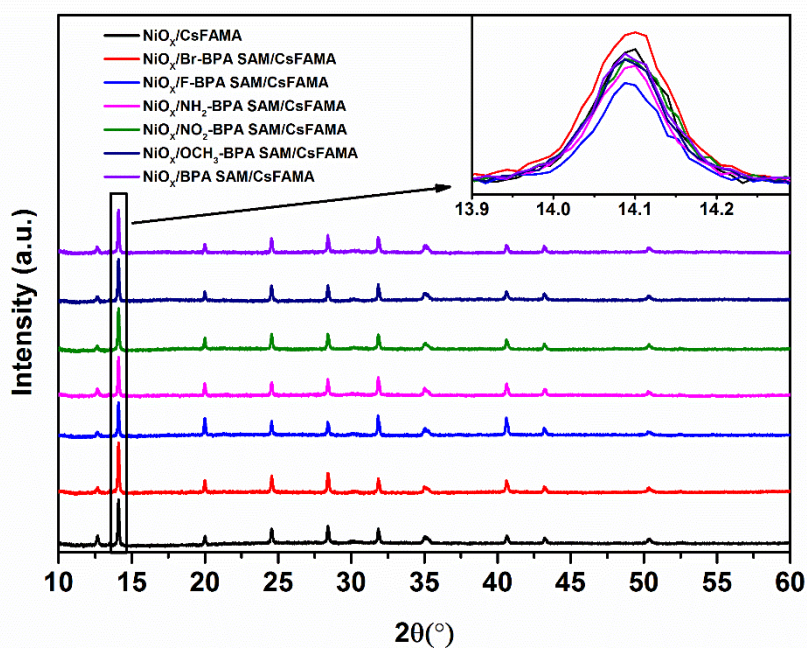


**Figure 30:** XRD reflexes for CsFAMA perovskites deposited on NiO<sub>x</sub> nanoparticles based thin films dip coated in R-BPA solution.

**Table 10:** XRD reflexes for (110) and (220) lattice planes in CsFAMA perovskites on NiO<sub>x</sub> nanoparticles based thin films which were modified by dip coated R-BPA molecules.

|       | <i>CsFAMA</i> | <i>Br-BPA</i> | <i>F-BPA</i> | <i>NH<sub>2</sub>-BPA</i> | <i>NO<sub>2</sub>-BPA</i> | <i>OCH<sub>3</sub>-BPA</i> | <i>BPA</i> |
|-------|---------------|---------------|--------------|---------------------------|---------------------------|----------------------------|------------|
| (110) | 14.10         | 14.10         | 14.09        | 14.10                     | 14.09                     | 14.09                      | 14.09      |
| (220) | 28.40         | 28.43         | 28.37        | 28.40                     | 28.37                     | 28.40                      | 28.40      |

The XRD reflexes for CsFAMA perovskites on NiO<sub>x</sub> nanoparticles based thin film showed prominent perovskite peaks at 2θ equals 14.10° and 28.40° for (110) and (220) lattice planes respectively [22-24]. The peaks for CsFAMA perovskites on dip coated R-BPA SAM on NiO<sub>x</sub> thin films showed similar 2θ. The XRD reflexes are shown in **Figure 30** and the values are listed in **Table 10**. The minor differences in the value of the 2θ could be assigned to lattice strain.

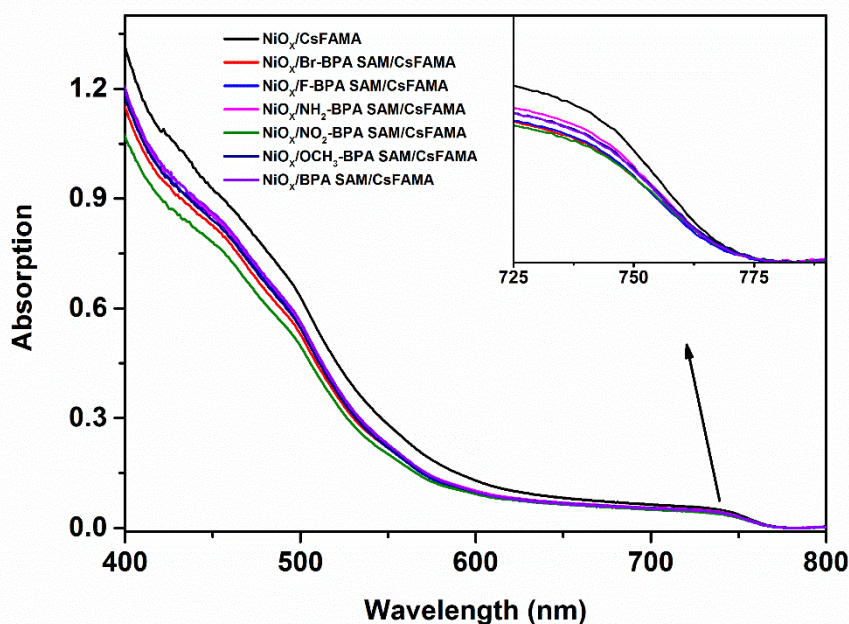


**Figure 31:** UV-Vis absorption spectra for CsFAMA perovskites deposited on NiO<sub>x</sub> nanoparticles based thin films dip coated in R-BPA solution.

The UV-Vis absorption spectra for CsFAMA perovskite on NiO<sub>x</sub> nanoparticles based thin films modified by dip coated R-BPA molecules showed similar absorption onset at ~770 nm (see **Figure 31**). The slight variations observed in the wavelength range of 650 nm to 400 nm is due to special samples prepared for these measurements having varying thickness of the CsFAMA films (100-200 nm).

The top view scanning electron microscopy (SEM) images of CsFAMA perovskites on NiO<sub>x</sub> modified by R-BPA SAMs indicate homogeneous distribution of perovskite on the NiO<sub>x</sub> film (**Figure 32**). The mean grain size for five random points on CsFAMA for non-modified NiO<sub>x</sub> samples was  $647.18 \pm 72.71$  nm and for Br-BPA SAM based sample was  $662.2 \pm 71.35$  nm. Similarly the mean values for F-BPA, NH<sub>2</sub>-BPA, NO<sub>2</sub>-BPA, OCH<sub>3</sub>-BPA, and BPA were  $712.4 \pm 80.78$  nm,  $668.5 \pm 75.1$  nm,  $593.4 \pm 162.18$  nm,  $624.5 \pm 116.79$  nm, and  $749 \pm 69.77$  nm respectively. The standard deviations for NO<sub>2</sub>-BPA and OCH<sub>3</sub>-BPA based CsFAMA perovskites suggest varying grain sizes ranging between 400 nm to 800 nm. However, in contrast the grain sizes for F-BPA and BPA based CsFAMA perovskites range between 600 nm to 800 nm and have a narrow distribution.

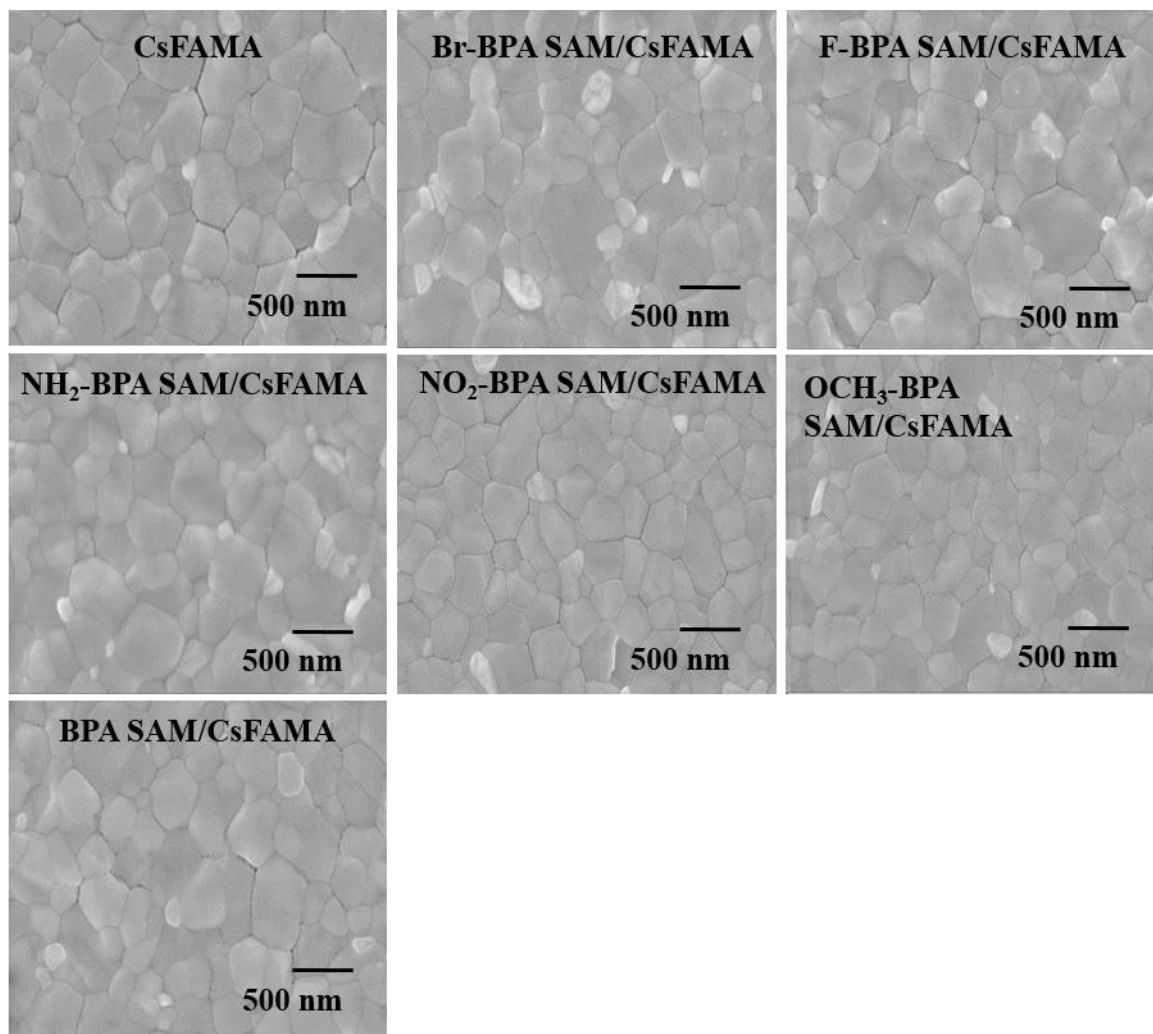


**Figure 32:** Top view SEM images for CsFAMA perovskites on NiO<sub>x</sub> nanoparticles based thin films modified by dip coated R-BPA molecules.

After characterizing the surface of the NiO<sub>x</sub> thin films for presence of R-BPA molecules and their effect on the properties of CsFAMA perovskite, solar cells were fabricated. The champion solar cells with non-modified and Br-BPA modified NiO<sub>x</sub> thin films showed power conversion efficiencies (PCEs) of 11.52% (11.96%) and 14.83% (13.95%) in forward (backward) direction and the mean values for PCE for five cells were at  $10.77 \pm 0.61\%$  ( $11.18 \pm 0.55\%$ ) and  $14.44 \pm 0.31\%$  ( $13.81 \pm 0.40\%$ ) respectively as shown in **Figure 33** and listed in **Table 11**. Similarly the champion solar cell with F-BPA modified NiO<sub>x</sub> thin films showed PCEs of 12.49% (13.40%) with an average of  $12.30 \pm 0.68\%$  ( $11.25 \pm 2.70\%$ ). The improvement in the PCEs is due to the increase of the  $V_{OC}$  of the devices from an average of  $0.928 \pm 0.013$  V ( $0.949 \pm 0.013$  V) to  $0.979 \pm 0.031$  V ( $1.001 \pm 0.015$  V) and  $1.053 \pm 0.015$  V ( $1.041 \pm 0.059$  V) for non-modified to Br-BPA SAM and F-BPA SAM modified NiO<sub>x</sub> thin films respectively.

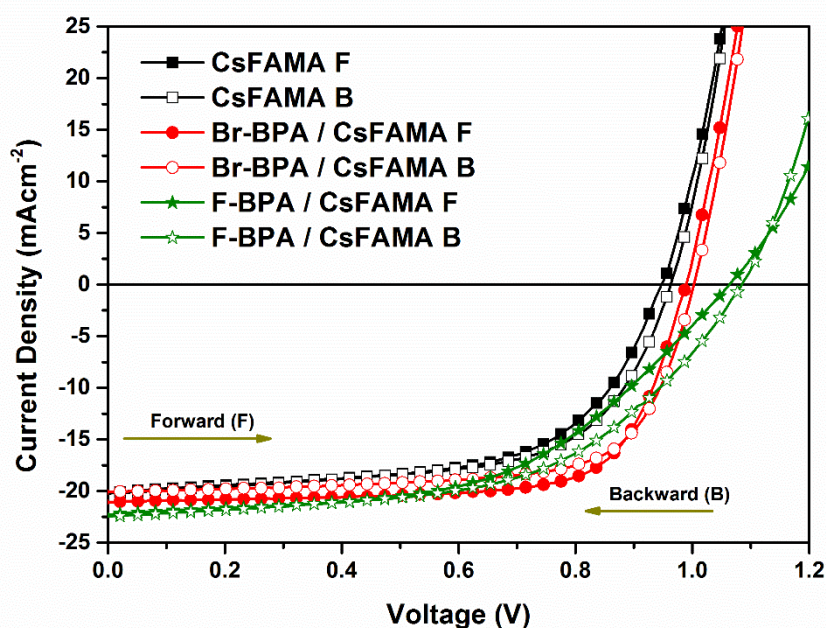


**Figure 33:** JV curves for light (indicated as L in the legends) measurements for forward (F) and backward (B) sweeps for CsFAMA, Br-BPA SAM/CsFAMA and F-BPA SAM/CsFAMA based solar cells.

This improvement in the  $V_{OC}$  is due to the contribution of Br-BPA and F-BPA. The dipole of Br-BPA and F-BPA were directed towards the  $NiO_x$  (**Figure 27**) and therefore, the valence band edge of  $NiO_x$  shifted towards the valence band edge of the perovskite thereby improving the charge extraction and  $V_{OC}$ . The most increase in  $V_{OC}$  is observed due to F-BPA as listed in **Table 11**. The champion devices without any modification had series resistance ( $R_{SER}$ ) of  $6.48 \Omega \text{ cm}^2$  ( $5.21 \Omega \text{ cm}^2$ ) and shunt resistance ( $R_{SH}$ ) of  $171 \Omega \text{ cm}^2$  ( $265 \Omega \text{ cm}^2$ ) compared to F-BPA SAM modified solar cells with  $R_{SER}$  of  $15.09 \Omega \text{ cm}^2$  ( $10.85 \Omega \text{ cm}^2$ ) and  $R_{SH}$  of  $154.32 \Omega \text{ cm}^2$  ( $270.27 \Omega \text{ cm}^2$ ). The difference in the  $R_{SER}$  contributes to the loss of FF and similar  $R_{SH}$  for the devices justify the similar  $J_{SC}$ . The difference in the  $R_{SER}$  could be assigned to the poor coverage of F-BPA on the  $NiO_x$  thin film surface as suspected by the contact angle measurements. Therefore it is safe to assume that F-BPA molecules contribute to the  $R_{SER}$ . However, despite of  $R_{SER}$  and  $R_{SH}$  issues, the improvement in the  $V_{OC}$ s (non-modified  $0.947 \text{ V}$  ( $0.967 \text{ V}$ ) to F-BPA modified  $1.067 \text{ V}$  ( $1.087 \text{ V}$ )) of the devices prove the potential of these molecules as interface modifiers.

**Table 11:**  $V_{OC}$ , absolute  $J_{SC}$ , FF, and PCE values for light measurements of CsFAMA, Br-BPA SAM/CsFAMA and F-BPA SAM/CsFAMA based solar cells along with the mean values for best 5 cells. The values are listed in forward (backward) sweep directions.

| $0.09 \text{ cm}^2$ | $V_{OC}$ (V)                 | $J_{SC}$ ( $\text{mAcm}^{-2}$ ) | FF (%)                     | PCE (%)                    |
|---------------------|------------------------------|---------------------------------|----------------------------|----------------------------|
| CsFAMA              | 0.947 (0.967)                | 20.23 (20.22)                   | 60.55 (61.77)              | 11.52 (11.96)              |
| Mean (5 cells)      | 0.928±0.013<br>(0.949±0.013) | 19.07±0.87<br>(19.01±0.86)      | 61.14±0.14<br>(62.43±0.01) | 10.77±0.61<br>(11.18±0.55) |
| Br-BPA              | 0.987 (1.007)                | 21.06 (20.08)                   | 71.88 (69.60)              | 14.83 (13.95)              |
| Mean (5 cells)      | 0.979±0.031<br>(1.001±0.015) | 21.05±0.59<br>(20.19±0.41)      | 70.65±0.03<br>(68.85±0.02) | 14.44±0.31<br>(13.81±0.40) |
| F-BPA               | 1.067 (1.087)                | 22.30 (22.47)                   | 52.08 (54.35)              | 12.49 (13.40)              |
| Mean (5 cells)      | 1.053±0.015<br>(1.041±0.059) | 22.10±0.39<br>(21.01±2.07)      | 52.68±0.03<br>(50.50±0.46) | 12.30±0.68<br>(11.25±2.70) |

**Figure 34** shows the JV curves for R-BPA modified  $\text{NiO}_x$  thin films which include Br-BPA, F-BPA,  $\text{NH}_2$ -BPA,  $\text{NO}_2$ -BPA,  $\text{OCH}_3$ -BPA, and BPA molecules. They were dip coated on to the  $\text{NiO}_x$  thin films. The values for  $V_{OC}$ ,  $J_{SC}$ , FF, and PCEs are listed in the **Table 12**. The champion solar cells for non-modified samples observed 8.39% (7.85%) PCEs which is lower than the expected performance. The champion solar cell with Br-BPA modification showed the relatively highest improvement in the  $V_{OC}$  of the device as shown in **Table 12**. The improvement in the  $V_{OC}$  of this device was consistent with the previous results seen in **Figure 33**. However, F-BPA modification based champion solar cell displayed similar  $V_{OC}$ s as the reference device.



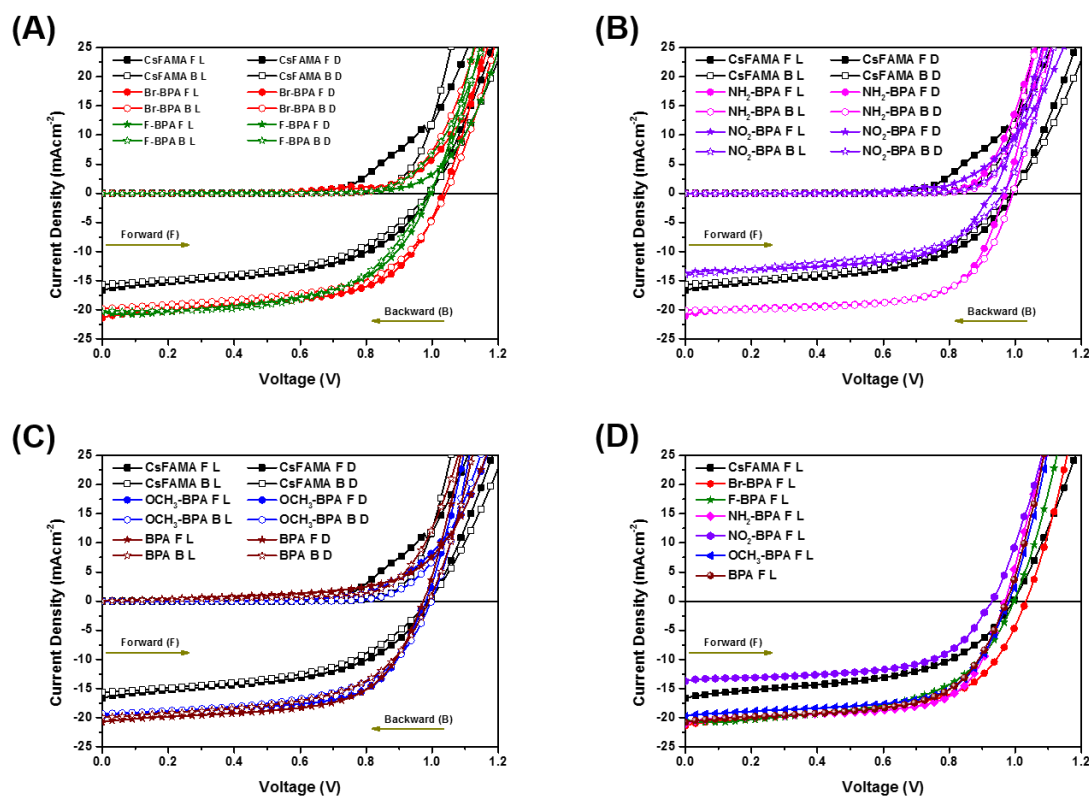


**Figure 34:** JV curves for (A, B, and C) dip coated R-BPA SAM modified NiO<sub>x</sub> thin films in light and dark conditions for forward and backward sweep directions and (D) comparison of the JV curves in light conditions for forward sweep direction.

The NH<sub>2</sub>-BPA modification led to a drop in the V<sub>OC</sub> of the device compared to the reference for forward sweep direction, however, the backward sweep direction values were similar. The drop in the V<sub>OC</sub> due to NH<sub>2</sub>-BPA is expected as the dipole is directed away from the NiO<sub>x</sub> and therefore, the energy gap between the bands increase leading to loss in the V<sub>OC</sub>. However, the scan direction dependency on the performance requires further investigation. The NO<sub>2</sub>-BPA based devices performed worse than the reference as it observed low absolute J<sub>SCS</sub> of 13.73 mAcm<sup>-2</sup> (14.00 mAcm<sup>-2</sup>) compared to other reference and modified devices. This behaviour could be assigned to the relatively smaller grain size for the perovskite in NO<sub>2</sub>-BPA based samples as seen in **Figure 32**. The smaller grain size would lead increase in the recombinations at grain boundaries which would justify lower J<sub>SC</sub> in these devices. These cells also showed difference in the V<sub>OC</sub> depending upon the scan direction. The devices with OCH<sub>3</sub>-BPA and BPA modifications showed similar results and no significant change in the V<sub>OCs</sub> were observed.

One of the consistent issues observed during the fabrication of these devices were in the irreproducibility. Therefore, the attention was diverted towards optimizing the reference devices.

**Table 12:**  $V_{oc}$ , absolute  $J_{sc}$ , FF, and PCE values for light measurements of NiO<sub>x</sub>/CsFAMA, NiO<sub>x</sub>/Br-BPA SAM/CsFAMA, NiO<sub>x</sub>/F-BPA SAM/CsFAMA, NiO<sub>x</sub>/NH<sub>2</sub>-BPA SAM/CsFAMA, NiO<sub>x</sub>/NO<sub>2</sub>-BPA SAM/CsFAMA, NiO<sub>x</sub>/OCH<sub>3</sub>-BPA SAM/CsFAMA, and NiO<sub>x</sub>/BPA SAM/CsFAMA based solar cells in forward (backward) directions. The measurement values are for NiO<sub>x</sub> nanoparticles and dip coated R-BPA SAM based HTL modified solar cells.

| $0.0702 \text{ cm}^2$     | $V_{oc} \text{ (V)}$ | $J_{sc} \text{ (mAcm}^{-2}\text{)}$ | $FF \text{ (\%)}$ | $PCE \text{ (\%)}$ |
|---------------------------|----------------------|-------------------------------------|-------------------|--------------------|
| CsFAMA                    | 0.997 (0.987)        | 16.65 (15.69)                       | 50.91 (51.03)     | 8.39 (7.85)        |
| Br-BPA SAM                | 1.037 (1.037)        | 21.46 (19.83)                       | 57.73 (58.07)     | 12.85 (11.90)      |
| F-BPA SAM                 | 0.997 (0.987)        | 20.42 (20.29)                       | 57.68 (58.76)     | 11.60 (11.69)      |
| NH <sub>2</sub> -BPA SAM  | 0.966 (0.997)        | 21.08 (20.12)                       | 64.65 (65.26)     | 13.13 (13.02)      |
| NO <sub>2</sub> -BPA SAM  | 0.926 (0.966)        | 13.73 (14.00)                       | 59.80 (51.59)     | 7.59 (6.94)        |
| OCH <sub>3</sub> -BPA SAM | 0.977 (0.997)        | 19.83 (19.36)                       | 63.34 (58.11)     | 12.14 (12.11)      |
| BPA SAM                   | 0.977 (0.987)        | 20.08 (19.96)                       | 61.13 (57.24)     | 12.42 (11.28)      |

**Figure 35** represents the JV curves for CsFAMA based solar cells where the CsFAMA perovskite films were annealed for 15 min or 1 h after spin coating. The champion performance of 15 min annealing time based devices showed PCEs of 15.43% (15.32%) compared to 13.00% (13.20%) for the normal 1 h annealed perovskites. The devices showed negligible hysteresis as listed in **Table 13**. However, similar to previous observations, the irreproducibility of these devices remained.

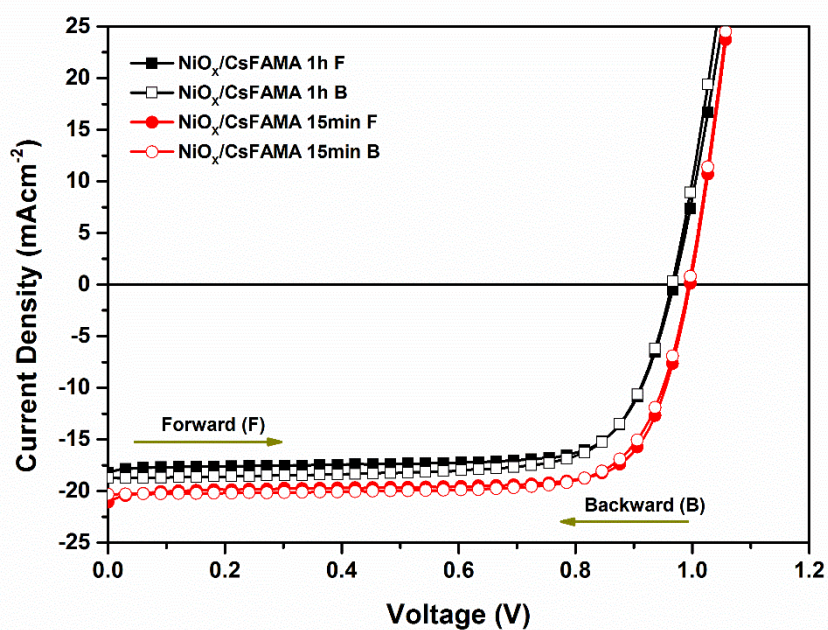


**Figure 35:** JV curves for 15 min and 1 h annealing time for CsFAMA based solar cells in light conditions for forward and backward sweep directions.

**Table 13:**  $V_{OC}$ , absolute  $J_{SC}$ , FF, and PCE values for light measurements of  $NiO_x/CsFAMA$  based solar cells for 1 h and 15 min CsFAMA perovskite annealing time at  $100^\circ C$ .

| $0.09\text{ cm}^2$ | $V_{oc}$ (V)  | $J_{sc}$ ( $\text{mAcm}^{-2}$ ) | FF (%)        | PCE (%)       |
|--------------------|---------------|---------------------------------|---------------|---------------|
| 1 h                | 0.967 (0.967) | 18.20 (18.73)                   | 74.33 (73.36) | 13.00 (13.20) |
| 15 min             | 0.997 (0.997) | 21.07 (20.31)                   | 73.66 (75.69) | 15.43 (15.32) |

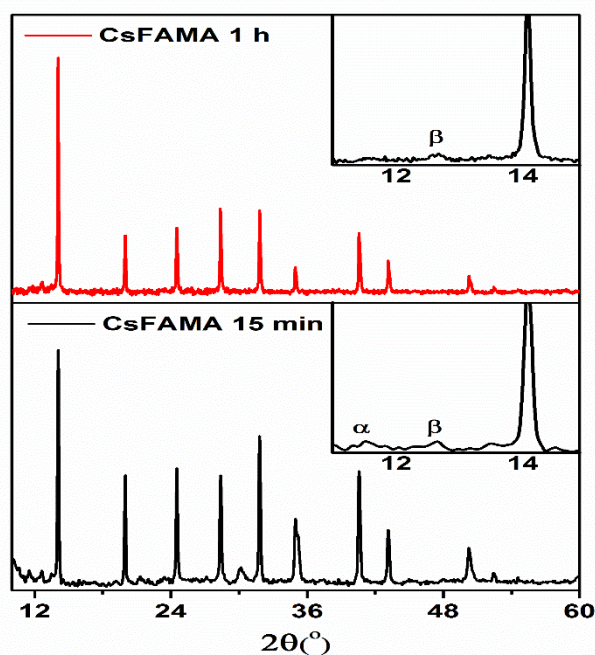


**Figure 36:** XRD reflexes for CsFAMA films annealed at 15 min and 1 h. The inset focuses on the presence of  $\delta$ -FAPbI<sub>3</sub> for 15 min annealed films and cubic PbI<sub>2</sub> for both the samples.

The XRD reflexes of these perovskite layers revealed formation of the perovskite as seen in **Figure 36**. The presence of  $\delta$ -FAPbI<sub>3</sub> ( $2\theta$  equals  $11.51^\circ$ ) and cubic PbI<sub>2</sub> ( $2\theta$  equals  $12.66^\circ$ ) for the 15 min annealed perovskite films were also observed. The 1 h annealed films only showed presence of cubic PbI<sub>2</sub>. The absence of  $\delta$ -FAPbI<sub>3</sub> for the 1 h annealed films could suggest that the perovskite requires more than 15 min to achieve the desired composition with slight residual cubic PbI<sub>2</sub>. The presence of cubic PbI<sub>2</sub> in excess has been proven to be beneficial for the crystallization of perovskite, however, it also affects the stability of the device in the long run.

To further investigate the reason for the inconsistent performance of these solar cells and to optimize the fabrication process, the focus was shifted towards NiO<sub>x</sub> films. The quality of these films could dictate the quality of chemisorption of the R-BPA molecules for SAM formation and further could explain the inconsistent reference cells. Therefore, the nanoparticles based NiO<sub>x</sub> thin films were investigated through top view SEM images (**Figure 37**). Three solutions (solution 1-3) with identical concentrations (20 mg/mL), fourth solution (solution 4) with half concentration (20 mg/2 mL), and fifth solution (solution 5) with double concentrations (40 mg/mL) in deionized water were used. These concentrations were used to investigate the potential of differences in the thin film quality for same

concentrations and its comparison with respect to half and double the usual concentrations. The spin coating conditions for these films were identical and coated on ITO substrates.

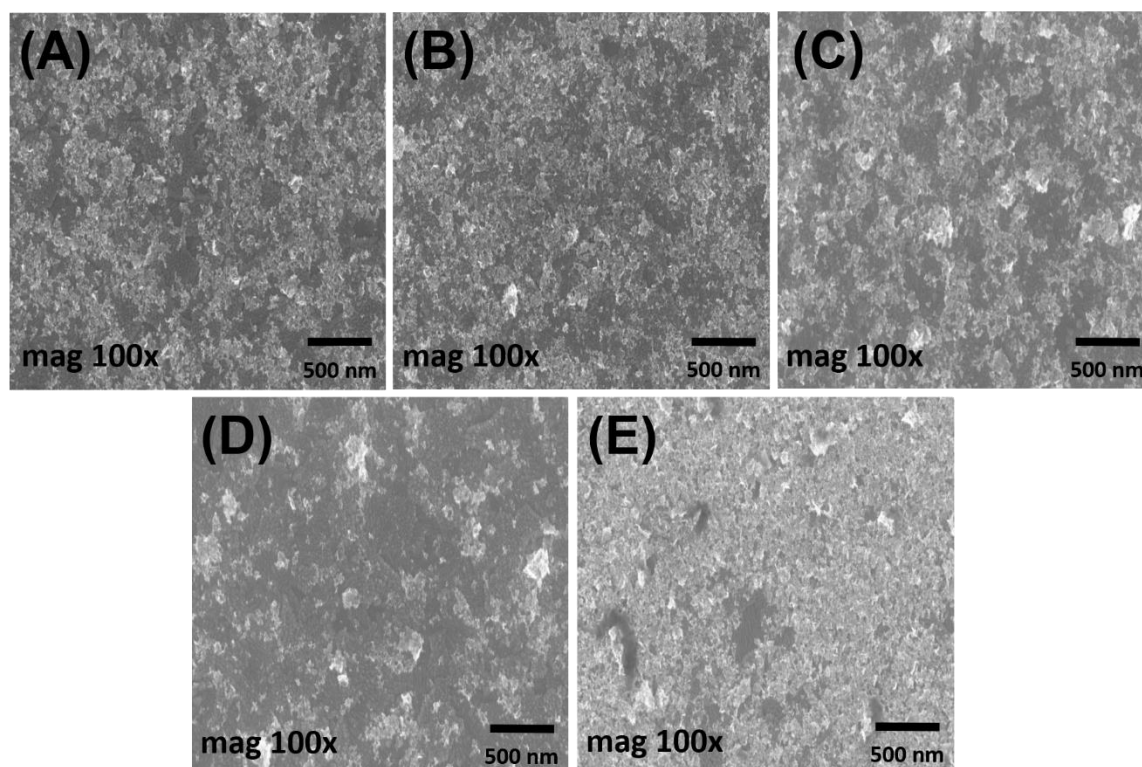


**Figure 37:** Top view SEM images for NiO<sub>x</sub> nanoparticles based thin films on ITO with concentrations (A-C) 20 mg/mL, (D) 20 mg / 2 mL, and (E) 40 mg/mL.

The top view SEM images showed non-homogeneous distribution of NiO<sub>x</sub> on the ITO substrates for solutions 1-3. The white substance spread across the substrates indicate NiO<sub>x</sub> and the dark grey patches indicate the ITO. This conclusion was made after observing the image of solution 4 which had half the concentration of solutions 1-3. Since the concentration was half, the amount of NiO<sub>x</sub> spread across the substrate (the white substance) was visibly less thereby exposing the grey ITO area. In contrast, the SEM image for solution 5 with double concentration indicated a homogeneous distribution of NiO<sub>x</sub> across the g-ITO substrate. Even though the homogeneous distribution of the film for solution 5 with 40 mg/mL concentration was best, it brought new issues with filtering the solution after ultrasonication as the particles would clog the filter. Therefore, consistently reproducing the solution for spin coating became an issue.

To eliminate the inconsistency brought by the quality of NiO<sub>x</sub> nanoparticles based thin films further investigations were carried out using sol-gel processed Cs doped NiO<sub>x</sub>.

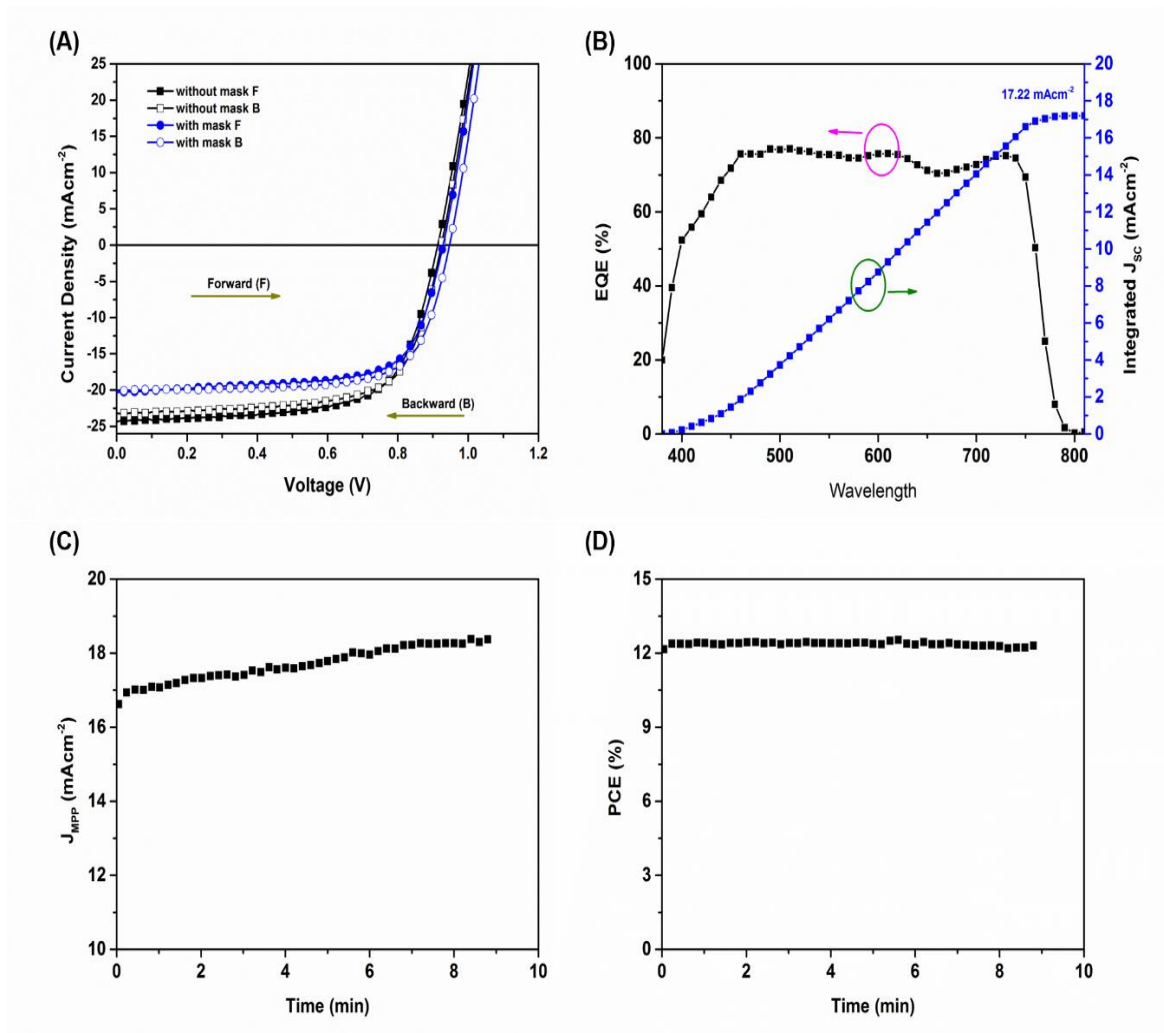


**Figure 38:** (A) JV curves for Cs:NiO<sub>x</sub>/CsFAMA based solar cells without and with mask (without 0.09 cm<sup>2</sup> and with 0.0702 cm<sup>2</sup>), (B) EQE and integrated J<sub>sc</sub>, (C-D) maximum power point tracking of J<sub>MPP</sub> and PCE.

The Cs:NiO<sub>x</sub> thin films were prepared using a sol-gel method and the solar cells were fabricated by annealing CsFAMA perovskites for 1 h. The JV curves for these devices were measured without and with a shadow mask with areas 0.09 cm<sup>2</sup> and 0.0702 cm<sup>2</sup> respectively as shown in **Figure 38A**. The PCEs of the device fell from 14.53% (14.37%) to 12.77% (13.34%) due to the fall in the J<sub>sc</sub> from 24.33 mAcm<sup>-2</sup> (23.21 mAcm<sup>-2</sup>) to 20.31 mAcm<sup>-2</sup> (20.01 mAcm<sup>-2</sup>). The R<sub>SH</sub> for without and with mask JV curves were 483.09 Ω cm<sup>2</sup> (2152.85 Ω cm<sup>2</sup>) and 148.36 Ω cm<sup>2</sup> (735.29 Ω cm<sup>2</sup>) respectively. The R<sub>SER</sub> for without and with mask JV curves were 4.37 Ω cm<sup>2</sup> (4.14 Ω cm<sup>2</sup>) and 4.17 Ω cm<sup>2</sup> (3.97 Ω cm<sup>2</sup>) respectively. The change in the R<sub>SH</sub> and R<sub>SER</sub> affect the FF of the devices (from 68.14% (66.51%) to 69.05% (71.37%)). The shadow mask eliminates any electrical contribution from the neighbour to the measured solar cell. To measure the J<sub>sc</sub> accurately for these devices, external quantum

efficiency (EQE) measurements were carried out. The EQE achieved a maximum absorbance of 77% leading to an integrated  $J_{SC}$  of  $17.22 \text{ mAcm}^{-2}$  as shown in **Figure 38B**. Further maximum power point tracking (MPPT) of these solar cells were carried out under continuous illumination. The tracking was carried out for 8 min. The values for  $J_{MPP}$  and PCE are shown in **Figure 38C-D**. The MPPT suggest that the cells have a consistent PCE of 12.2%. Further the  $\text{Cs:NiO}_x$  based cells were dip coated with R-BPA molecules.

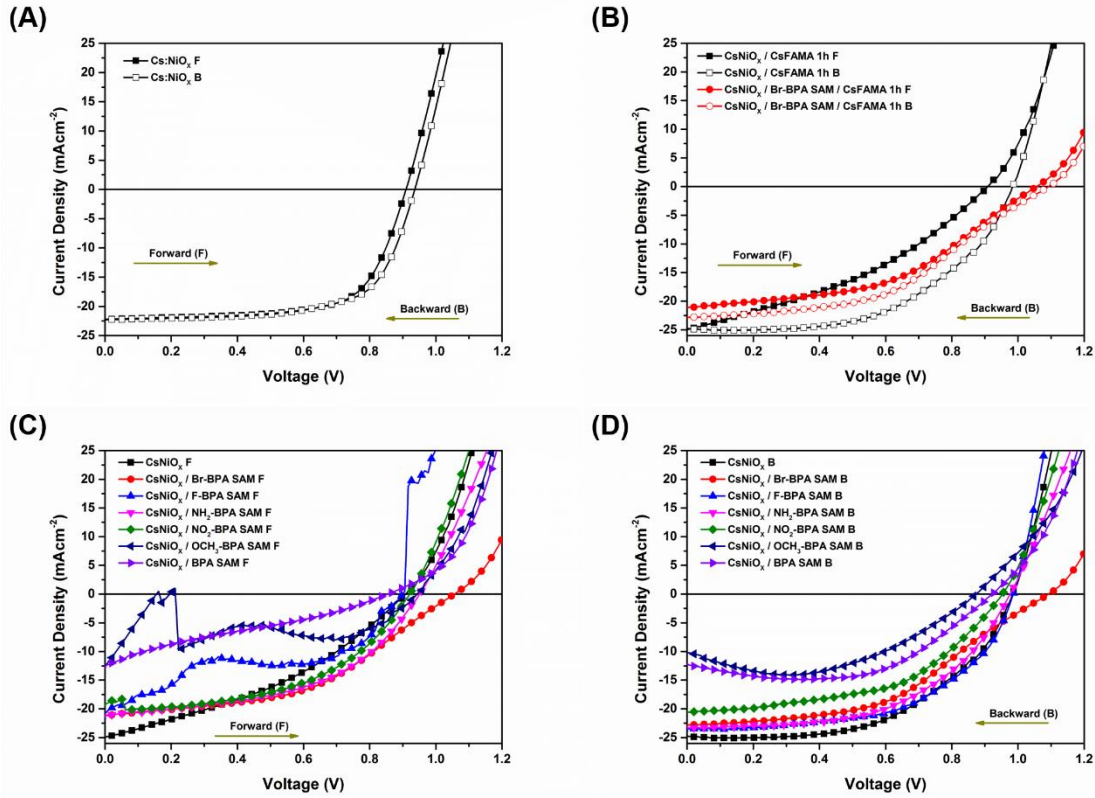


**Figure 39:** JV curve for (A)  $\text{Cs:NiO}_x/\text{CsFAMA}$  perovskite solar cells and (B-D) solar cells with R-BPA molecules deposited on  $\text{Cs:NiO}_x$  thin films.

**Table 14:**  $V_{OC}$ , absolute  $J_{SC}$ , FF, and PCE values of  $\text{Cs:NiO}_x$  and  $\text{CsFAMA}$  based solar cells. The values are listed in forward (backward) sweep directions.

| $0.09 \text{ cm}^2$ | $V_{OC}$ (V)  | $J_{SC}$ ( $\text{mAcm}^{-2}$ ) | FF (%)        | PCE (%)       |
|---------------------|---------------|---------------------------------|---------------|---------------|
| $\text{Cs:NiO}_x$   | 0.906 (0.937) | 22.21 (22.30)                   | 68.12 (66.68) | 13.64 (13.86) |

|                 |                              |                            |                            |                            |
|-----------------|------------------------------|----------------------------|----------------------------|----------------------------|
| Mean (20 cells) | 0.910±0.017<br>(0.936±0.021) | 21.82±1.12<br>(22.51±0.96) | 59.20±6.47<br>(59.06±3.75) | 11.65±1.27<br>(12.35±0.76) |
|-----------------|------------------------------|----------------------------|----------------------------|----------------------------|

The **Figure 39A** shows the illuminated JV curves for the champion Cs:NiO<sub>x</sub> based CsFAMA perovskite solar cells. The V<sub>OC</sub>, absolute J<sub>SC</sub>, FF and PCE of the champion cells along with the mean values for 20 cells are listed in **Table 14**. The cells performed similar to the solar cells with NiO<sub>x</sub> nanoparticles based films. However, the V<sub>OC</sub> of these devices were lower in comparison to the nanoparticles based films.

**Table 15:** V<sub>OC</sub>, absolute J<sub>SC</sub>, FF, and PCE values for light measurements of Cs:NiO<sub>x</sub> based solar cells with R-BPA SAM functionalization by dip coating. The values are listed in forward (backward) sweep directions.

| <i>0.09 cm<sup>2</sup></i> | <i>V<sub>OC</sub> (V)</i> | <i>J<sub>SC</sub> (mAcm<sup>-2</sup>)</i> | <i>FF (%)</i> | <i>PCE (%)</i> |
|----------------------------|---------------------------|---|---------------|----------------|
| Cs:NiO <sub>x</sub>        | 0.906 (0.987)             | 24.92 (24.76)                             | 36.50 (54.43) | 8.26 (13.29)   |
| Br-BPA SAM                 | 1.057 (1.087)             | 21.11 (22.83)                             | 45.74 (45.83) | 10.09 (11.24)  |
| F-BPA SAM                  | 0.896 (0.987)             | 20.77 (23.45)                             | 41.37 (56.18) | 7.71 (12.93)   |
| NH <sub>2</sub> -BPA SAM   | 0.946 (0.977)             | 21.23 (23.29)                             | 49.40 (53.66) | 9.85 (11.95)   |
| NO <sub>2</sub> -BPA SAM   | 0.916 (0.957)             | 19.19 (20.57)                             | 53.13 (51.16) | 9.28 (9.98)    |
| OCH <sub>3</sub> -BPA SAM  | 0.947 (0.997)             | 12.59 (18.79)                             | 47.07 (52.01) | 5.63 (9.74)    |
| BPA SAM                    | 0.856 (0.926)             | 12.48 (12.30)                             | 25.81 (68.08) | 2.74 (7.73)    |

After dip coating R-BPA molecules on the Cs:NiO<sub>x</sub> films, the device performance got worse and irregular JV curves were obtained for the modified samples as seen in **Figure 39B-C**. In a JV curve for solar cells, the absolute J<sub>SC</sub> of the device is the highest current density



obtained, however it was not in the case in these modified results as the current density obtained across the voltage sweep increase in magnitude which is uncharacteristic of solar cells and diodes. This could be due to agglomeration of phosphonic acid molecules on the Cs:NiO<sub>x</sub> surface which would misdirect the dipoles and interfere with the performance of the solar cells. The solar cells based on Cs:NiO<sub>x</sub> films dip coated with Br-BPA molecules were the only cells for which the champion V<sub>OC</sub> observed were comparable to the NiO<sub>x</sub> nanoparticles based Br-BPA modified films as shown in **Table 15**. Therefore, this behaviour from Br-BPA modified cells were further confirmation of the positive effects of the dipole moment of Br-BPA on the performance of solar cells.

### Spin coated R-BPA SAMs

The sol-gel processed Cs:NiO<sub>x</sub> films showed lower V<sub>OC</sub> compared to the NiO<sub>x</sub> nanoparticles based films alongside issues with dip coating of phosphonic acid molecules. Therefore, the possibility of spin coating of R-BPA molecules onto NiO<sub>x</sub> nanoparticles were explored. For this study Br-BPA, NH<sub>2</sub>-BPA, and BPA molecules were chosen because Br-BPA (2.3 D) showed consistent performance and to spread out the dipole moment NH<sub>2</sub>-BPA (-0.9 D) and BPA (0.4 D) molecules were chosen. The R-BPA molecules were dynamically spin coated onto the NiO<sub>x</sub> films in the glovebox and the CsFAMA perovskites were annealed for 1 h.

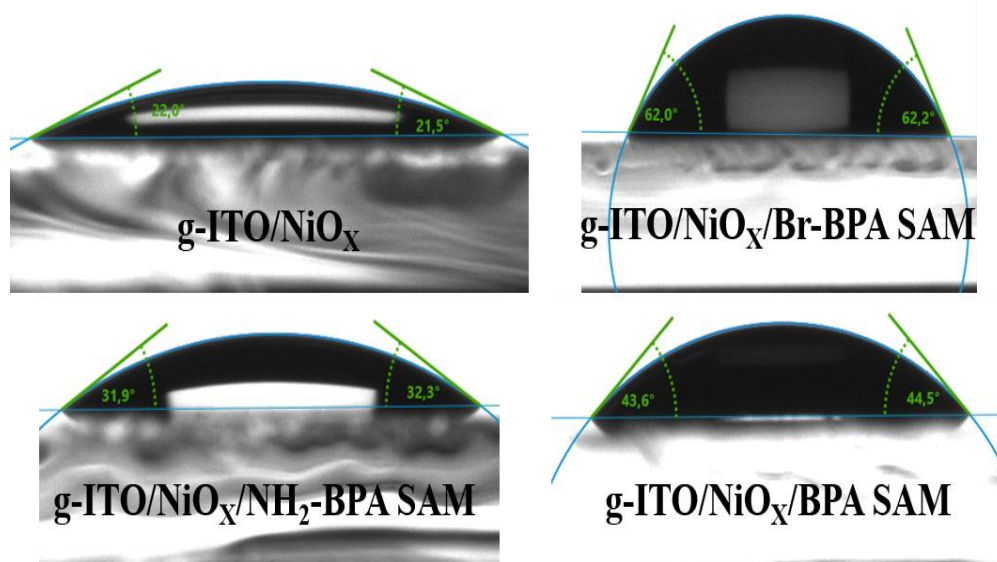


**Figure 40:** Images of water drops on NiO<sub>x</sub> nanoparticles based thin films modified by spin coated R-BPA molecules.

The NiO<sub>x</sub> nanoparticles based thin films used were same as used in dip coated R-BPA experiments and therefore, the XRD and UV-Vis transmission spectra for these films were can be observed in **Figure 28**.

The modification of the NiO<sub>x</sub> surface by R-BPA (Br-BPA, NH<sub>2</sub>-BPA and BPA) molecules through spin coating was confirmed by performing contact angle measurements. The measured values are listed in the **Table 16** and the images of water drops can be seen in **Figure 40**.

Similar to dip coated results, Br-BPA modified NiO<sub>x</sub> thin films showed the highest observed change ( $65.2 \pm 0.7^\circ$ ) compared to the other samples without ( $27.1 \pm 0.7^\circ$ ) and with NH<sub>2</sub>-BPA ( $32.4 \pm 0.5^\circ$ ) and BPA ( $47.7 \pm 0.5^\circ$ ) modified NiO<sub>x</sub> thin films. These results indicate successful modification of the NiO<sub>x</sub> thin films through spin coating R-BPA molecules.

**Table 16:** Contact angles (CAs) of water measured on NiO<sub>x</sub> nanoparticles based thin films modified by spin coated R-BPA molecules.

|        | <i>NiO<sub>x</sub></i> | <i>NiO<sub>x</sub>/Br-BPA</i> | <i>NiO<sub>x</sub>/NH<sub>2</sub>-BPA<br/>SAM</i> | <i>NiO<sub>x</sub>/BPA</i> |
|--------|------------------------|-------------------------------|---|----------------------------|
| CA (°) | $27.1 \pm 0.7$         | $65.2 \pm 0.7$                | $32.4 \pm 0.5$                                    | $47.7 \pm 0.5$             |

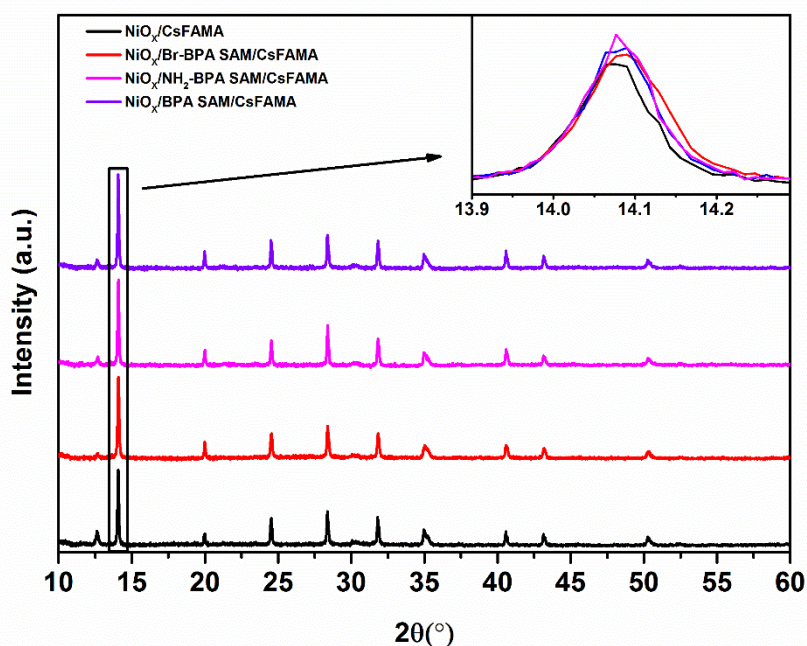


**Figure 41:** XRD reflexes for CsFAMA perovskites deposited on NiO<sub>x</sub> nanoparticles based thin films modified by spin coating R-BPA solution.

The CsFAMA based perovskite absorber layer was prepared similar to previous chapter. However in this case the perovskite thin films were annealed for 1 h compared to the usual 1 h. The XRD reflexes for these samples without and with R-BPA modification can be seen **Figure 41A**. The XRD reflexes for CsFAMA perovskites on NiO<sub>x</sub> nanoparticles based thin film showed prominent perovskite peaks at  $2\theta$  equals  $14.08^\circ$  and  $28.36^\circ$  for (110) and (220) lattice planes respectively [22,23]. The  $2\theta$  values for Br-BPA, NH<sub>2</sub>-BPA and BPA molecules modified samples were similar to the non-modified samples as shown in **Table 17**. The slight changes can be attributed to lattice strain.

**Table 17:** XRD reflexes for (110) and (220) lattice planes in CsFAMA perovskites on NiO<sub>x</sub> nanoparticles based thin films which were modified by spin coating R-BPA molecules.

|       | <i>CsFAMA</i> | <i>Br-BPA</i> | <i>NH<sub>2</sub>-BPA</i> | <i>BPA</i> |
|-------|---------------|---------------|---------------------------|------------|
| (110) | 14.08         | 14.09         | 14.09                     | 14.08      |
| (220) | 28.36         | 28.39         | 28.38                     | 28.39      |

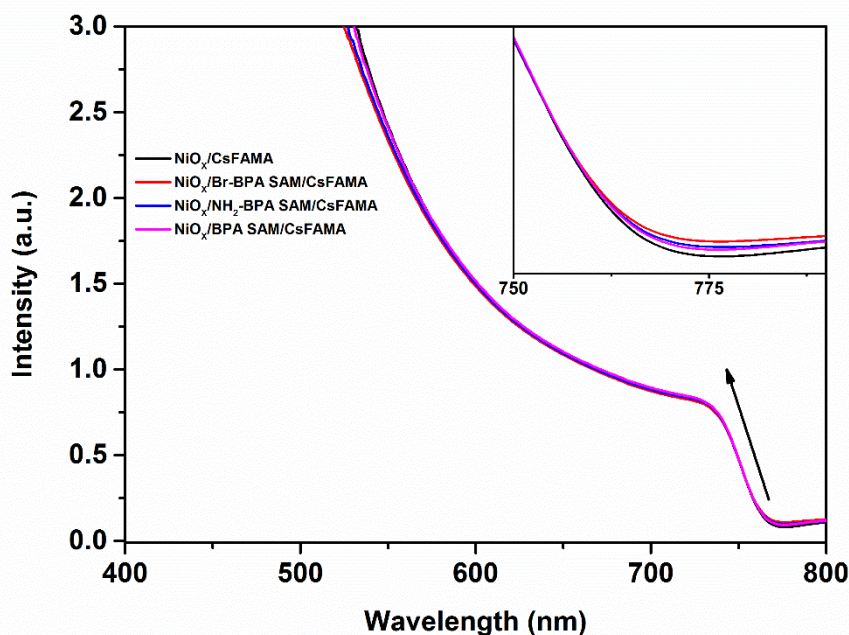


**Figure 42:** UV-Vis absorption spectra for CsFAMA perovskites deposited on NiO<sub>x</sub> nanoparticles based thin films modified by spin coating R-BPA solution.

The UV-Vis spectra observed in **Figure 41B** show an absorbance onset at ~770 nm which is similar to the dip coated samples. However, the absorbance shown for spin coated samples are for 300-325 nm thick CsFAMA layers. Since the thicknesses are within range to each other therefore, the behaviour is similar.

In **Figure 43**, the top view SEM images for CsFAMA perovskite layers on without and with modified NiO<sub>x</sub> thin films show homogeneous grain distribution. The mean grain size for five random points on the images are  $440.87 \pm 59.10$  nm,  $529 \pm 107.11$  nm,  $570.09 \pm 213.90$  nm and  $417.38 \pm 63.98$  nm for non-modified and Br-BPA, NH<sub>2</sub>-BPA and BPA molecule modified samples respectively. These grain sizes were smaller in comparison to dip coated samples as seen in **Figure 32**. The large standard deviations for Br-BPA and NH<sub>2</sub>-BPA based samples suggest irregular size distribution with patches of large grains and small grains spread across the surface. The presence of large grains on the surface was partly supported by the cross section SEM images as seen in **Figure 44**. The non-modified samples have significantly more grain boundaries along the thickness of the film in vertical and horizontal directions compared to the others where the boundaries are mainly vertical. This suggests that the non-modified samples have relatively more grains compared to the modified samples.

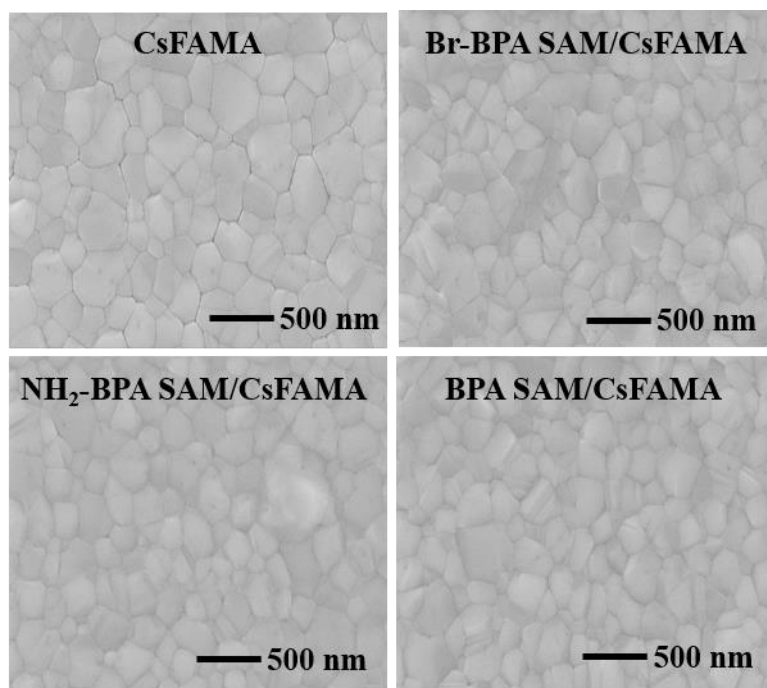


**Figure 43:** Top view SEM images for CsFAMA perovskite on non-modified and Br-BPA, NH<sub>2</sub>-BPA and BPA molecules modified NiO<sub>x</sub> thin films. The modification was done using spin coating.

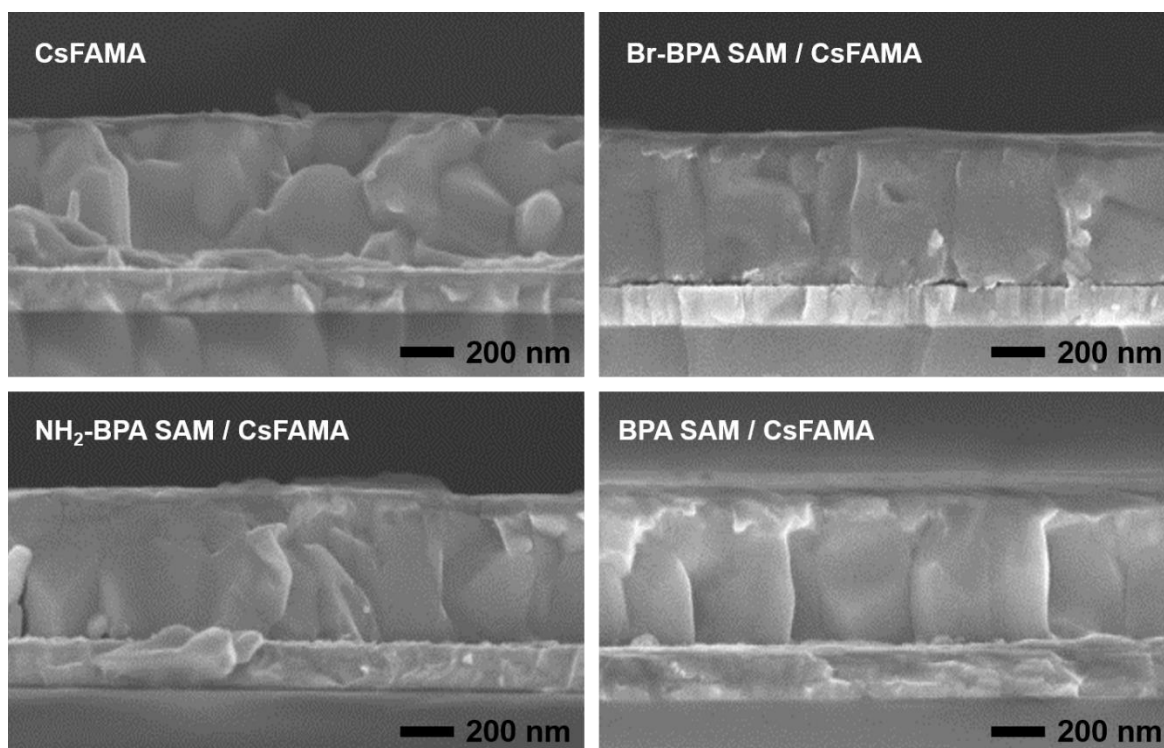


**Figure 44:** Cross sectional SEM images for ITO/NiO<sub>x</sub>/ without and with R-BPA/CsFAMA/PC<sub>60</sub>ABM substrates for spin coated R-BPA molecules on NiO<sub>x</sub> thin films.

Similarly, the images suggest that NH<sub>2</sub>-BPA molecules based CsFAMA films have large crystals compared to the non-modified and Br-BPA molecules based samples. The continuous grains from across the thickness is helpful for charge extraction as the charges do not encounter grain boundaries and therefore are less prone to grain boundary recombination.

Evidently, the phosphonic acid molecules has affected the crystallization of the CsFAMA perovskites. The change is observed in the reduction of grain boundaries across the thin film as seen in **Figure 44**. The large grains observed for NH<sub>2</sub>-BPA molecules based sample suggest a possible interaction between the NH<sub>2</sub>- group of the molecule and the formamidinium ion from the perovskite. However, this hypothesis has to be further investigated.

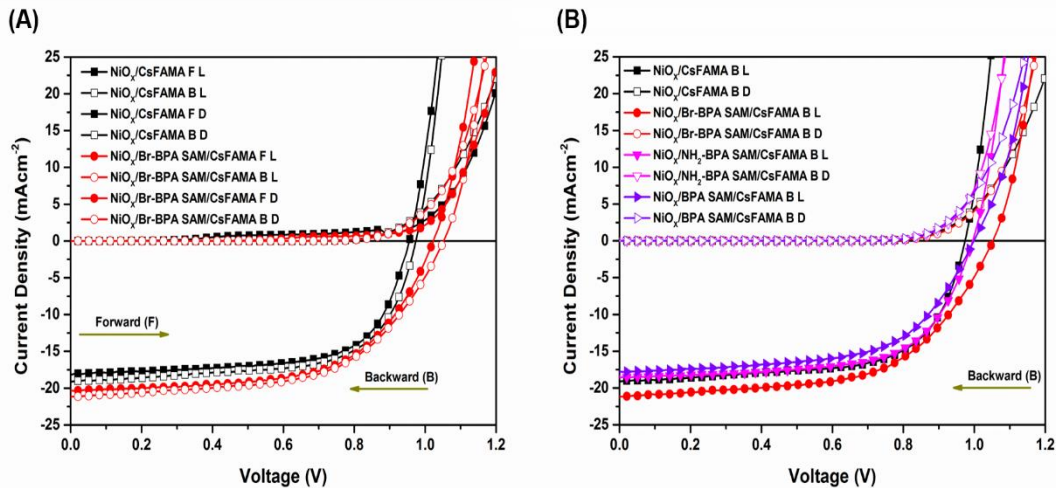


**Figure 45:** JV curves for spin coated R-BPA molecules on NiO<sub>x</sub> nanoparticles based thin films and 1 h annealed CsFAMA perovskite. **(A)** Comparison of non-modified and Br-BPA molecules based cells and **(B)** backward curves for non-modified, Br-BPA, NH<sub>2</sub>-BPA and BPA modified solar cells.

**Figure 45** shows the JV curves for the dynamically spin coated R-BPA SAM based solar cells, and the  $V_{OC}$ ,  $J_{SC}$ , FF, and PCEs are listed in **Table 18**. Consistent with the earlier results for Br-BPA, the  $V_{OC}$  improved from 0.957 V (0.977 V) to 1.027 V (1.057 V) in comparison to non-modified solar cells. The devices also showed improved  $J_{SC}$  and the values were supported by the EQE and integrated  $J_{SC}$  (**Figure 46B**). The  $R_{SER}$  and  $R_{SH}$  observed for non-modified solar cells were 5.06  $\Omega$  cm<sup>2</sup> (4.41  $\Omega$  cm<sup>2</sup>) and 155.28  $\Omega$  cm<sup>2</sup> (505.05  $\Omega$  cm<sup>2</sup>) respectively. Similarly the  $R_{SER}$  values for Br-BPA, NH<sub>2</sub>-BPA and BPA

modified solar cells were calculated to be  $7.78 \Omega \text{ cm}^2$  ( $8.74 \Omega \text{ cm}^2$ ),  $5.22 \Omega \text{ cm}^2$  ( $6.13 \Omega \text{ cm}^2$ ) and  $8.22 \Omega \text{ cm}^2$  ( $10.29 \Omega \text{ cm}^2$ ) respectively and the  $R_{SH}$  values were  $787.40 \Omega \text{ cm}^2$  ( $497.51 \Omega \text{ cm}^2$ ),  $310.55 \Omega \text{ cm}^2$  ( $349.65 \Omega \text{ cm}^2$ ) and  $200.80 \Omega \text{ cm}^2$  ( $909.09 \Omega \text{ cm}^2$ ) respectively.

The  $V_{OC}$ s for  $\text{NH}_2$ -BPA and BPA SAM based solar cells showed slight improvement over the non-modified cells. However, the  $J_{SC}$  for BPA SAM based cells were significantly lower than Br-BPA SAM and slightly non-modified cells. The MPPT for the devices suggested stable performance for 10 min as shown in **Figure 46A**.

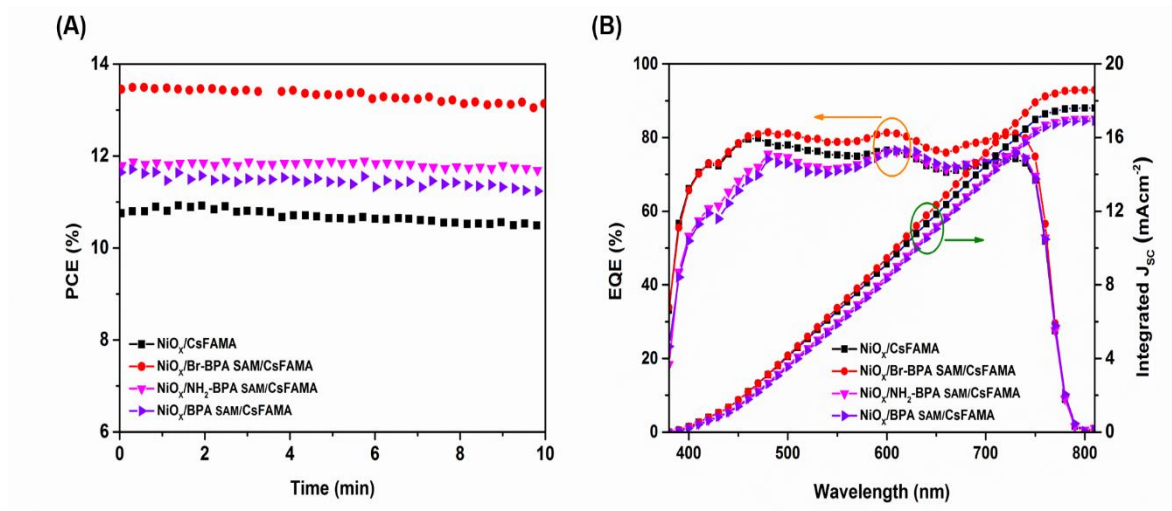


**Figure 46:** (A) MPPT of PCE and (B) EQE and integrated  $J_{SC}$  for spin coated R-BPA molecules on  $\text{NiO}_x$  nanoparticles based thin films and 1 h annealed CsFAMA.

**Table 18:**  $V_{OC}$ , absolute  $J_{SC}$ , FF, and PCE values for light measurements of the  $\text{NiO}_x$  nanoparticles based solar cells with BPA SAM, Br-BPA SAM, and  $\text{NH}_2$ -BPA SAM. The SAMs were deposited using dynamic spin coating and the CsFAMA perovskites were annealed for 1 h at  $100^\circ\text{C}$ . The values are listed in forward (backward) sweep directions.

| $0.0702 \text{ cm}^2$        | $V_{OC}$ (V)     | $J_{SC}$ ( $\text{mAcm}^{-2}$ ) | <i>Integrated</i>               |                  |                  |
|------------------------------|------------------|---------------------------------|---------------------------------|------------------|------------------|
|                              |                  |                                 | $J_{SC}$ ( $\text{mAcm}^{-2}$ ) | FF (%)           | PCE (%)          |
| $\text{NiO}_x/\text{CsFAMA}$ | 0.957<br>(0.977) | 18.16 (19.09)                   | 17.64                           | 66.48<br>(64.38) | 11.32<br>(11.86) |

|                      |         |               |       |         |         |
|----------------------|---------|---------------|-------|---------|---------|
| Br-BPA               | 1.027   | 20.33 (21.15) | 18.62 | 60.43   | 12.43   |
| SAM/CsFAMA           | (1.057) |               |       | (57.83) | (12.79) |
| NH <sub>2</sub> -BPA | 0.987   | 18.28 (18.56) | 17.08 | 66.23   | 11.91   |
| SAM/CsFAMA           | (0.997) |               |       | (64.10) | (11.79) |
| BPA                  | 0.997   | 16.15 (17.77) | 16.93 | 61.59   | 9.85    |
| SAM/CsFAMA           | (0.997) |               |       | (60.32) | (10.61) |

## Conclusion

In conclusion this chapter shows a successful modification of NiO<sub>x</sub> films prepared through solution processing routes which include nanoparticle synthesis and sol-gel route. The modification of the NiO<sub>x</sub> nanoparticles based films were primarily carried out by dip coating phosphonic acid molecules on the films. The chosen molecules were Br-BPA, F-BPA, NH<sub>2</sub>-BPA, NO<sub>2</sub>-BPA, OCH<sub>3</sub>-BPA, and BPA due to their dipole moments. In comparison to dip coating, this work also includes modification of NiO<sub>x</sub> films through spin coating the R-BPA molecules onto its surface. The successful modifications through different methods were confirmed through contact angle measurements. The presence of Br-BPA molecules on the surface showed the maximum change in the contact angle of water compared to the other phosphonic acid molecules.

The presence of the R-BPA SAMs at the NiO<sub>x</sub>/CsFAMA interface did not significantly affect the absorption properties of the perovskite. However, the morphology of the perovskite observed changes in the grain size. In case of dip coated samples, NO<sub>2</sub>-BPA and OCH<sub>3</sub>-BPA based samples showed large standard deviations in the grain size compared to others. Similarly, spin coated samples also indicated impact on grain sizes due to the phosphonic acid molecules. The presence of R-BPA SAM at the NiO<sub>x</sub>/CsFAMA interface possibly reduced the number of grains.

The JV curves for dip coated Br-BPA and F-BPA molecules based solar cells showed significant change in the V<sub>OC</sub> of the devices compared to non-modified cells. The presence



of F-BPA molecules improved the  $V_{OC}$  to  $\sim 1.087$  V compared to 1.007 V and 0.967 V for Br-BPA and non-modified solar cells. This improvement can be assigned to the dipole effect of these molecules on the performance of the solar cells. However, for consistent performance of these devices the optimization of  $NiO_x$  thin film quality is critical. However, when compared to sol-gel processed Cs: $NiO_x$  films, the performance of  $NiO_x$  nanoparticles based films had higher  $V_{OCs}$  for non-modified samples.

The JV curves for spin coated Br-BPA molecules had similar results compared to dip coated Br-BPA based solar cells. Solar cells with  $V_{OCs}$  of 1.057 V were observed compared to non-modified solar cells with 0.977 V. The devices showed consistent performance in MPPT.

Throughout the experiments and variations, Br-BPA modification either with dip coating or spin coating performed consistently by achieving improved  $V_{OCs}$ . The improvement can be attributed to the free standing gas phase dipole moment of the molecule (2.3 D). The presence of Br-BPA molecules at the  $NiO_x$ /CsFAMA interface increased the grain sizes across the cross section of the layer by reducing horizontal grains. Less grain boundaries are essential for charge extraction and lowering of charge recombinations. The dipole also affects the band bending of the valence band of  $NiO_x$  and perovskite in such a way that charge extraction improves and higher  $V_{OCs}$  can be obtained.

## References

1. I. Lange, S. Reiter, M. Pätzelt, A. Zykov, A. Nefedov, J. Hildebrandt, S. Hecht, S. Kowarik, C. Wöll, G. Heimel, D. Neher, *Adv. Funct. Mater.* **24**, 7014 (2014)
2. S. Rühle, M. Greenshtein, S.-G. Chen, A. Merson, H. Pizem, C.S. Sukenik, D. Cahen, A. Zaban, *J. Phys. Chem. B* **109**, 18907 (2005)
3. F. Abraham, Fluorinated Benzylphosphonic Acid Derivatives for Work Function Modification, Durham thesis, Durham University (2014). <http://etheses.dur.ac.uk/10622/>
4. S.A. Paniagua, A.J. Giordano, O'Neil L. Smith, S. Barlow, H. Li, N.R. Armstrong, J.E. Pemberton, J.-L. Brédas, D. Ginger, S.R. Marder, *Chem. Rev.* **2016**, *116* (12), 7117-7158
5. I. Lange, S. Reiter, J. Kniepert, F. Piersimoni, M. Pätzelt, J. Hildebrandt, T. Brenner, S. Hecht, D. Neher, *Appl. Phys. Lett.* **106**, 113302 (2015)
6. C. Wood, H. Li, P. Winget, J.-L. Brédas, *J. Phys. Chem. C* **116**, 19125-19133 (2012)
7. F. Jiang, W.C.H. Choy, X. Li, D. Zhang, J. Cheng, *Adv. Mater.* **27**, 2930 (2015)
8. X. He, Y. Bai, H. Chen, X. Zheng, S. Yang, *Electronics and Photonics* **1**, 3175 (2016)
9. A. Abrusci, S.D. Stranks, P. Docampo, H.L. Yip, A.K. Jen, H.J. Snaith, *Nano Lett.* **13**, 3124 (2013)
10. L. Zuo, Z. Gu, T. Ye, W. Fu, G. Wu, H. Li, H. Chen, *J. Am. Chem. Soc.* **137**, 2674 (2015)
11. L. Yang, G. Chen, Y. Sun, D. Han, S. Yang, M. Gao, P. Zou, H. Luan, X. Kong, J. Yang, *Electrochimica Acta* **164**, 38 (2015)
12. Q. Wang, C.-C. Chueh, T. Zhao, J. Cheng, M. Eslamian, W.C.H. Choy, A.K.-Y. Jen, *ChemSusChem* **10**, 3794 (2017)
13. P. Zhao, B.J. Kim, H.S. Jung, *Materials Today Energy* **7**, 267 (2018)
14. Z. Zhang, J.T. Yates Jr., *Chem. Rev.* **112**, 5520 (2012)
15. C. Goh, S.R. Scully, M.D. McGehee, *J. App. Phys.* **101**, 114503 (2007)
16. O.T. Hofmann, P. Rinke, *Adv. Electron. Mater.* **3**, 1600373 (2017)
17. S. Weber, T. Rath, J. Mangalam, B. Kunert, A.M. Coclite, M. Bauch, T. Dimopoulos, G. Trimmel, *J. Mater. Sci: Mater. Electron.* **29**, 1847 (2018)
18. H. Zhang, J. Cheng, F. Lin, H. He, J. Mao, K.S. Wong, A.K.-Y. Jen, W.C.H. Choy, *ACS Nano* **10**, 1503 (2016)
19. F. Jiang, W.C.H. Choy, X. Li, D. Zhang, J. Cheng, *Adv. Mater.* **27**, 2930 (2015)
20. X. Yin, P. Chen, M. Que, Y. Xing, W. Que, C. Niu, J. Shao, *ACS Nano* **10**, 3630 (2016)

21. W. Chen, F.-Z. Liu, X.-Y. Feng, A.B. Djurišić, W.K. Chan, Z.-B. He, *Adv. Energy Mater.* **7**, 1700722 (2017)
22. T. Singh, T. Miyasaka, *Adv. Energy Mater.* **8**, 1700677 (2018)
23. M. Saliba, T. Matsui, J.-Y. Seo, K. Domanski, J.-P. C.-Baena, M. K. Nazeeruddin, S. M. Zakeeruddin, W. Tress, A. Abate, A. Hagfeldt, M. Grätzel, *Energy Environ. Sci.* **9**, 1989 (2016)
24. X. Guo, C. McCleese, C. Kolodziej, A.C.S. Samia, Y. Zhao, C. Burda, *Dalton Trans.* **45**, 3806 (2016)



## Chapter 5: Conclusion and Outlook

---

*In literature and in life we ultimately pursue, not conclusion but beginnings...*

- Sam Tanenhaus

## Conclusion

**Chapter 1: An Introduction to Perovskite materials and basics of Solar cells** reports on the origin and properties of perovskite materials favourable for solar cells applications [1-4]. The ability to vary the composition in the crystal structure allows further optimization of optical properties of perovskites (example bandgap) [5-19]. As mentioned previously, perovskites have low trap density and electron-hole diffusion lengths above 100  $\mu\text{m}$  allowing efficient charge collection [2-4]. To further build efficient solar cells, fabricating solar cells with the optimal composition from variety of transparent conducting oxides, hole transport layers, perovskite absorber layer composition, electron transport layers, and metal back electrodes is vital. Therefore, the chapter covers the introduction to different solar cell architectures and the corresponding components. The state of the art for lead halide perovskite solar cells covers the currently available highest PCEs for n-i-p architecture and p-i-n architecture based cells [20-24]. Further the chapter discusses hysteresis observed in lead perovskite solar cells and issues related to the toxicity of lead. Lastly, the chapter ends with refreshing the basics of solar cells and the working principles.

**Chapter 2: Influence of different layers on the performance of solar cells in n-i-p architecture** encapsulates the fabrication of n-i-p architecture based lead perovskite solar cells and the irreproducible nature of these devices owing to strict requirements of fabrication process. The chapter studies the variation of cesium content in the perovskite composition, different TCOs (ITO and FTO) and HTLs (spiro-OMeTAD and PTAA). However the PCEs obtained range between 0 – 13% and have really low sample size for each variation indicating poor reproduction. The chapter concludes by attempting the prescribed methodology to produce 20% and higher efficient lead perovskite solar cells by Saliba et al. [25]. However the average PCEs obtained for these cells were < 2%. Therefore, the chapter strongly hints the importance and need of optimizing the fabrication process and the delicate yet meticulous requirements of lead perovskites to achieve highly efficient solar cells.

In **Chapter 3: Modification of NiO<sub>x</sub> hole transport layers with 4-bromobenzylphosphonic acid and its influence on the performance of lead halide perovskite solar cells** shows successful functionalization of solution processed NiO<sub>x</sub> HTLs by a dip coating procedure using a Br-BPA solution in acetonitrile. This is substantiated by the markedly increased contact angle of water, the surface free energies and the detection of

P 2p and Br 3p peaks in the modified sample by XPS measurements. No notable change in the optical properties and surface morphology of the perovskite layers were observed. However, the JV curves reflect improved photovoltaic performance, particularly an increased  $V_{OC}$ . A typical device shows an improved PCE from 11.2% (10.8%) to 12.5% (12.7%) due to an improved  $V_{OC}$  from 0.978 V (0.978 V) to 1.019 V (1.029 V) in fwd (bwd) scan directions, respectively. The improvement in the  $V_{OC}$  is assumed to be largely due to the realignment of the energy levels based on the dipole moment of the Br-BPA SAM molecules. With devices having Br-BPA modifications,  $V_{OC}$ s of up to 1.099 V could be obtained. Furthermore, MPP tracking measurements revealed a steady state PCE of 11.35% and 12.22% for typical devices without and with Br-BPA modified  $NiO_x$  films.

This chapter was published in the Journal of Materials Science: Materials in Electronics (DOI: 10.1007/s10854-019-01294-0) [26]. Reproduced with permission from Springer Nature.

**Chapter 4: Benzyl phosphonic acid SAMs in p-i-n architecture** reports on the background and extended work done supporting the previous chapter. This chapter covers the modification of  $NiO_x$  and perovskite interface with phosphonic acid based molecules which include Br-BPA, F-BPA,  $NH_2$ -BPA,  $NO_2$ -BPA,  $OCH_3$ -BPA and BPA molecules through dip coating and spin coating methods. The presence of these molecules change the surface properties of  $NiO_x$  due to their individual dipoles [27,28]. When the dipole of a molecule is directed towards or away from the  $NiO_x$  surface at the  $NiO_x$  and perovskite interface, it causes shift in the energy levels of  $NiO_x$  and perovskite. Br-BPA, F-BPA, and  $NO_2$ -BPA molecules when form SAM at the interface and their dipole is directed towards  $NiO_x$  layer, the gap between the valence band of  $NiO_x$  and perovskite reduce [29,30]. This affects the  $V_{OC}$  of the device. Similarly, the dipole of  $NH_2$ -BPA,  $OCH_3$ -BPA and BPA molecules based SAM is directed away from  $NiO_x$  and in turn increases the gap between the energy levels of  $NiO_x$  and perovskite.

The modifications were confirmed through measuring the contact angles of the water droplets on the non-modified and modified  $NiO_x$  films. The contact angles for Br-BPA modified  $NiO_x$  surfaces showed maximum change in the contact angles for all the variations studied. The presence of R-BPA SAM molecules showed slight variations in the morphology of the perovskite films. In case of dip coated method, the grain sizes for Br-BPA, F-BPA,  $NH_2$ -BPA, and BPA molecules have a clear increase compared to non-modified samples.

The size distribution for these samples range between 600 nm to 800 nm. However, NO<sub>2</sub>-BPA and OCH<sub>3</sub>-BPA based samples have smaller grains in the top view images. The size distribution range between 400 nm to 800 nm. In case of spin coated method, the relative size (mean) of the grains are lesser than dip coated samples at the surface of the films. The cross section images of these samples suggested reduced grain boundaries across the thickness of the films for the modified samples. The reduced grain boundaries would lead to reduced grain boundary recombination as the charge diffusion length increases.

For NiO<sub>x</sub> nanoparticles based films modified by dip coating the phosphonic acid molecules, the Br-BPA and F-BPA modified films showed improved V<sub>OCs</sub> up to 1.057 V from 0.977 V. However when faced with inconsistencies and further need to optimize the thin film quality, the improvement in the Br-BPA molecules showed consistent improvement in the V<sub>OC</sub> of the devices compared to non-modified films and the other modifications. For spin coated phosphonic acid molecules based cells, the modifications were successful and the Br-BPA molecule based cells again had the most improvement. The reason for the improvement can be attributed to the gas phase dipole moment of the molecule (Br-BPA, 2.3 D) [27]. The dipole affects the band alignment as mentioned previously [31].

The chapter successfully shows modification of NiO<sub>x</sub> and perovskite interface through two different deposition methods. The solar cells with Br-BPA SAM show consistent and significant improvement in the photovoltaic properties.

## **Outlook: Future and alternatives**

To achieve highly efficient lead perovskite based solar cells, it is critical to scrutinize, investigate and optimize the solar cell fabrication process and particularly the perovskite thin film deposition. Once these steps are understood and the necessary skill step is achieved, highly efficient perovskite solar cells are possible to fabricate. This is important for both the architectures: n-i-p and p-i-n. Research have shown that NiO<sub>x</sub> has the potential to be manipulated and optimized to achieve over 20% power conversion efficiency. Therefore with careful management of NiO<sub>x</sub> and NiO<sub>x</sub>/perovskite interface using appropriate positively influencing supplements fabrication of highly efficient devices can be possible. Towards this goal, self assembled monolayers with different functional groups and anchor groups can be effectively explored. In efforts to build on the research done in this thesis in the p-i-n



architecture using NiO<sub>x</sub> and R-BPA SAMs, more exploration can be held towards understanding different deposition conditions for the R-BPA molecules at their individual level. Different functional groups with phosphonic acid molecules may interact differently with different solvent and in turn guide the self-assembly process. Similarly temperature dependence on the self-assembly process can be explored.

In the light of toxicity issues of lead, alternatives for lead are being enthusiastically researched. The obvious direction being homovalent substitution of lead (Pb<sup>2+</sup>). Therefore, tin (Sn<sup>2+</sup>) and germanium (Ge<sup>2+</sup>) have taken the spotlight [32-39]. To further the attempts diverse compositions of lead-free perovskites with various A-site cations and X-site halides are being perused [40]. However, in comparison to the lead perovskites, lead free perovskites have barely crossed 9% PCEs [41]. In order to achieve higher PCEs of 24.82% by achieving higher J<sub>SC</sub> of ~30 mAcm<sup>-2</sup>, for MASnI<sub>3</sub> with bandgap of 1.3 eV, Mandadapu et al. reported simulation results suggesting that the optimal film thickness must be 0.6 μm. This allows a fill factor of 78% and V<sub>OC</sub> of 1.04 V. However, these results are contingent upon defect free films [40,42,43]. One of the other issues with Sn based perovskites, is the purity of the tin iodide (SnI<sub>2</sub>) precursor. The easy oxidation of Sn<sup>2+</sup> to Sn<sup>4+</sup> has caused trouble in the quality and reproducibility of the tin perovskite solar cells [44-46]. To trim down the possibility of this oxidation tin fluoride (SnF<sub>2</sub>) has been widely used as an additive [47-49]. At present time, it is difficult to say if lead-free perovskite solar cells will come close to the lead perovskites, however, iterative efforts may bring them to equal level [50-55].

## References

1. A. Kojima, K. Teshima, Y. Shirai, T. Miyasaka, *J. Am. Chem. Soc.* **131**, 6050 (2009)
2. Q. Dong, Y. Fang, Y. Shao, P. Mulligan, J. Qiu, L. Cao, J. Huang, *Science* **347**, 967 (2015)
3. D. Shi, V. Adinolfi, R. Comin, M. Yuan, E. Alarousu, A. Buin, Y. Chen, S. Hoogland, A. Rothenberger, K. Katsiev, Y. Losovyj, X. Zhang, P.A. Dowben, O.F. Mohammed, E.H. Sargent, O.M. Bakr, *Science* **347**, 519 (2015)
4. S.D. Stranks, G.E. Eperon, G. Grancini, C. Menelaou, M.J.P. Alcocer, T. Leijtens, L.M. Herz, A. Petrozza, H.J. Snaith, *Science* **342**
5. J.-P.C.-Baena, A. Abate, M. Saliba, W. Tress, T.J. Jacobsson, M. Grätzel, A. Hagfeldt, *Energy Environ. Sci.*, **10**, 710-727 (2017)
6. M. Yavari, M.M.-Ardakani, S. Gholipour, N. Marinova, J.L. Delgado, S.-H.T.-Cruz, K. Domanski, N. Taghavinia, M. Saliba, M. Grätzel, A. Hagfeldt, W. Tress, *Adv. Energy Mater.* **8**, 1702719 (2018)
7. B. Philippe, M. Saliba, J.-P.C.-Baena, U.B. Cappel, S.-H.T.-Cruz, M. Grätzel, A. Hagfeldt, H. Rensmo, *Chem. Mater.* **29**, 3589 (2017)
8. M.I. Dar, M. Franckevičius, N. Arora, K. Redeckas, M. Vengris, V. Gulbinas, S.M. Zakeeruddin, M. Grätzel, *Chem. Phys. Lett.* **683**, 211 (2017)
9. M. Hadadian, J.-P.C.-Baena, E.K. Goharshadi, A. Ummadisingu, J.-Y. Seo, J. Luo, S. Gholipour, S.M. Zakeeruddin, M. Saliba, A. Abate, M. Grätzel, A. Hagfeldt, *Adv. Mater.* **28**, 8681 (2016)
10. A.D. Jodlowski, C.R.-Caremona, G. Grancini, M. Salado, M. Ralaiarisoa, S. Ahmad, N. Koch, L. Camacho, G. de Miguel, M.K. Nazeeruddin, *Nature Energy* **2**, 972 (2017)
11. S.D. Stranks, H.J. Snaith, *Nature Nanotechnology* **10**, 391 (2015)
12. M. Najafi, F.D. Giacomo, D. Zhang, S. Shanmugam, A. Senes, W. Verhees, A. Hadipour, Y. Galagan, T. Aernouts, S. Veenstra, R. Andriessen, *Small* **14**, 1702775 (2018)
13. N.J. Jeon, J.H. Noh, W.S. Yang, Y.C. Kim, S. Ryu, J. Seo, S.I. Seok, *Nature* **517**, 476 (2015)
14. G.E. Eperon, S.D. Stranks, C. Menelaou, M.B. Johnston, L.M. Herz, H.J. Snaith, *Energy Environ. Sci.* **7**, 982 (2014)
15. A. Amat, E. Mosconi, E. Ronca, C. Quarti, P. Umari, M.K. Nazeeruddin, M. Grätzel, F. De Angelis, *Nano Lett.* **14**, 3608 (2014)
16. M. Kulbak, D. Cahen, G. Hodes, *J. Phys. Chem. Lett.* **6**, 2452 (2015)

17. W.S. Yang, B.-W. Park, E.H. Jung, N.J. Jeon, Y.C. Kim, D.U. Lee, S.S. Shin, J. Seo, E.K. Kim, J.H. Noh, S.I. Seok, *Science* **356**, 1376 (2017)
18. M. Saliba, T. Matsui, J.-Y. Seo, K. Domanski, J.-P. C.-Baena, M.K. Nazeeruddin, S.M. Zakeeruddin, W. Tress, A. Abate, A. Hagfeldt, M. Grätzel, *Energy Environ. Sci.* **9**, 1989 (2016)
19. M. Saliba, T. Matsui, K. Domanski, J.-Y. Seo, A. Ummadisingu, S.M. Zakeeruddin, J.-P.C.-Baena, W.R. Tress, A. Abate, A. Hagfeldt, M. Grätzel, *Science* **354**, 206 (2016)
20. M.A. Green, Y. Hishikawa, E.D. Dunlop, D.H. Levi, J.H.-Ebinger, M. Yoshita, A.W.Y.H.-Baillie, *Prog Photovolt Res Appl.* **27**, 3-12 (2019)
21. N.J. Jeon, H. Na, E.H. Jung, T.-Y. Yang, Y.G. Lee, G. Kim, H.-W. Shin, S.I. Seok, J. Lee, J. Seo, *Nature Energy* **3**, 682 (2018)
22. S. Ye, H. Rao, Z. Zhao, L. Zhang, H. Bao, W. Sun, Y. Li, F. Gu, J. Wang, Z. Liu, Z. Bian, C. Huang, *J. Am. Chem. Soc.* **139**, 7504 (2017)
23. W. Chen, Y. Wu, J. Fan, A.B. Djurišić, F. Liu, H.W. Tam, A. Ng, C. Surya, W.K. Chan, D. Wang, Z.-B. He, *Adv. Energy Mater.* **8**, 1703519 (2018)
24. W. Chen, F.-Z. Liu, X.-Y. Feng, A.B. Djurišić, W.K. Chan, Z.-B. He, *Adv. Energy Mater.* **7**, 1700722 (2017)
25. M. Saliba, J.-P.C.-Baena, C.M. Wolff, M. Stollerfoht, N. Phung, S. Albrecht, D. Neher, A. Abate, *Chem. Mater.* **30**, 4193-4201 (2018)
26. J. Mangalam, T. Rath, S. Weber, B. Kunert, T. Dimopoulos, A. Fian, G. Trimmel, *J. Mater Sci: Mater Electron* (2019)
27. I. Lange, S. Reiter, M. Pätzel, A. Zykov, A. Nefedov, J. Hildebrandt, S. Hecht, S. Kowarik, C. Wöll, G. Heimel, D. Neher, *Adv. Funct. Mater.* **24**, 7014 (2014)
28. S. Rühle, M. Greenshtein, S.-G. Chen, A. Merson, H. Pizem, C.S. Sukenik, D. Cahen, A. Zaban, *J. Phys. Chem. B* **109**, 18907 (2005)
29. Q. Wang, C.-C. Chueh, T. Zhao, J. Cheng, M. Eslamian, W.C.H. Choy, A.K.-Y. Jen, *ChemSusChem* **10**, 3794 (2017)
30. C. Goh, S.R. Scully, M.D. McGehee, *J. App. Phys.* **101**, 114503 (2007)
31. Z. Zhang, J.T. Yates Jr., *Chem. Rev.* **112**, 5520 (2012)
32. C.H. Ng, K. Nishimura, N. Ito, K. Hamada, D. Hirotani, Z. Wang, F. Yang, S. Iikubo, Q. Shen, K. Yashino, T. Minemoto, S. Hayase, *Nano Energy* **58**, 130 (2019)
33. N. Ito, M.K. Kamarudin, D. Hirotani, Y. Zhang, Q. Shen, Y. Ogomi, S. Iikubo, T. Minemoto, K. Yoshino, S. Hayase, *J. Phys. Chem. Lett.* **9**, 1682 (2018)

34. I. Kopacic, B. Friesenbichler, S.F. Hoefler, B. Kunert, H. Plank, T. Rath, G. Trimmel, *ACS Appl. Energy Mater.* **1**, 343 (2018)
35. T. Rath, J. Handl, S. Weber, B. Friesenbichler, P. Fürk, L. Troi, T. Dimopoulos, B. Kunert, R. Resel, G. Trimmel, *J. Mater. Chem. A* **7**, 9523 (2019)
36. S. Shao, J. Liu, G. Portale, H.-H. Fang, G.R. Blake, G.H.T. Brink, L.J.A. Koster, M.A. Loi, *Adv. Energy Mater.* **8**, 1702019 (2018)
37. S. Weber, T. Rath, K. Fellner, R. Fischer, R. Resel, B. Kunert, T. Dimopoulos, A. Steinegger, G. Trimmel, *ACS Appl. Energy Mater.* **2**, 539 (2019)
38. T. Krishnamoorthy, H. Ding, C. Yan, W.L. Leong, T. Baikie, Z. Zhang, M. Sherburne, S. Li, M. Asta, N. Mathews, S.G. Mhaisalkar, *J. Mater. Chem. A* **3**, 23829 (2015)
39. L.-J. Chen, *RSC Adv.* **8**, 18396 (2018)
40. W. Ke, C.C. Stoumpos, M.G. Kanatzidis, *Adv. Mater.* 1803230 (2018)
41. E. Jokar, C.-H. Chien, C.-M. Tsai, A. Fathi, E. W.-G. Diao, *Adv. Mater.* 1804835 (2018)
42. U. Mandadapu, S.V. Vedanayakam, K. Thyagarajan, M.R. Reddy, B.J. Babu, *Int. J. Renewable Energy Res.* **7**, 1603 (2017)
43. Q.-Y. Chen, Y. Huang, P.-Ru Huang, T. Ma, C. Cao, Y. He, *Chin. Phys. B* **25**, 027104 (2016)
44. W. Ke, C.C. Stoumpos, I. Spanopoulos, L. Mao, M. Chen, M.R. Wasielewski, M.G. Kanatzidis, *J. Am. Chem. Soc.* **139**, 14800 (2017)
45. Z. Zhu, C.-C. Chueh, N. Li, C. Mao, A. K.-Y. Jen, *Adv. Mater.* **30**, 1703800 (2018)
46. Z. Zhao, F. Gu, Y. Li, W. Sun, S. Ye, H. Rao, Z. Liu, Z. Bian, C. Huang, *Adv. Sci.* **4**, 1700204 (2017)
47. T.-B. Song, T. Yokoyama, C.C. Stoumpos, J. Logsdon, D.H. Cao, M.R. Wasielewski, S. Aramaki, M.G. Kanatzidis, *J. Am. Soc.* **139**, 836 (2017)
48. M.H. Kumar, S. Dharani, W.L. Leong, P.P. Boix, R.R. Prabhakar, T. Baikie, C. Shi, H. Ding, R. Ramesh, M. Asta, M. Grätzel, S.G. Mhaisalkar, N. Mathews, *Adv. Mater.* **26**, 7122 (2014)
49. S. Gupta, D. Cahen, G. Hodes, *J. Phys. Chem. C* **122**, 13926 (2018)
50. S.J. Lee, S.S. Shin, Y.C. Kim, D. Kim, T.K. Ahn, J.H. Noh, J. Seo, S.I. Seok, *J. Am. Chem.* **138**, 3974 (2016)
51. W. Gao, C. Ran, J. Li, H. Dong, B. Jiao, L. Zhang, X. Lan, X. Hou, Z. Wu, *J. Phys. Chem. Lett.* **9**, 6999 (2018)
52. S. Tsarev, A.G. Boldyreva, S.Y. Luchkin, M. Elshobaki, M.I. Afanasov, K.J. Stevenson, P.A. Troshin, *J. Mater. Chem. A* **6** 21389 (2018)

53. X. Liu, Y. Wang, F. Xie, X. Yang, L. Han, ACS Energy Lett. **3** 1116 (2018)
54. W. Liao, D. Zhao, Y. Yu, N. Shrestha, K. Ghimire, C.R. Grice, C. Wang, Y. Xiao, A.J. Cimaroli, R. J. Ellingson, N.J. Podraza, K. Zhu, R.-G. Xiong, Y. Yan, J. Am. Chem. Soc. **138**, 12360 (2016)
55. D.P. McMeekin, G. Sadoughi, W. Rehman, G.E. Eperon, M. Saliba, M.T. Hörantner, A. Haghighirad, N. Sakai, L. Korte, B. Rech, M.B. Johnston, L.M. Herz, H.J. Snaith, Science **351**, 151 (2016)



---

## APPENDIX

---

*Important principles may and must be inflexible...*

- *Abraham Lincoln*

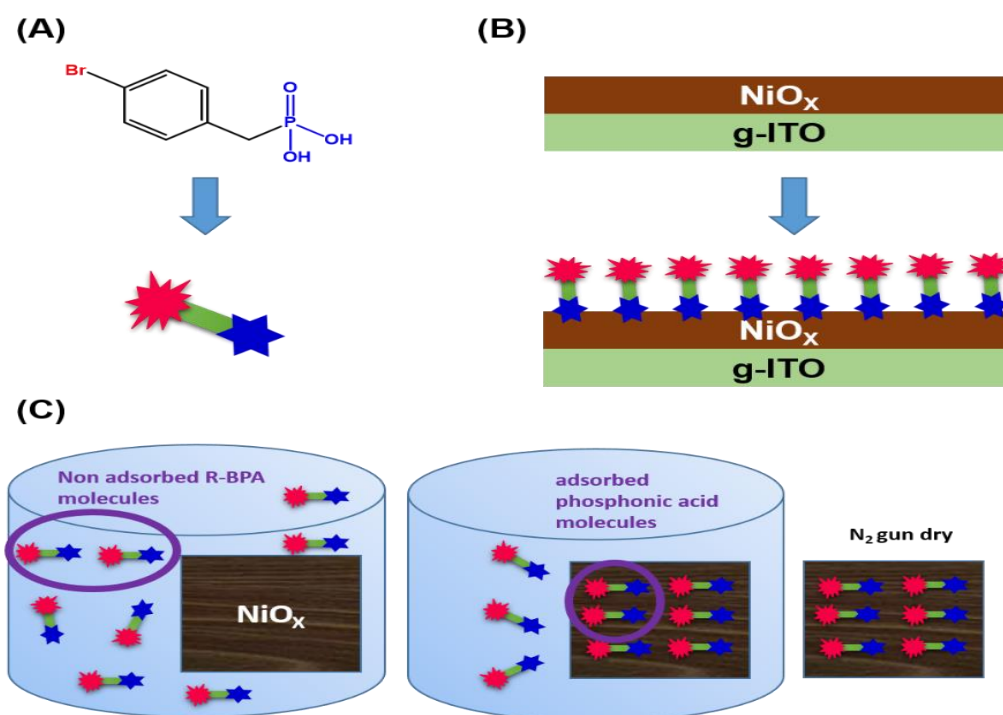


**Figure 47:** (A) Br-BPA molecule and corresponding schematic diagram where the red star indicated the Br group (red in the molecule structure), blue star indicates the phosphonic acid ( $\text{H}_2\text{PO}_3^-$ ) anchor group. (B) 2-D schematic for pre- and post- deposition of the benzylphosphonic acid molecule on g-ITO/ $\text{NiO}_x$  surface. (C) Schematic for dip coating of phosphonic acid molecules on g-ITO/ $\text{NiO}_x$  substrate in a three step process.



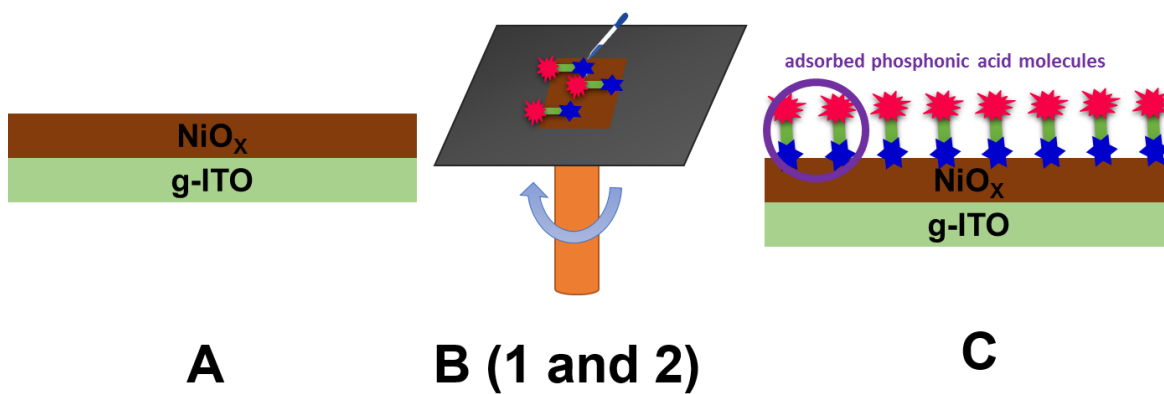


**Figure 48:** spin coating steps for (A) g-ITO/NiO<sub>x</sub> film with (B) R-BPA molecule (1) and rinsing with fresh acetonitrile (2), and (C) R-BPA SAM molecules adsorbed on g-ITO/NiO<sub>x</sub> substrates forming g-ITO/NiO<sub>x</sub>/R-BPA SAM.

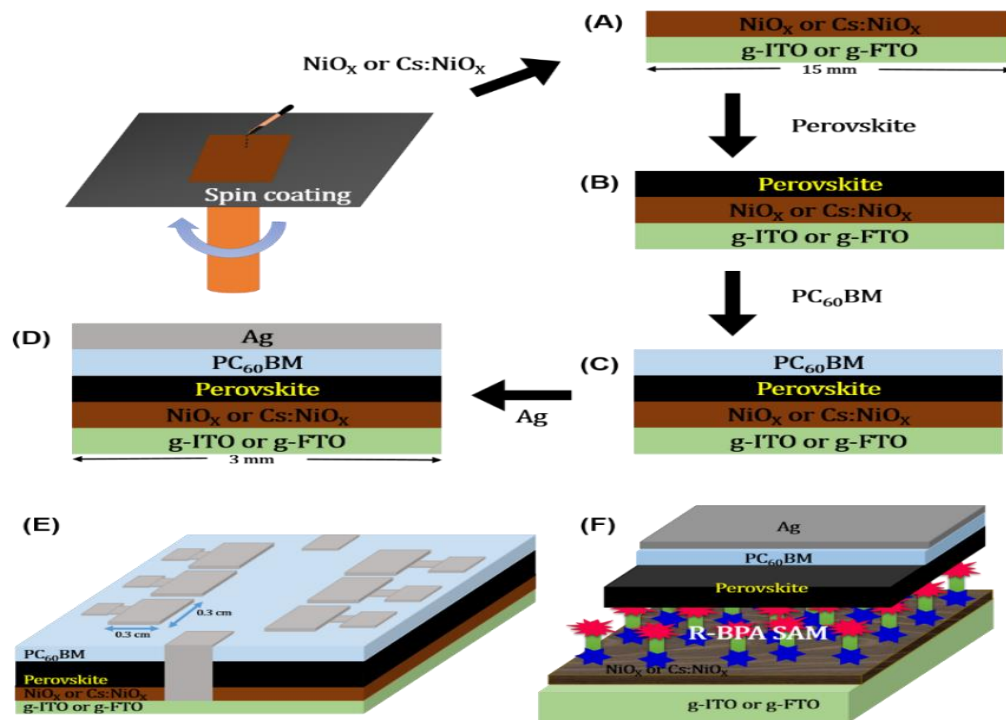


**Figure 49:** Schematic for the sequential spin coating of (A)  $\text{NiO}_x$  or  $\text{Cs:NiO}_x$  layer (B) CsFAMA based triple cation lead halide perovskite (C)  $\text{PC}_{60}\text{BM}$  layer, and thermal deposition of (D) Silver (Ag) on g-ITO substrate. (E) Schematic of a 3-D view of a g-ITO/ $\text{NiO}_x$ /perovskite/ $\text{PC}_{60}\text{BM}$ /Ag based solar cell with p-i-n architecture with a possible g-FTO or  $\text{Cs:NiO}_x$  as electrode or hole transport layer. (F) Schematic of a 3-D view of a g-ITO/ $\text{NiO}_x$ /R-BPA SAM/perovskite/ $\text{PC}_{60}\text{BM}$ /Ag based solar cell with p-i-n architecture with a possible g-FTO or  $\text{Cs:NiO}_x$  as electrode or hole transport layer. The final area of each solar cell is  $0.09 \text{ cm}^2$ .

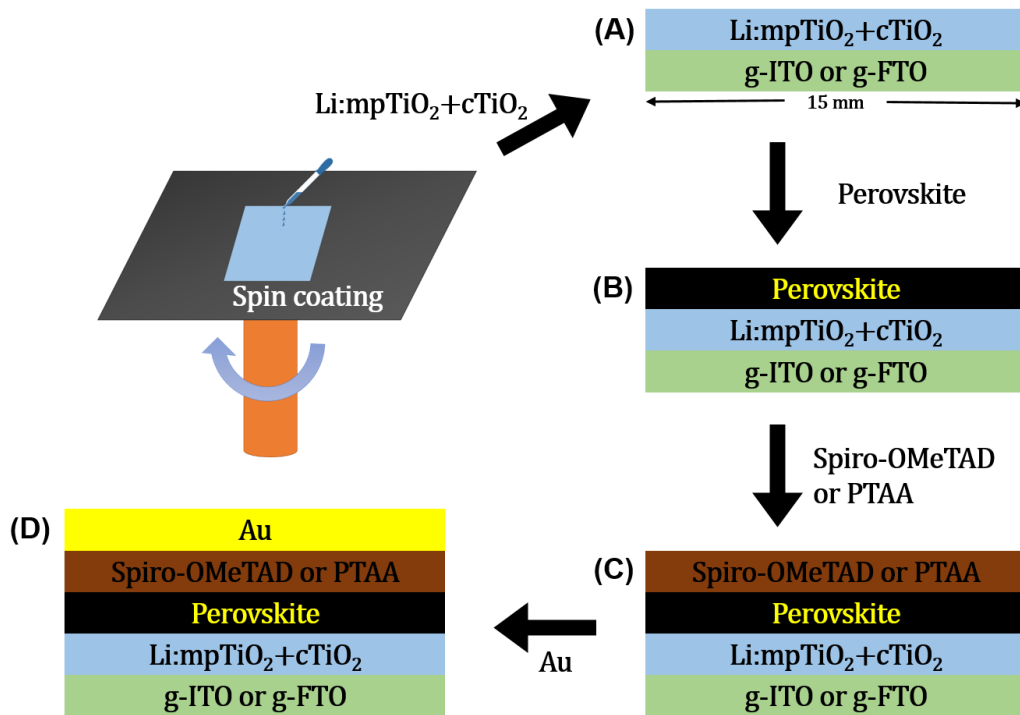


**Figure 50:** Schematic for the sequential spin coating of (A)  $\text{Li:mpTiO}_2 + \text{cTiO}_2$  layer (B) CsFAMA based triple cation lead halide perovskite (C) spiro-OMeTAD or PTAA, and thermal deposition of (D) Gold (Au) on  $\text{g-ITO}$  or  $\text{g-FTO}$  substrates.

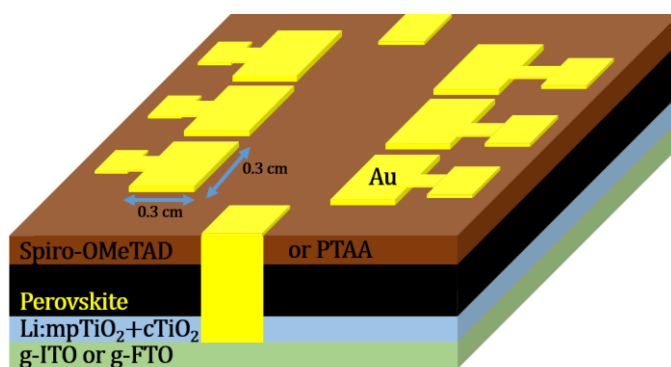


**Figure 51:** Schematic of a 3-dimensional view of g-ITO/Li:mpTiO<sub>2</sub>+cTiO<sub>2</sub>/perovskite/spiro-OMeTAD or PTAA/Au based solar cell with n-i-p architecture. The final area of each solar cell is 0.09 cm<sup>2</sup>.



---

## LIST OF FIGURES

---

**Figure 1:** (A) The  $ABX_3$  perovskite crystal structure with “A”-site monovalent cation, “B”-site divalent metal cation, and “X”-site monovalent halide anion. Reproduced with permission from Ref. [18]. Copyright © 2014. The Royal Society of Chemistry. (B) XRD reflexes for a triple cation and a double halide perovskite with lead as a metal centre having a  $Cs_{0.1}(FA_{0.83}MA_{0.17})_{0.9}Pb(I_{0.83}Br_{0.17})_3$  composition [22,38]..... 20

**Figure 2:** (A) mesoporous and (B) planar n-i-p architecture, and (C) mesoporous (mp) and (D) planar p-i-n architecture for perovskite solar cells. The metal (anode / cathode) is used as BE, spiro-OMeTAD or  $NiO_x$  is used as HTL,  $cTiO_2$  and  $mpTiO_2$ , and PCBM are used as ETL, and ITO patterned on glass (g-ITO) is used as TCO (cathode / anode). ..... 22

**Figure 3:** The HOMO and LUMO level alignments for different CTLs (HTLs and ETLs), perovskites, TCOs, and BEs [-]..... 23

**Figure 4:** Chemical structures of (A) spiro-OMeTAD, (B)  $PC_{60}BM$ , (C) PTAA, (D) P3HT (E) PEDOT:PSS, (F) LiTFSI, (G) TBP, and (H) FK209. .... 24

**Figure 5:** (A) Chemical structure of the new HTM, DM, used by Jeon et al. to achieve 23.2% efficient cells in a conventional architecture based solar cell [82]. (B) Crystal structure of  $Cu(thiourea)I$  used by Ye et al. to achieve 19.9% efficient cells in an inverted architecture based perovskite solar cell. The crystal structure of  $Cu(thiourea)I$  was Reprinted with permission from reference 87. Copyright © 2017. American Chemical Society. .... 26

**Figure 6:** (A) JV curves for champion devices and (C) cross sectional SEM image of the device published by Tavakoli et al., and (B) JV curves for large-area  $NiO_x$  and  $Cu:NiO_x$  based inverted devices and (D) cross sectional SEM image of the device published by Chen et al.. Reprinted with permission from reference 83 and 49 respectively. Copyright © 2018 WILEY-VCH Verlag GmbH & Co. KGaA, Weinheim. .... 27

**Figure 7:** Schematic of (A) few reasons among many that affect the hysteresis behaviour in the perovskite solar cell, and (B) different processes that may contribute to the hysteresis behaviour in the perovskite solar cell..... 29

**Figure 8:** Energy band diagram for an n-i-p architecture based solar cell illustrating the light absorption and excitation (red and blue), exciton (green) formation and consequent separation and collection of the charge particles (black arrows). The electron transport layer (ETL) is responsible to carry the electrons ( $e^-$ ) to the cathode (e.g. indium doped tin oxide (ITO)) and the hole transport layer (HTL) is responsible to carry the holes ( $h^+$ ) to the anode (e.g. gold (Au)). .... 31

**Figure 9:** (A) Schematic of a Current Density – Voltage (JV) curve for a solar cell with dark (red dot) and light (red solid) measurements. The figure shows the coordinates for different parameters such as  $V_{OC}$ ,  $J_{SC}$  in the graph. (B) Schematic of a Power – Voltage curve for solar cell depicting the  $J_{MPP}$ ,  $V_{MPP}$  and the power curve (green). (C) The spectral irradiance graph showing the sunlight spectra before entering the earth’s atmosphere (orange). The figure also shows the terrestrial global 37°C south facing tilt irradiance (black), direct normal and circumsolar irradiance (red), the ultraviolet, visible and infrared ranges, and the different absorption bands (blue) due to water ( $H_2O$ ), oxygen ( $O_2$ ), carbon dioxide ( $CO_2$ ) and the ozone ( $O_3$ ). (D) EQE curve (black) and integrated  $J_{SC}$  (blue) as a function of wavelength ( $\lambda$ ). In this figure the absorbance onset for the absorber material is depicted at

~770 nm (normal for lead halide perovskite based solar cell absorber material having bandgap of around 1.61 eV)..... 33

**Figure 10:** UV-Vis transmission spectra for  $c\text{TiO}_2$  and  $mp\text{TiO}_2$  on glass substrate with air as background. .... 53

**Figure 11:** XRD reflexes for CsFAMA perovskite (10% Cs) thin films prepared using DMF:DMSO perovskite solution in ratios of 4:1 and 1:4. .... 54

**Figure 12:** UV-Vis absorption spectra for CsFAMA perovskite (10% Cs) thin films prepared using DMF:DMSO solution in ratio of 4:1. .... 54

**Figure 13:** JV curves for solar cells with  $\text{Cs}_x(\text{FA}_{0.83}\text{MA}_{0.17})_{1-x}\text{Pb}(\text{I}_{0.83}\text{Br}_{0.17})_3$  with  $x =$  (A) 0 (0%), (B) 0.05 (5%), (C) 0.1 (10%), and (D) 0.15 (15%) Cs content in forward (F) and backward (B) sweep directions under illumination (Light, L). Cells were fabricated on ITO. .... 56

**Figure 14:** JV curves for solar cells with  $\text{Cs}_x(\text{FA}_{0.83}\text{MA}_{0.17})_{1-x}\text{Pb}(\text{I}_{0.83}\text{Br}_{0.17})_3$  with  $x =$  (A) 0 (0%), (B) 0.05 (5%), (C) 0.1 (10%), and (D) 0.15 (15%) Cs content in forward (F) and backward (B) sweep directions under illumination (Light, L). Cells were fabricated on FTO. .... 58

**Figure 15:** JV curves for (A) ITO and (B) FTO as TCO and perovskite (PS) spun at 4000 rpm and 6000 rpm. JV curves for FTO and ITO as TCO and PS spun at (C) 6000 rpm and (D) 4000 rpm. The graphs represent light and dark curves in forward sweep and backward sweep directions. (E and F) Zoomed in JV curves for dark conditions for ITO and FTO as TCO with PS spun at 6000 rpm and 4000 rpm. .... 60

**Figure 16:** JV curves for (A) spiro-OMeTAD and (B) PTAA as HTL for perovskite absorber layer deposited using DMF:DMSO solution in ratios of 4:1 and 1:4. (C) Normalized (100%) EQE for comparing spiro-OMeTAD and PTAA based solar cells with 4:1 perovskite solvent ratio. (D) spiro-OMeTAD as HTL with different doping profiles using LiTFSI, FK209 and TBP as dopants with 4:1 perovskite solvent ratio. .... 63

**Figure 17:** (A) perovskite ( $\text{Cs}_{0.1}$ ) on ITO/ $c\text{TiO}_2+mp\text{TiO}_2$  substrates after annealing at  $100^\circ\text{C}$  for 1 h. Solar cells with (B) PTAA and (C) spiro-OMeTAD as HTL. (D) Annealing perovskite layers on hot plate at  $100^\circ\text{C}$ . (E) Greyish and (F) black perovskite layer during annealing. .... 67

**Figure 18:** JV curves for (A) champion solar cell under light (L) and dark (D) conditions, and (B) backward sweep curves for comparing day 1, day 2 results with light soaking for 15 min, 30 min, 45 min, 60 min, 75 min, and 90 min, respectively. (C-F)  $V_{oc}$ ,  $J_{sc}$ , FF, and PCE trend after light soaking on day 2. .... 69

**Figure 19:** (A) Schematic illustration of the modification of the  $\text{NiO}_x$ -layer with 4-bromobenzylphosphonic acid and the device architectures of the investigated solar cells (glass/ITO/ $\text{NiO}_x$ /perovskite/ $\text{PC}_{60}\text{BM}/\text{Ag}$ ) without and with Br-BPA modification, (B) schematic energy band diagram for the device configuration ITO/ $\text{NiO}_x$ /perovskite/ $\text{PC}_{60}\text{BM}/\text{Ag}$ ; the scheme is not drawn to scale and the Fermi level is taken as the reference energy level. .... 83

**Figure 20:** Images showing the typical drop shapes of (A) water on a NiO<sub>x</sub> film, (B) water on NiO<sub>x</sub>/ Br-BPA film, (C) ethylene glycol on a NiO<sub>x</sub> film and (D) ethylene glycol on NiO<sub>x</sub>/ Br-BPA film. .... 84

**Figure 21:** XPS survey spectra of a non-modified (A) and modified NiO<sub>x</sub> film (B); details of the region of the relevant P- and Br-peaks (C) confirming the presence of phosphor and bromine at the surface of the modified NiO<sub>x</sub> film; high resolution XPS spectra and peak deconvolution of the P 2p (D) and the Br 3p peak with additional signal of P 2s (E) in the modified sample..... 85

**Figure 22:** (A) XRD patterns and (B) UV-Vis absorption spectra of perovskite thin films prepared on glass/ITO/NiO<sub>x</sub> substrates without and with Br-BPA modification..... 87

**Figure 23:** Top view SEM images of perovskite thin films prepared on a non- modified (A) and modified (B) NiO<sub>x</sub> layer..... 88

**Figure 24:** (A) JV curves (dark and illuminated) measured in forward and backward direction, (B) maximum power point tracking measurements and (C) EQE spectra of typical perovskite solar cells prepared with non-modified and modified NiO<sub>x</sub> hole transport layers. .... 89

**Figure 25:** Box plots showing statistics of the characteristic parameters (A) V<sub>OC</sub>, (B) J<sub>SC</sub>, (C) FF and (D) PCE of the best 20 devices prepared each with non-modified and modified NiO<sub>x</sub> hole transport layers..... 91

**Figure 26:** JV curves (A) and EQE spectrum (B) of one of the devices with Br-BPA modification showing the highest V<sub>oc</sub> prepared within this study. .... 92

**Figure 27:** Schematic representation of (A) Br- and NH<sub>2</sub>-functionalized BPA based SAMs on NiO<sub>x</sub> surface. The red arrows indicate the directed dipole of the molecule towards or away from the NiO<sub>x</sub>. (B) Band bending diagram of the band edges of NiO<sub>x</sub> and perovskite and the effect of dipole moments on energy gap between the band edges of NiO<sub>x</sub> and perovskite. Here 'δ+x' indicates the increase in the gap when dipole is directed away from NiO<sub>x</sub>, and 'δ-y' indicates decrease when dipole is directed towards the NiO<sub>x</sub> with respect to the non-modified NiO<sub>x</sub> having a constant gap of 'δ'. The value of 'x' and 'y' depend upon the nature of dipole and its impact on the energy gap. .... 101

**Figure 28:** (A) XRD reflexes for NiO<sub>x</sub> nanoparticles based thin films and (B) UV-Vis transmission curves for glass and nanoparticles and sol-gel based NiO<sub>x</sub> thin films. The inset contains pictures of the solutions for NiO<sub>x</sub> nanoparticles in deionized water and NiO<sub>x</sub> sol-gel solution before thin film deposition. .... 106

**Figure 29:** Images of water drops on NiO<sub>x</sub> nanoparticles based thin films modified by dip coated R-BPA molecules. .... 106

**Figure 30:** XRD reflexes for CsFAMA perovskites deposited on NiO<sub>x</sub> nanoparticles based thin films dip coated in R-BPA solution. .... 108

**Figure 31:** UV-Vis absorption spectra for CsFAMA perovskites deposited on NiO<sub>x</sub> nanoparticles based thin films dip coated in R-BPA solution. .... 109



|  |     |
|--|-----|
| <b>Figure 32:</b> Top view SEM images for CsFAMA perovskites on NiO <sub>x</sub> nanoparticles based thin films modified by dip coated R-BPA molecules.....  | 110 |
| <b>Figure 33:</b> JV curves for light (indicated as L in the legends) measurements for forward (F) and backward (B) sweeps for CsFAMA, Br-BPA SAM/CsFAMA and F-BPA SAM/CsFAMA based solar cells. ....  | 111 |
| <b>Figure 34:</b> JV curves for (A, B, and C) dip coated R-BPA SAM modified NiO <sub>x</sub> thin films in light and dark conditions for forward and backward sweep directions and (D) comparison of the JV curves in light conditions for forward sweep direction.....  | 113 |
| <b>Figure 35:</b> JV curves for 15 min and 1 h annealing time for CsFAMA based solar cells in light conditions for forward and backward sweep directions. ....   | 115 |
| <b>Figure 36:</b> XRD reflexes for CsFAMA films annealed at 15 min and 1 h. The inset focuses on the presence of $\delta$ -FAPbI <sub>3</sub> for 15 min annealed films and cubic PbI <sub>2</sub> for both the samples. ....  | 116 |
| <b>Figure 37:</b> Top view SEM images for NiO <sub>x</sub> nanoparticles based thin films on ITO with concentrations (A-C) 20 mg/mL, (D) 20 mg / 2 mL, and (E) 40 mg/mL.....   | 117 |
| <b>Figure 38:</b> (A) JV curves for Cs:NiO <sub>x</sub> /CsFAMA based solar cells without and with mask (without 0.09 cm <sup>2</sup> and with 0.0702 cm <sup>2</sup> ), (B) EQE and integrated J <sub>SC</sub> , (C-D) maximum power point tracking of J <sub>MPP</sub> and PCE.....  | 118 |
| <b>Figure 39:</b> JV curve for (A) Cs:NiO <sub>x</sub> /CsFAMA perovskite solar cells and (B-D) solar cells with R-BPA molecules deposited on Cs:NiO <sub>x</sub> thin films. ....   | 119 |
| <b>Figure 40:</b> Images of water drops on NiO <sub>x</sub> nanoparticles based thin films modified by spin coated R-BPA molecules. ....   | 121 |
| <b>Figure 41:</b> XRD reflexes for CsFAMA perovskites deposited on NiO <sub>x</sub> nanoparticles based thin films modified by spin coating R-BPA solution.....  | 123 |
| <b>Figure 42:</b> UV-Vis absorption spectra for CsFAMA perovskites deposited on NiO <sub>x</sub> nanoparticles based thin films modified by spin coating R-BPA solution. ....  | 124 |
| <b>Figure 43:</b> Top view SEM images for CsFAMA perovskite on non-modified and Br-BPA, NH <sub>2</sub> -BPA and BPA molecules modified NiO <sub>x</sub> thin films. The modification was done using spin coating. ....  | 125 |
| <b>Figure 44:</b> Cross sectional SEM images for ITO/NiO <sub>x</sub> / without and with R-BPA/CsFAMA/PC <sub>60</sub> ABM substrates for spin coated R-BPA molecules on NiO <sub>x</sub> thin films. ....   | 125 |
| <b>Figure 45:</b> JV curves for spin coated R-BPA molecules on NiO <sub>x</sub> nanoparticles based thin films and 1 h annealed CsFAMA perovskite. (A) Comparison of non-modified and Br-BPA molecules based cells and (B) backward curves for non-modified, Br-BPA, NH <sub>2</sub> -BPA and BPA modified solar cells. .... | 126 |
| <b>Figure 46:</b> (A) MPPT of PCE and (B) EQE and integrated J <sub>SC</sub> for spin coated R-BPA molecules on NiO <sub>x</sub> nanoparticles based thin films and 1 h annealed CsFAMA. ....  | 127 |

**Figure 47:** (A) Br-BPA molecule and corresponding schematic diagram where the red star indicated the Br group (red in the molecule structure), blue star indicates the phosphonic acid ( $H_2PO_3^-$ ) anchor group. (B) 2-D schematic for pre- and post- deposition of the benzylphosphonic acid molecule on g-ITO/ $NiO_x$  surface. (C) Schematic for dip coating of phosphonic acid molecules on g-ITO/ $NiO_x$  substrate in a three step process. .... 144

**Figure 48:** spin coating steps for (A) g-ITO/ $NiO_x$  film with (B) R-BPA molecule (1) and rinsing with fresh acetonitrile (2), and (C) R-BPA SAM molecules adsorbed on g-ITO/ $NiO_x$  substrates forming g-ITO/ $NiO_x$ /R-BPA SAM..... 145

**Figure 49:** Schematic for the sequential spin coating of (A)  $NiO_x$  or Cs: $NiO_x$  layer (B) CsFAMA based triple cation lead halide perovskite (C)  $PC_{60}BM$  layer, and thermal deposition of (D) Silver (Ag) on g-ITO substrate. (E) Schematic of a 3-D view of a g-ITO/ $NiO_x$ /perovskite/ $PC_{60}BM$ /Ag based solar cell with p-i-n architecture with a possible g-FTO or Cs: $NiO_x$  as electrode or hole transport layer. (F) Schematic of a 3-D view of a g-ITO/ $NiO_x$ /R-BPA SAM/perovskite/ $PC_{60}BM$ /Ag based solar cell with p-i-n architecture with a possible g-FTO or Cs: $NiO_x$  as electrode or hole transport layer. The final area of each solar cell is  $0.09\text{ cm}^2$ . .... 146

**Figure 50:** Schematic for the sequential spin coating of (A) Li:mpTiO<sub>2</sub>+cTiO<sub>2</sub> layer (B) CsFAMA based triple cation lead halide perovskite (C) spiro-OMeTAD or PTAA, and thermal deposition of (D) Gold (Au) on g-ITO or g-FTO substrates..... 147

**Figure 51:** Schematic of a 3-dimensional view of g-ITO/Li:mpTiO<sub>2</sub>+cTiO<sub>2</sub>/perovskite/spiro-OMeTAD or PTAA/Au based solar cell with n-i-p architecture. The final area of each solar cell is  $0.09\text{ cm}^2$ ..... 148

---

## LIST OF TABLES

---

|  |     |
|--|-----|
| <b>Table 1:</b> <i>V<sub>OC</sub>, absolute J<sub>SC</sub>, FF, and PCE values for light measurements for the graphs shown in Figure 13. The values are listed in forward (backward) sweep directions. ....</i>  | 56  |
| <b>Table 2:</b> <i>V<sub>OC</sub>, absolute J<sub>SC</sub>, FF, and PCE values for light measurements for the graphs shown in Figure 14. The values are listed in forward (backward) sweep directions. ....</i>  | 58  |
| <b>Table 3:</b> <i>V<sub>OC</sub>, absolute J<sub>SC</sub>, FF, and PCE values for light measurements for the graphs shown in Figure 15. The values are listed in forward (backward) sweep directions. ....</i>  | 61  |
| <b>Table 4:</b> <i>V<sub>OC</sub>, absolute J<sub>SC</sub>, FF, and PCE values for light measurements for the graphs shown in Figure 16A-B. The values are listed in forward (backward) sweep directions. ....</i>   | 64  |
| <b>Table 5:</b> <i>V<sub>OC</sub>, absolute J<sub>SC</sub>, FF, and PCE values for light measurements for the graphs shown in Figure 16C. The values are listed in forward (backward) sweep directions. ....</i>   | 65  |
| <b>Table 6:</b> <i>V<sub>OC</sub>, absolute J<sub>SC</sub>, FF, and PCE values for light measurements for the graphs shown in Figure 18A. The values are listed in forward (backward) sweep directions. ....</i>   | 70  |
| <b>Table 7:</b> <i>Results of the contact angle measurements of the non-modified and modified NiO<sub>x</sub> layers. ....</i>   | 84  |
| <b>Table 8:</b> <i>Characteristic parameters of typical perovskite solar cells prepared with non-modified and modified NiO<sub>x</sub> hole transport layers. ....</i>   | 90  |
| <b>Table 9:</b> <i>Contact angles (CAs) of water measured on NiO<sub>x</sub> nanoparticles based thin films modified by dip coated R-BPA molecules. ....</i>   | 107 |
| <b>Table 10:</b> <i>XRD reflexes for (110) and (220) lattice planes in CsFAMA perovskites on NiO<sub>x</sub> nanoparticles based thin films which were modified by dip coated R-BPA molecules. ....</i>  | 108 |
| <b>Table 11:</b> <i>V<sub>OC</sub>, absolute J<sub>SC</sub>, FF, and PCE values for light measurements of CsFAMA, Br-BPA SAM/CsFAMA and F-BPA SAM/CsFAMA based solar cells along with the mean values for best 5 cells. The values are listed in forward (backward) sweep directions. ....</i>   | 112 |
| <b>Table 12:</b> <i>V<sub>OC</sub>, absolute J<sub>SC</sub>, FF, and PCE values for light measurements of NiO<sub>x</sub>/CsFAMA, NiO<sub>x</sub>/Br-BPA SAM/CsFAMA, NiO<sub>x</sub>/F-BPA SAM/CsFAMA, NiO<sub>x</sub>/NH<sub>2</sub>-BPA SAM/CsFAMA, NiO<sub>x</sub>/NO<sub>2</sub>-BPA SAM/CsFAMA, NiO<sub>x</sub>/OCH<sub>3</sub>-BPA SAM/CsFAMA, and NiO<sub>x</sub>/BPA SAM/CsFAMA based solar cells in forward (backward) directions. The measurement values are for NiO<sub>x</sub> nanoparticles and dip coated R-BPA SAM based HTL modified solar cells. ....</i> | 114 |
| <b>Table 13:</b> <i>V<sub>OC</sub>, absolute J<sub>SC</sub>, FF, and PCE values for light measurements of NiO<sub>x</sub>/CsFAMA based solar cells for 1 h and 15 min CsFAMA perovskite annealing time at 100°C. ....</i>  | 115 |
| <b>Table 14:</b> <i>V<sub>OC</sub>, absolute J<sub>SC</sub>, FF, and PCE values of Cs:NiO<sub>x</sub> and CsFAMA based solar cells. The values are listed in forward (backward) sweep directions. ....</i>   | 119 |
| <b>Table 15:</b> <i>V<sub>OC</sub>, absolute J<sub>SC</sub>, FF, and PCE values for light measurements of Cs:NiO<sub>x</sub> based solar cells with R-BPA SAM functionalization by dip coating. The values are listed in forward (backward) sweep directions. ....</i>   | 120 |

**Table 16:** Contact angles (CAs) of water measured on NiO<sub>x</sub> nanoparticles based thin films modified by spin coated R-BPA molecules. .... 122

**Table 17:** XRD reflexes for (110) and (220) lattice planes in CsFAMA perovskites on NiO<sub>x</sub> nanoparticles based thin films which were modified by spin coating R-BPA molecules. . 123

**Table 18:** V<sub>OC</sub>, absolute J<sub>SC</sub>, FF, and PCE values for light measurements of the NiO<sub>x</sub> nanoparticles based solar cells with BPA SAM, Br-BPA SAM, and NH<sub>2</sub>-BPA SAM. The SAMs were deposited using dynamic spin coating and the CsFAMA perovskites were annealed for 1 h at 100°C. The values are listed in forward (backward) sweep directions. .... 127



---

## CURRICULUM VITAE

---

**Jimmy Mangalam**

### **Bachelor's and Master's in Nanotechnology**

Email (office): [mangalam@tugraz.at](mailto:mangalam@tugraz.at)

Phone (Office): +4331687332317

ORCID: 0000-0002-1809-5242

Email: [jimmymangalam@gmail.com](mailto:jimmymangalam@gmail.com)

Mobile (Austrian): +436608381535

Mobile (Indian): +919971911883

### **Publications:**

- **J. Mangalam**, T. Rath, S. Weber, Birgit Kunert, T. Dimopoulos, A. Fian, G. Trimmel, "Modification of NiO<sub>x</sub> hole transport layers with 4-bromobenzylphosphonic acid and its influence on the performance of lead halide perovskite solar cells". *Journal of Materials Science: Materials in Electronics*, In Press (2019). DOI: 10.1007/s10854-019-01294-0.
- **J. Mangalam**, M. Kumar, M. Sharma, M. Joshi, "High adsorptivity and visible light assisted photocatalytic activity of silver/reduced graphene oxide (Ag/rGO) nanocomposite for wastewater treatment", *Nano-Structure & Nano-Objects* 17 (2019), 58-66. DOI: 10.1016/j.nanoso.2018.11.003.
- S. Weber, T. Rath, **J. Mangalam**, B. Kunert, A. M. Coclite, M. Bauch, T. Dimopoulos, G. Trimmel, "Investigation of NiO<sub>x</sub>-hole transport layers in triple cation perovskite solar cells", *J. Mater. Sci: Mater Electron* 29 (2018), 1847-1855. DOI: 10.1007/s10854-017-8094-9.
- **J. Mangalam**, S. Agarwal, A. N. Resmi, M. Sundararajan, K. B. Jinesh, "Resistive Switching in Polymethyl methacrylate thin films", *Organic Electronics* 29 (2016), 33-38. DOI: 10.1016/j.orgel.2015.11.017.

### **Conference Proceeding:**

- 17<sup>th</sup> International Workshop on Physics of Semiconductor and Devices – 2013, Amity University Uttar Pradesh, Sector 125, Noida 201301, Uttar Pradesh, India. "Grafting of Ag Nanoparticles on GO nano sheets for Water Purification Application", **J. Mangalam**, M. Joshi. *Environmental Engineering, Springer, ISSN: 1863-5520*, DOI: 10.1007/978-3-319-03002-9, Author: V. K. Jain and A. Verma.

### **Posters:**

- 2018 MRS Fall meetings and exhibits – November 2018, Boston MA, USA. "Investigating the effects of functionalized benzylphosphonic acid SAMs on triple cation perovskite based solar cells", **J. Mangalam**, T. Rath, S. Weber, B. Kunert, T. Dimopoulos, A. Fian, G. Trimmel.
- HOPV – May 2018, Benidorm, Spain. "R-functionalized benzylphosphonic acid SAMs for improved efficiency in inverted triple cation lead perovskite solar cells", **J. Mangalam**, T. Rath, S. Weber, B. Kunert, T. Dimopoulos, A. Fian, G. Trimmel.
- Photovoltaic days – November 2017, Vienna, Austria. "Effects of hole transport layers on triple cation perovskite based conventional and inverted solar cell geometry", **J. Mangalam**, T. Rath, S. Weber, B. Kunert, A. M. Coclite, M. Bauch, T. Dimopoulos, G. Trimmel.
- DocDays – April 2017, Doctoral School of Chemistry, Karl-Franzens University and Graz University of Technology, Graz A-8010, Austria. "Comparison of triple cation

*perovskite solar cells with two different hole transport layers*”, **J. Mangalam**, T. Rath, G. Trimmel.

- 17<sup>th</sup> International Workshop on Physics of Semiconductor and Devices – 2013, Amity University Uttar Pradesh, Sector 125, Noida 201301, Uttar Pradesh, India. “*Grafting of Ag Nanoparticles on GO nano sheets for Water Purification Application*”, **J. Mangalam**, M. Joshi.
- Nanotechnology in Conventional and Alternate Energy – August 2013, University of Petroleum and Energy Studies, Dehradun 248007, Uttarakhand, India. “*Synthesis and Characterization of Ag-GO nanocomposite for water purification application*”, **J. Mangalam**, Monika Joshi

#### **PhD candidate:**

- Under the guidance of **Assoc. Prof. Dipl.-Ing. Dr.techn. Gregor Trimmel**, at the Institute for Chemistry and Technology of Materials, Graz University of Technology, Stremayrgasse 9, Graz A-8010, Austria.
- **Topic: Investigation on hybrid perovskite solar cells**
- Duration: July 2016 – Present.

#### **Bachelor’s and Master’s in Nanotechnology:**

- Amity Institute of Nanotechnology, Amity University Uttar Pradesh, Sector 125, Noida 201301, Uttar Pradesh, India
- Grade Point Average: 7.35 / 10
- Duration: July 2011 – June 2016.

#### **Master Thesis:**

- Under the guidance of **Assoc. Prof. Dipl.-Ing. Dr. techn. Karin Zojer**, at the Institute of Solid State Physics, Graz University of Technology, Petersgasse 16, Graz A-8010, Austria.
- **Topic: Macroscopic transport simulations to understand the coupling between electric and heat current in organic light emitting diode.**
- Duration: January 2016 – June 2016.

#### **Bachelor Thesis:**

- Under the guidance of **Dr. K. B. Jinesh**, at the Department of Physics, Indian Institute of Space Science Technology, Thiruvananthapuram – 695547, Kerala, India.
- **Topic: Resistive switching in Polymethyl methacrylate.**
- Duration: February 2015 – June 2015.

#### **Reference:**

- Dr. Gregor Trimmel [gregor.trimmel@tugraz.at](mailto:gregor.trimmel@tugraz.at)
- Dr. Thomas Rath [thomas.rath@tugraz.at](mailto:thomas.rath@tugraz.at)
- Dr. Karin Zojer [karin.zojer@tugraz.at](mailto:karin.zojer@tugraz.at)
- Dr. K. B. Jinesh [kbjinesh@iist.ac.in](mailto:kbjinesh@iist.ac.in)
- Dr. Monika Joshi [mjoshi@amity.edu](mailto:mjoshi@amity.edu)

*Here my hike ends and the view from the top is humbling...*

*- Yours truly...*